# Investigation of a Remote Sensing Technique for Droplet Effective Radius

by
Melanie A. Wetzel

Department of Atmospheric Science
Colorado State University
Fort Collins, Colorado

ONR N00014-86-C-0459

Colorado State University

Department of Atmospheric Science

Paper No. 469

# INVESTIGATION OF A REMOTE SENSING TECHNIQUE FOR DROPLET EFFECTIVE RADIUS

by

Melanie A. Wetzel

Department of Atmospheric Science
Colorado State University
Fort Collins, Colorado 80523

Spring, 1990

Atmospheric Science Paper No. 469

Research Supported by
ONR Contract No. N00014-86-C-0459
Principal Investigator: Thomas H. Vonder Haar

This paper was also submitted in partial fulfillment of the requirements for the Degree of Doctor of Philosophy.

## ABSTRACT

Theoretical and observational studies are carried out to evaluate the use of cloud near-infrared spectral reflectance to determine cloud droplet size. A multiple scattering radiative transfer model for plane-parallel clouds is developed in order to determine monochromatic cloud reflectance in the 0.85 and 1.6 micrometer atmospheric windows. The results are applied to an objective retrieval technique for droplet effective radius. It is shown that the retrieval technique provides accurate droplet size estimates from known values of bispectral reflectance. Potential uncertainties due to measurement or viewing geometry errors are identified. The influence of cloud structure variability on the retrieval accuracy is determined through numerical simulations representing vertical inhomogeneity of cloud microphysical characteristics, limited horizontal extent of cloud, and the presence of aerosol vertically adjacent to and within cloud. The results of the simulations indicate little sensitivity of the retrieved droplet size due to typical cloud inhomogeneity, except in the case of shallow cloud atop a hazy marine boundary layer. The ability to correctly identify droplet effective radius variations is shown to require cloud of sufficient optical depth. Analysis of field measurement data demonstrate a retrieval accuracy within an uncertainty of 3 micrometers for cloud areas of sufficient optical depth, and a bias toward larger retrieved sizes for optically thin cloud. The results suggest the utility and some possible limitations of satellite remote sensing of cloud droplet size.

# ACKNOWLEDGEMENTS

Heartfelt appreciation is extended to the several colleagues who have offered technical assistance and scientific interaction during this research project. The contribution of time and expertise by Dr. Douglas Jensen of the Naval Ocean Systems Center (NOSC) was essential to the successful utilization of the data collection systems of the research aircraft. Dr. Hung-Chi Kuo (Naval Environmental Prediction and Research Facility) and Chi-Fan Shih (CSU) also provided valuable scientific support during the field program. Dr. Philip Durkee (Naval Postgraduate School) assisted in the acquisition of a set of the satellite data used for analysis. Chris Johnson-Pasqua (CSU) kindly provided help in the areas of radiometric instrument design and implementation. The calibration of the Spectral Radiometer was made possible by Daryl Myers and the facilities of the Solar Energy Research Institute (SERI). Financial funding for the field measurement program and computer-based data analysis and numerical modeling was provided primarily through the Office of Naval Research (ONR) under Contract No. N00014-86-C-0459, NOSC, and CIRA. Additional support was provided by CSU, the National Park Service group at CIRA, and the CSU Supercomputing Project.

I thank my graduate advisor, Dr. Thomas Vonder Haar, for his support and guidance during the successive phases of my Ph.D. studies. Each of the other members of my graduate committee at CSU have given valuable suggestions during this work. These professors are Dr. William Cotton, Dr. Stephen Cox, Dr. Siu-Au Lee, and Dr. Graeme Stephens. I also would like to thank my family and friends, particularly Randolph Borys, for the encouragement which played an important part in the attainment of this goal.

TABLE OF CONTENTS

LIST OF FIGURES

LIST OF TABLES

# Chapter 1

# INTRODUCTION

## 1.1 Motivation for research on the remote sensing of droplet size

Clouds play a critical role in modulating the exchange of solar and infrared radiation in the atmosphere. Scattering and absorption by clouds leads to the spatial redistribution and transformation of radiative energy, which subsequently drives atmospheric motions. Extensive marine stratus and stratocumulus clouds form over the subtropical oceans, where the descending branch of the Hadley Cell circulation creates a strong thermal inversion due to compressional warming (Schubert *et al.*, 1979) . These cloud decks are thought to be a source of significant radiational cooling for the atmosphere within the region. The relationship of marine stratiform cloudiness to the atmospheric general circulation, the control it exerts on coastal weather and ocean surface warming, and the little known nature of cloud layer formation and breakup, combine to make this cloud type of particular value for remote sensing applications, particularly because the ocean areas are sparsely observed except by satellites.

Remote sensing offers the opportunity to routinely observe cloud distribution and cloud physical characteristics over large regions, and improvement in remote sensing techniques is continually sought. Satellite remote sensing methods for cloud observations have, up to the present, primarily relied on passive radiance measurement in the relatively broad wavelength bands which correspond to the visible (0.38 to 0.76 micrometers), and in what is termed the "atmospheric infrared window" (10 to 12 micrometers). The information derived from broadband observations is limited by our inability to seperate processes of extinction by the cloud particles, aerosol, and atmospheric gases. For example, problems have arisen from attempting to match cloud shortwave reflectance or

albedo measurements against model calculations. The disagreement of observations and numerical estimates (Reynolds *et al.* (1975), Stephens *et al.* (1978c), Twomey and Cocks (1982) and others) has become known as the "cloud absorption paradox". Discrepancies may be due, in some of the comparisons, to inadequate representation or measurement of absorbing constituents such as water vapor. By measuring cloud reflectance in wavelength regions where gaseous absorption is minimized, we can observe extinction processes due to the particles and simultaneously investigate the contribution of these particles to cloud absorption.

This chapter will introduce the rationale and theoretical background for the study of stratus cloud spectral reflectance, and outline the stategy for the investigation of a proposed method of estimating cloud droplet size from spectral reflectance measurements. The meteorological significance of estimating droplet size by remote sensing is discussed in Section 1.2. Section 1.3 presents the requirements for an operational procedure of cloud droplet size estimation. Section 1.4 identifies the narrow wavelength intervals which are used as "spectral windows". These are centered at wavelengths where the absorption and reflection of solar radiation by clouds primarily depends on the cloud particle sizes, composition, and cloud structure, as outlined in Section 1.5. Specific goals of the present research are to develop an objective method of retrieving droplet size and to evaluate that method, as stated in Section 1.6. We utilize multiple scattering calculations for cloud layers composed of analytical droplet size distributions to develop the estimation method, and we test the derived relationships between cloud reflectance and droplet size using field measurements. The research strategy is outlined in Section 1.7.

## 1.2 Meteorological significance of droplet size estimates

The estimation of effective radius ($r_e$) of a droplet size distribution has synoptic, thermodynamic and radiative applications. Objective remote determination of a cloud type based on droplet size could contribute information to nephanalysis, flight planning, initialization of atmospheric circulation models, and statistical analysis of cloud cover and

radiation budget parameters. Determination of the droplet size itself can be used in parameterizations such the energy transfer in cloud models and defense-related electromagnetic propagation.

Several theories exist on the role of microphysical structure in cloud dynamic processes, which could benefit from estimates of droplet size over large regions of cloud. The work of Wiscombe *et al.* (1984) demonstrates that variation of droplet size characteristics influences the scattering and absorption by clouds. Droplet size distributions which include very large droplets lead to model calculations of substantially increased shortwave absorptivity and decreased spectral albedo. Cloud top infrared cooling is also directly related to liquid water content and the predominance of larger droplets (Barkstrom, 1978). An estimate of droplet effective radius, in conjunction with an estimate of liquid water content, may help in diagnosing entrainment and the resulting cloud cover evolution.

Rogers and Telford (1986) argue that a criterion for the onset of dynamic instability and entrainment leading to cloud layer break-up must depend on thermodynamic factors (such as the stability of the inversion and size of the turbulent eddies produced) and microphysical factors (such as the sizes and total mass concentration of cloud droplets participating in significant radiation exchange). They suggest that the presence of larger droplets can lead to the establishment of instability when convective turbulence mixes them into the overlying dry air faster than they settle below the cloud-top turbulence layer. The remote sensing of $r_e$ would help in testing this idea. In another application, large values of $r_e$ could indicate colloidal instability, a tendency toward precipitation formation due to a predominance of larger droplets with their higher coalescence efficiencies. Like mean radius, of course, a given value of effective radius can be produced by different droplet size spectra. A size distribution with two or three significant concentration modes will produce a cloud reflectance signature for the entire population, with the largest droplet mode contributing most to the effective radius. The particular reflectance characteristics will be determined by the numbers and liquid water contents of the individual modes. Thus, microphysical applications of a reflectance-based estimate of effective radius are limited by their sensitivity to multimodal populations.

If the shape of the size distribution can be represented by an monomodal analytic function, $r_e$ can be directly related to other parameters such as mean radius $r_m$ or the radius of the 95-percent volume liquid water content ($r_{95}$). As discussed by Curry (1986) , correlations between size distribution parameters are an indication of the type of parcel mixing mechanism which predominates at cloud top. The mixing mechanism determines the relationship of variations in droplet sizes, number concentrations, and liquid water content as entrainment proceeds, which will influence subsequent thermodynamic processes. In entity-type mixing (Telford and Wagner, 1981) , entrainment leads to the selective evaporation of the smallest droplets. There is a consequent reduction in $r_{95}$ and droplet concentration ($N$), while liquid water content ($W$) is changed little. We can expect that $r_e$ will be altered similarly to $r_{95}$, due to the sharp decreasing trend in $r_e$ as the population of droplets in the largest sizes lose mass. More information is needed on how cloud scale dynamics are related to variations in these microphysical parameters, so that the value of remote sensing of droplet size can be assessed.

The effective radius can also be applied in deducing other physical parameters of a cloud layer. Paltridge and Platt (1976, p. 80) show that we can estimate the shortwave volume extinction coefficient ($\beta$) from

$$\beta \approx \frac{3W}{2r_e}. \tag{1.1}$$

The physical units for this expression are prescribed by $\beta$ ($\mathrm{m}^{-1}$), $W$ ($\mathrm{g\,m}^{-3}$), and $r_e$ ($\mu$m). Slingo and Schrecker (1982) have developed model parameterizations of cloud scattering which require as input only the effective radius and liquid water content. They produce estimates of the extinction coefficient, single scattering albedo and asymmetry parameter for use in a broadband shortwave radiation model. The results of these parameterizations can then provide rapid input to net radiation budgets over large cloud regions. Similarly, Stephens (1978b) and Wiscombe *et al.* (1984) indicate that the optical depth of clouds depends on two moments of the droplet size distribution, for example, $r_e$ and liquid water path ($LWP$). The $LWP$ is the vertically integrated in-cloud water content for the sampled droplet size distribution. Also, Ackerman and Stephens (1987) demonstrate that cloud

reflectance relationships to droplet size vary according to the magnitude of the liquid water path. The remote sensing retrieval method described herein is designed to utilize optical depth estimates rather than requiring information on cloud liquid water path. It is shown that the optical depth must be within a specific range in order to successfully apply the retrieval method.

Cloud particle size spectra evolve by dynamic mixing processes and energy transfer in cloud, and in turn they control the extent and time scale for condensation, entrainment and sensible heating. For example, on five of six research flights in marine stratiform cloud layers, Nicholls and Leighton (1986) found that turbulent mixing in the cloud layer was primarily maintained by cloud top radiative cooling. They suggest that a broad droplet spectrum is indicative of shallow convection, with a cloud layer uncoupled to the full depth of the marine boundary layer because droplets are not involved in frequent cycling out into the non-cloudy air. The enhanced lifetimes of these droplets allows broadening of the distribution. Distribution broadening can be related to an increased effective radius or variance of the droplet population. We will see in Chapter 2 how expected variability in droplet effective radius and the variance of the size spectrum impact cloud reflectance.

Variations in the microphysical parameters must occur on a large enough spatial scale if they are to provide reflectance measurements which are representative of that microphysical structure. Mixtures of droplet populations within the viewed cloud top area can produce an estimate of droplet effective radius which does not equal that of any of the individual size spectra present. In this case, the remote sensing has limited usefulness in providing microphysical data. In the case of mixing of different size spectra, a value of effective radius estimated from cloud reflectance is only an indicator of the relative contributions by the different spectra. However, the data can still provide an effective radius value which accurately represents the reflectance properties of the observed cloud. As described above, the effective radius has been used to parameterize cloud radiative parameters. For this purpose, we require a value of effective radius characteristic of a relatively large cloud region. The parameterizations also require a value of cloud liquid water content, such that this must be estimated by some means on the same spatial scale as the effective radius.

In summary, the potential applications of remote sensing techniques for cloud optical and physical parameters are numerous. The profusion of ideas concerning microphysical-radiative interaction attests to its importance in boundary layer cloud systems. Monitoring of cloud parameters is essential to the study of these interactions, because more information is needed on the role of droplet populations in controlling cloud radiation budgets. Large scale climatic conditions are modulated by the physical and temporal characteristics of cloudiness. As noted long ago by Lilly (1968), " ...it would appear impossible...to maintain a 15–20 degree inversion at a height of 500–1000 meters without a radiatively effective cloud cover." If the system is in a radiative balance dependent on cloud microphysical conditions, we must anticipate the factors which allow transitions. The ability to estimate cloud droplet sizes from satellite observations would improve regional and global scale climatologies of cloud parameters for monitoring of global change, where that change may be due to increased cloud condensation nuclei production, greenhouse warming, deforestation, other direct influences by man, or transitions due to extraterrestrial solar flux variations.

Some of the possible applications of droplet size estimates to diagnosis of cloud dynamic processes require more study of the observed relationships between microphysical and dynamic characteristics, to determine whether the significant microphysical structure can be unambiguously determined from satellite. However, a value of effective radius directly estimated from cloud reflectance should be immediately useful in the parameterization of broadband shortwave radiation budget calculations. Requirements of a remote sensing technique for estimation of effective radius is discussed in Section 1.3. The ability of remote sensing to provide these data is then explored in the later Chapters.

## 1.3 Requirements for a remote sensing technique

Remote sensing applications require the identification of the acceptable uncertainty due to measurement limitations and acceptable error in the resultant parameters. We can then determine whether the sensitivity of the instrument system is sufficient to identify cloud radiance variations to meet the desired accuracy of the retrieval procedure.

An error of 3 $\mu$m for the effective radius estimate was judged acceptable in this study, based on the potential applications discussed in the preceeding section. The typical range of values for effective radius in marine stratus is 3–15 $\mu$m, including fog-like layers with values in the smaller size ranges and convective layers with effective radius values in the larger size ranges (Slingo *et al.*, 1982 ; Bonnel *et al.*, 1983 ). Stratus could therefore be objectively sub-classified according to size estimates. The parameterization between cloud optical depth, liquid water content, and effective radius discussed by Stephens (1978b) can be used to test the sensitivity of $r_e$ estimates in climate-related models. According to Charlock's (1982) study of surface warming under the influence of an increased solar constant, a change in a marine stratus cloud $r_e$ by 3 $\mu$m is sufficient to alter the magnitude of surface warming by 1K. Slingo and Schrecker's (1982) parameterization of cloud scattering using effective radius and liquid water content shows that a 3 $\mu$m variation in effective radius of a mid-latitude stratus layer leads to a 7% variation in system albedo. Size-dependent droplet growth rates due to longwave cooling has been investigated by Barkstrom (1978). For low, thin cloud, a droplet of 9.5 $\mu$m radius can grow by 1 $\mu$m radius in 2.5 minutes, but a droplet of 4.5 $\mu$m radius requires 6.7 minutes, during which time it is more likely to undergo detrainment or settling out of the cloud top region. Again, an accuracy of 3 $\mu$m appears sufficient to monitor large effects on radiative-microphysical interaction.

Implementation of remote sensing methods requires knowledge or assumptions on both the horizontal and vertical structure of the atmospheric constituents which cause extinction between the sensor and the cloud surface. Water vapor is the most important of these constituents. However, the estimates of water vapor contents obtained at remote locations using satellite data are limited in accuracy to approximately 20% of the column-integrated water vapor amount. Use of cloud observations within the water vapor window bands therefore minimizes the uncertainty in cloud radiance that would be associated with water vapor extinction effects. The spectral bandwidths of the primary near-infrared windows utilized for this study are 0.82–0.86 $\mu$m and 1.61–1.66 $\mu$m. The potential error in satellite-derived reflectance estimates due to atmospheric extinction in these near-infrared

water vapor windows is small, according to the results of a standard atmospheric transmission model. LOWTRAN model calculations were made of atmospheric extinction through a standard sub-tropical atmosphere and a saturated marine boundary layer. The effective water vapor path length was set at ten times the actual water vapor path to account for cloud multiple scattering. The multiple scattering effect on increasing photon path lengths is actually less than this, according to work reported by Kim (1983); the factor of ten was chosen to accentuate the vapor extinction. The resulting values of absorption due to water vapor are 1.6% of spectral solar irradiance in the 1.61–1.66 $\mu$m band, and less than 0.7% in the 0.82–0.86 $\mu$m band. Because the majority of this absorption occurs within the cloudy layer, observations of cloud from above must treat this error differently if the observing instrument is at cloud top rather than at spacecraft altitude. In either case, an estimate of the water vapor extinction could be applied to the measurements. The impact of small potential errors such as these in the values of observed reflectance will be discussed within Chapter 2.

Due to the constant evolution of cloud layers, we must also address the desired spatial and temporal resolution of satellite observations. The spatial resolution available from the operational meteorological satellites (approximately 1 km) will be related to the observed variability of cloud structure. The temporal resolution of data available from polar-orbiting or geostationary spacecraft is controlled by the limitations on viewing geometry in using the results of cloud reflectance models. Off-nadir observations introduce the additional complexity to the models due to azimuthal asymmetry of reflectance from clouds, but an inability to utilize these data from the satellites would hamper widespread sampling of the daytime evolution of the cloud layer spectral radiance. We have concentrated our analysis on nadir reflectance, which matches the available aircraft measurements and which corresponds to a subset of the data which will be provided twice daily from each of the new NOAA spacecraft AVHRR instruments. The more uncertain effects of off-nadir viewing are discussed only briefly in this study, and can be more effectively evaluated when the satellite data become available.

## 1.4 Identification of spectral windows in the near-infrared

Although near-infrared radiation is not detectable by the human eye, it comprises nearly half of the available solar flux reaching the lower atmosphere and surface, and thus acts as a significant source for atmospheric energetics and instrumented remote sensing of clouds. Spectral (*e.g.* narrow waveband or monochromatic) bands of strong atmospheric shortwave transmission exist in the near-infrared (NIR; defined as the 0.7–3.0 micrometer waveband), due to negligible water vapor absorption near 0.85, 1.05, 1.20, and 1.60 $\mu$m (respectively 11725, 9524, 8333, and 6250 cm$^{-1}$). The spectral intervals corresponding to the strong transmission are termed water vapor windows. Absorption by other atmospheric gases is also small in these intervals. Transmittances through a model cloud-free atmosphere are shown in Figure 1.1 for the bands located at 9524, 8333, and 6250 cm$^{-1}$. A slightly opaque water vapor window exists near 2.2 $\mu$m (4545 cm$^{-1}$). Cloud reflectance in the spectral windows can be theoretically modeled, given several assumptions, using only the cloud droplet size distributions and the size-dependent scattering properties for the droplet population. The interdependence of multiple scattering and the effective path length through in-cloud water vapor is minimized, so that cloud reflectivity is governed by the scattering (and absorption) characteristics of the hydrometeors alone.

The spectral reflectance ($\rho_\lambda$) is calculated from the ratio of upward spectral radiance ($L_\lambda^+$) and downward spectral irradiance ($E_\lambda^-$). Use of the water vapor windows to define the spectral bands limits the extinction of both downwelling solar flux and backscattered cloud radiance. The ratio is made non-dimensional by multiplying the upward radiance term in the numerator by $\pi$, creating an equivalent isotropic upward irradiance. Thus, we have

$$\rho_\lambda = \frac{\pi L_\lambda^+}{E_\lambda^-}, \tag{1.2}$$

where $\lambda$ denotes the narrow spectral bandwidth or monochromatic wavelength for which the calculation is valid. The symbol $L$ is used for radiance (units W m$^{-2}$ sr$^{-1}$) in accordance with the standard terminology suggested by the International Association of Meteorology and Atmospheric Physics (IAMAP) Radiation Commission (Raschke, 1978),

and these standards are used throughout the text. Therefore, conventions not necessarily common, such as the use of $\delta$ for optical depth and the superscript + for upward-directed radiation, are found here.

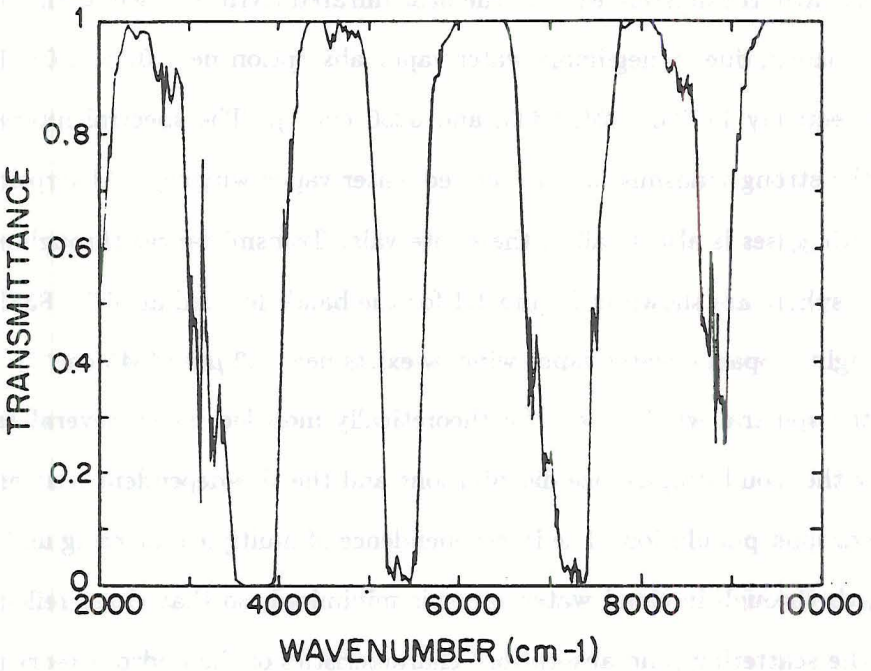


Figure 1.1: Spectral transmittance through a 1 cm sea-level path of water vapor, from a version of LOWTRAN using high spectral resolution gaseous absorption coefficients (Davies *et al.*, 1984).

Aircraft radiometer systems can be used to measure spectral radiances for clouds with differing cloud particle characteristics. This capability allows potential satellite remote sensing methods to be tested prior to the launch of a satellite-borne system. Hansen and Pollack (1970) presented theoretical evidence based on the doubling method, as well as some observations, to suggest that variations in terrestrial cloud microphysical structure (in particular, hydrometeor phase and size) could be estimated from spectral reflectance measurements in the near-infrared if optical depth was known. The coefficient of ab-

sorption for ice is greater than that for water in the spectral regions 1.5-1.8 $\mu$m (as well as 2.05-2.20 $\mu$m), which causes ice clouds to appear darker than water clouds under the same illumination. The remote sensing potential for discriminating between the ice and water phases of clouds was studied with airborne instruments (Kyle *et al.*, 1978), and then during a Defense Meteorological Satellite Program (DMSP) short-term experiment using a 1.6 $\mu$m narrowband sensor (Bunting and d'Entremont, 1982). The next series of NOAA polar-orbiting satellites, scheduled for first launch in the 1990's, will carry an AVHRR sensor which includes a 1.6-micrometer narrowband sensor. This sensor will be operated during the daylight hours, while the 3.7-micrometer channel will be operated at night. The new near-infrared window channel will provide the opportunity to discriminate between ice cloud, water cloud, and snow. The data will also allow the continued study of relationships between cloud reflectance and particle size. The theoretical basis for a correspondence between spectral reflectance and droplet size is discussed in the next section. Field experiments to date which have examined this relationship are also summarized. We identify the contributions of this dissertation research during and following the discussion.

## 1.5 Relationship of cloud reflectance to cloud microphysical structure

### 1.5.1 General characteristics of scattering from a cloud layer

The absorption by water droplets of radiative energy in the NIR water vapor windows provides the opportunity to observe water cloud radiance characteristics under the primary influence of droplet extinction processes. At wavelengths such as 1.6 and 2.2 $\mu$m, energy is absorbed almost exclusively by the cloud droplets. Outside of the window regions, contribution to absorption by droplets is much smaller, due to extinction by water vapor. Work by Davies *et al.* (1984) with a multiple scattering model at high spectral resolution demonstrates the controlling influence of droplet absorption on energy transfer within the water vapor windows bands.

Cloud extinction is primarily determined by the droplet size distribution within the multiple scattering layer. In the geometric optics limit (van de Hulst, 1981) , for which the size parameter of a sphere ($\chi = \frac{2\pi r}{\lambda}$) is large and $n_i$ is small ($n_i$ is the imaginary refractive

index for the droplet), Bohren and Barkstrom (1974) derived an expression for the energy absorbed by a droplet as a function of incident flux, geometric cross section, and the path length within the droplet. Total absorption is proportional to the product of droplet cross sectional area and droplet radius (and also proportional to droplet volume). Thus, for a given amount of incident energy, the absorbed component may be expected to increase with droplet size. Twomey and Bohren (1980) used this argument with similarity scaling and H-function arguments for semi-infinite layers (Chandrasekhar, 1950) to suggest a measurable relationship between mean droplet radius and cloud absorption. Twomey and Cocks (1982) discuss unresolved disparities between the observed and predicted droplet sizes based on theoretical relationships between mean droplet size and cloud reflectance. The measured reflectances were considerably higher than those predicted from radiative transfer modeling for the wavelength 2.25 $\mu$m, and lower for the wavelengths 0.75, 1.0, and 1.2 $\mu$m. However, they based their theoretical analysis on the simplification of a monodisperse population of droplets. Secondly, the H-function analytical solutions to the radiative transfer equation assume that the cloud layers are semi-infinite. The authors suggest possible causes for the discrepancy between model results and measurements, including cloud inhomogeneity and non-pure water composition, but conclude that their results show deviations which are opposite to those expected under those influences. The use of monodisperse droplet populations to derive their expected cloud reflectance, and the choice of mean droplet size as the retrieved parameter may also limit the agreement of their theoretical results and the observations.

King (1986) has used a NASA scanning multichannel radiometer (Kyle *et al.*, 1978) to investigate the use of shortwave cloud reflectance to estimate the optical depth. Simulated phase functions based on a fair weather cumulus droplet size distribution, and alternatively the Henyey-Greenstein assumption, were applied to reflectance observations above an optically thick convective cloud in Oklahoma. His analysis shows that large differences in derived optical thickness may result from varying the choice of the phase function model used to represent the droplet size distribution for the cloud. Thus, the use of monodisperse or other non-representative droplet size distributions can lead to incorrect

relationships between the droplet size parameters and cloud reflectance. In Chapter 2, polydisperse analytical size distributions based on the gamma function are utilized to provide an accurate representation of cloud scattering characteristics.

The effective radius ($r_e$) is a scalar parameter of a polydisperse droplet size distribution which is directly related to cloud scattering. This is shown by the following argument. Again under the assumption of large size parameter, an effective radius for scattering by a droplet population can be defined by integrating the scattering coefficient ($\beta_{sca}$) over the size distribution ($n(r)dr$). Following Hansen and Travis (1974),

$$\beta_{sca} = \int \pi r^2 Q_{sca}(\chi, m) n(r) dr \tag{1.3}$$

is used to define the effective radius for scattering,

$$r_{sca} = \frac{\int r \pi r^2 Q_{sca}(\chi, m) n(r) dr}{\int \pi r^2 Q_{sca}(\chi, m) n(r) dr}. \tag{1.4}$$

In this equation, m is the complex refractive index and $Q_{sca}$ is the scattering efficiency. If $Q_{sca}$ can be assumed to approach its asymptotic value of 2, as it does for cloud droplet populations when the wavelength of incident radiation is less than approximately 2 $\mu$m and droplet effective radius is greater than 4 $\mu$m, we have

$$r_e = \frac{\int \pi r^3 n(r) dr}{\int \pi r^2 n(r) dr}, \tag{1.5}$$

which can be obtained from the size distribution alone.

Curran and Wu (1982) employed the NASA multichannel radiometer to present an analysis of cloud particle phase and effective radius based on near-infrared reflectance measurements. Their retrieval method utilized spectral radiance observations at 0.85 $\mu$m to provide a measure of scaled optical depth,

$$\delta' = (1 - g)\delta, \tag{1.6}$$

where g is the asymmetry parameter of the droplet size distribution and $\delta$ is the optical depth of the cloud layer. The $\delta'$ scaling combines effects due to cloud extinction and asymmetric droplet scattering. It can be considered as a weighting for the contribution

to extinction by backscattering for a given cloud. The scaled optical depth, when plotted against reflectance in one of the spectral windows with significant droplet absorption (1.6 $\mu$m or 2.1 $\mu$m), was then used to infer the similarity parameter,

$$s = \sqrt{\frac{1-\omega_0}{1-g\omega_0}}, \tag{1.7}$$

where $\omega_0$ is the single scattering albedo of the droplet size distribution. The similarity parameter is very closely related to the effective radius of the size distribution, so that effective radius is retrievable from the coincident measurements of cloud radiance at 0.83 and 1.6 (or 2.1) $\mu$m. There is some variability in the correspondence of effective radius to the similarity parameter (and thus to cloud reflectance), which is due to the variance of the size distribution. The influence of size distribution variance is explored further by this dissertation. The aircraft remote sensing observations made by Curran and Wu (1982) implied particle size and phase changes for different cloud layers sampled. However, the authors were not able to validate the microphysical conditions within these clouds. The research presented in this disseratation includes a direct comparison of cloud microphysical measurements and estimates of droplet size obtained from cloud bispectral radiance observations.

Stephens and Scott (1985) describe a spectral radiometer developed at CSIRO in Australia, which was later expanded to measure radiances throughout the shortwave. Stephens and Platt (1987) have carried out field measurements of cloud reflectance with this radiometer and have found, in contrast to Twomey and Cocks (1982), that measured values were smaller in the NIR windows than theoretically calculated values. These authors complete their discussion by suggesting that cloud composition may account for this discrepancy, and they call for additional studies on the effects of variable cloud structure and neglected absorbers. The research reported here contributes to the knowledge of these effects, as described below.

### 1.5.2 Effects of inhomogenous cloud structure

The radiative models used in the previously described studies have treated clouds as horizontally homogenous, vertically uniform and/or optically thick. Cloud distributions

typically show scattered conditions and clear areas due to convective and mesoscale organizing features. In particular, marine stratiform clouds are often comprised of individual cellular elements of limited optical thickness. The horizontal and vertical inhomogeneity of cloud structure is a source of error in reflectance calculations. This dissertation contains model evaluation of the effects of each of these types of inhomogeneity for marine stratus.

Droplet size measurements within overcast stratus and stratocumulus clouds demonstrate that the microphysical parameters of these populations fluctuate between cloud levels and less so along horizontal tracks (Noonkester, 1984). The magnitudes of effective radius generally lie within the range 3-15 $\mu$m. Similar microphysical conditions were observed in the field data obtained for this project, including the presence of a double mode of the droplet size distributions. Several hypotheses exist on the mechanisms for evolution of droplet distributions, including the entrainment of dry air at cloud top (Telford *et al.*, 1984; Hill and Choulartan, 1985), incomplete turbulent mixing leading to locally increased supersaturation (Baker *et al.*, 1984), and entrainment of cloud condensation nuclei (Warner, 1973; Lee *et al.*, 1980). Work by Welch *et al.* (1980) demonstrated that values of cloud hemispheric reflectance and absorptance may change significantly with the presence of enhanced concentrations of large droplets, even when the cloud optical thickness is held constant. The influence of droplet size distribution on the wavelength-specific cloud radiance is studied here by use of both analytic and measured size distributions, and inclusion of the effects of vertical inhomogeneity within the cloud.

Cloud shape exerts control over spectral reflectance by altering the angular distribution of upward radiance (McKee and Cox, 1974; Davies, 1978). As the area of cloud-breaks and cloud sides increases, energy directed horizontally has less chance of being re-scattered upward or downward. Cloud hemispheric reflectance and transmittance measured from above and below cloud differs from the idealized layer cloud. Therefore, breaks in the cloud cover and cloud-top striations can cause an "apparent" cloud absorption ( Ackerman and Cox, 1981).

Results of single-cloud Monte Carlo modeling demonstrate that significant variations in cloud extinction due to finite cloud effects occur in the NIR as well as the visible (Davies

*et al.*, 1984). However, angular patterns of scattering from broken cloud fields (Welch and Wielicki, 1984) show that photons exiting cloud sides require considerable distance ($> 0.5$ km) from neighboring clouds in order to avoid interaction (*i.e.* secondary scattering and absorption). That study was limited to visible wavelengths and the attendant negligible droplet absorption. Comparison of simulations for near-infrared reflectance from homogenous and scattered stratocumulus was undertaken for the research reported here.

Foot (1988) shows that narrow-band reflectance measured in the near-infrared water vapor windows suggests a larger effective radius than was measured by his aircraft cloud physics instrumentation. This was not explained by model simulations which included aerosol or the effects of overlying thin cirrus. He carried out Monte Carlo model simulations of uneven cloud tops, and found that narrow turrets (100 m in depth, seperated by 25 m) allowed preferential reduction in reflectance for the 2.01 $\mu$m window relative to the 1.55 $\mu$m window, which were used in combination to infer effective radius changes. This reduction at the wavelength of stronger water absorption leads to the increased droplet size estimate. It was not possible to verify that the narrow turrets existed at a 25 m spacing, because of the aircraft sampling rate. This situation emphasizes the difficulty in obtaining and representing the "complete" variability in cloud structure for comparison with model results. In this dissertation, we evaluate the sensitivity of retrieved droplet size to cloud structure variations, so that the applicability of the retrieval method can be based on accepted error levels. The analysis of differences between the angular reflectance of plane parallel and non-uniform cloud fields in the water vapor window wavelengths is addressed in Chapter 3.

### 1.5.3 Aerosol and mixed-component droplet populations

Uncertainties in the analysis of cloud reflectance also arise for the cases where non-pure water droplets, interstitial (between droplets) aerosol, or external haze layers accompany the cloud (Newiger and Bähnke, 1981). A program of combined modeling and measurement of the radiation budget for Arctic stratus, carried out by Herman and Curry (1984), provides evidence on the role of soot-containing aerosol above and within cloud. They found the ratio of diffuse to direct solar radiation components notably enhanced at

cloud top due to multiple scattering by aerosol above cloud. Significant extinction can be caused by the aerosol population. In this manuscript, the term 'aerosol' will refer to dry or hydrated particles with radii less than 2.0 $\mu$m, since this is the minimum size at which a (pure) water droplet normally requires negligible supersaturation to become activated (Wallace and Hobbs, 1977). Aerosol at sub-saturated conditions within the marine boundary layer (MBL) is often hydrated due to deliquescence.

Measurements of aerosol extinction specifically at NIR wavelengths are scarce, particularly for marine layer aerosol. The mass concentration for aerosol in cloud is small compared to that for liquid water, but the aerosol may absorb more solar radiation per unit volume. This is because the imaginary part ($n_i$) of the refractive index ($m = n_r - in_i$) can be orders of magnitude larger for aerosol than water spheres in the shortwave (Weiss *et al.*, 1980). Information of this type is summarized by Shettle and Fenn (1979), indicating that soot and dust-like aerosol are gray absorbers (imaginary index of refraction is independent of wavelength) in the near-infrared, while oceanic aerosol, sea salt, and water solubles show more variation. The imaginary index of refraction is up to ten times as large for sea salt as for water in the near-infrared. At a wavelength of 1.6 $\mu$m, $n_i$ is equal to 0.0001 for water, 0.00065 for sea salt, 0.02 for water soluble aerosol, and 0.48 for soot. Chýlek *et al.* (1984) show that soot loadings on the order of 0.3 $\mu$g m$^{-3}$ can produce a 20% reduction in reflectivity of an optically thick stratus layer at visible wavelengths. However, the effect is smaller in the near-infrared. The majority of atmospheric aerosols have $n_i$ values lower than soot, and therefore the effects on cloud reflectivity are expected to be less significant.

The extinction characteristics of marine aerosol are highly dependent on the local relative humidity. As the relative humidity increases, the aerosol hydrates and this haze droplet scatters more of the incident solar radiation. The single scattering albedo ($\tilde{\omega}$) describes the probability that a photon will not be absorbed in a scattering event. It is measurable as the ratio of the scattering coefficient to the sum of scattering and absorption coefficients. The ($\tilde{\omega}$) of a maritime aerosol population with $n_i = 0.132$ for wavelength $\lambda =$ 2.0 $\mu$m changes from 0.75 at relative humidity RH = 85%, to 0.94 at RH = 99% (Hänel,

1976). Podzimek (1982) lists the fluctuation in mean marine aerosol refractive indices at a 0.589 $\mu$m wavelength at relative humidities of 20% and 96% : $n_i$ decreases from 0.047 to 0.003 and $n_r$ decreases from 1.55 to 1.35 as the aerosol is subjected to the higher humidity.

The contribution of scattering to particle extinction is controlled by the real part of the refractive index ($n_r$). Typical values in the visible region are 1.33 (pure water), 1.49 (sea salt), and 1.53 (continental dust). As droplet scattering is enhanced, the solar radiation is directed more significantly back toward space and forward to the cloud layer. Size distributions of droplets and aerosol, and their column-integrated concentrations, determine the net flux at any given location. Above cloud, aerosol layers may become even more important in the radiation balance when they contain high concentrations of particulate alone or in aqueous solution. The influence on cloud reflectance of aerosol within and above cloud layers is explored in Chapter 3.

## 1.6 Objectives of this research

The primary goal of this research is to contribute to the development of a satellite remote sensing technique for estimating cloud droplet size in marine stratus clouds. The specific objectives of the present work are;

(1) to develop an objective technique for estimating the effective radius within a cloud layer,

(2) to determine the magnitudes and uncertainties of cloud droplet size estimates due to variations in stratiform cloud structure,

(3) to use measurements of cloud spectral reflectance to test the theoretical relationships between droplet size and reflectance, and

(4) to apply the results from the above to make recommendations on an operational remote sensing method for droplet size in marine stratus.

## 1.7 Research strategy

The methods for addressing the objectives of this research include both numerical modeling of radiative transfer in clouds, and aircraft measurement of cloud microphysical

structure and radiances. The first specific objective of the research is to determine how the quantitative relationships between droplet size and spectral reflectance can be used in an objective estimation method. In Chapter 2, we will consider the physical basis of a passive remote sensing retrieval method for droplet size, including the use of effective radius for the retrieved size parameter and the necessity of using measured radiance in more than one spectral band. An objective method for estimating effective radius is developed, utilizing analytical droplet size distributions based on the gamma function. A radiative transfer model known as the adding-and-doubling method is applied, in order to obtain the theoretical results which the objective retrieval method employs.

The second goal of this work is to identify the range and uncertainty in estimated $r_e$ values in the upper cloud regions providing the remotely observed cloud reflectance. In Chapter 3, we discuss the impact on droplet size estimates of varying cloud composition and structure. Cloud reflectance relationships for cloud layers characterized by different values of effective radius and variance are presented. The presence of aerosol constituents and of differing cloud sublayers are simulated for horizontally homogeneous cloud, and the error in droplet size estimates for these cases is determined. The Monte Carlo method of radiative transfer calcuations is also applied, in order to represent the effects of horizontally inhomogenous cloud on spectral reflectance.

The third objective of the research is to test the retrieval method using radiometric and microphysical measurements from field observations. The methods and results of the measurement programs are discussed in Chapter 4, with additional information located in Appendix A. Sampled microphysical parameters are used to characterize droplet size within the clouds, and spectral reflectances and reflectance ratios are used to estimate droplet size. Similarities and differences between the droplet size measurements and estimates are discussed.

The fourth objective of this study, addressed in Chapter 5, is to make recommendations on the operational use and further testing of a droplet size retrieval technique. The chapter will provide a summary of the present research, conclusions on the expected success of $r_e$ estimation from satellite data, and an outline for the next needed research steps.

## Chapter 2

# DEVELOPMENT OF AN OBJECTIVE RETRIEVAL METHOD

## 2.1 Introduction

The studies described in Chapter 1 (Hansen and Pollack, 1970; Twomey and Bohren, 1980; Curran and Wu, 1982) suggest that the droplet size of a sufficiently homogeneous cloud layer may be retrievable from measurements of reflectance in a near-infrared water vapor window band, given an accurate estimate of cloud optical depth against which to normalize the cloud brightness. The scaled optical depth was introduced by Curran and Wu (1982) in order to correct for the effects of the asymmetry parameter on cloud scattering, and because this parameter can be closely estimated from measurements near 0.83 $\mu$m. The method which is developed in this chapter utilizes numerical model results of cloud reflectance a 0.85 $\mu$m to determine scaled optical depth, and reflectance at 1.6 $\mu$m to indicate the size-specific absorption by cloud droplets. Other shortwave bands can be used to determine the scaled optical depth as long as they also lie in water vapor windows and have small values of the spectral extinction parameters for aerosol and cloud. A measurement at 0.65 $\mu$m could be applied; however, this wavelength is within the Chappuis ozone absorption band (0.45–0.75 $\mu$m), and this radiation is also more susceptible to extinction by aerosol. Thus, we will utilize the 0.85 $\mu$m spectral observations to estimate the scaled optical depth, and the 1.6 $\mu$m wavelength to identify size-specific cloud absorption.

## 2.2 Rationale for choice of simulation methods

The prediction method is based on the numerical simulations of the reflectance properties of idealized cloud layers with predefined size distributions and a large range of values of optical depth. The radiative transfer scheme chosen to simulate the cloud was required

to determine cloud radiance through a multiple scattering layer, for a viewing angle at or near nadir. We employed the "Adding" method, described in the following section. This model also allowed simulation of clouds composed of differing layers, so that the retrieval method could be tested for vertically inhomogeneous cloud and aerosol.

Hansen's (1971b) modified gamma function was chosen as the model for the droplet size distributions to generate the predictor relationships between effective radius, scaled optical depth and bispectral (at 0.85 and 1.6 $\mu$m) reflectances. The gamma function is frequently used to represent droplet size distributions. The Hansen modified gamma function is defined by the effective radius and the effective variance, such that water droplet size distributions with equivalent values of these parameters will have equivalent extinction properties (Hansen, 1971b). The expressions for the modified gamma distribution and the effective variance are given in Section 2.5, where we discuss how the effective radius and effective variance control cloud near-infrared reflectance at a given value of scaled optical depth.

Cubic spline interpolation is used to predict the scaled optical depth from the 0.85-$\mu$m reflectance, and to then predict the effective radius, for two values of the effective variance which bracket the observed range of this parameter in sampled clouds. Results are presented in this Chapter which demonstrate the sensitivity of retrieved droplet size to potential uncertainties in solar angle. In operational use, either an interpolation between results for a given set of solar angles could be used, or the calculation of original predictor curves for the family of gamma distributions could be carried out for the exact angles. The Adding method and the interpolation procedure were selected in part because, when combined, they are still computationally simple enough to integrate into a realtime prediction technique.

## 2.3 Description of the adding model

The Adding method of representing multiple scattering characteristics described by Grant and Hunt (1968) was used to simulate stratiform clouds composed of single and multiple layers. In this method, the principles of invariance for monochromatic radiative

transfer are applied to energy exchange between plane-parallel, vertically adjoined layers. One major advantage of the adding method is the ease of representing multiple cloud or aerosol layers in the atmosphere. This increases the computational requirements only moderately and allows simulation of several different particle size distributions, optical depths and extinction coefficients. Within each individual layer the single scattering albedo and phase function are assumed constant, and the azimuthally-averaged radiance at the boundaries of a layer composed of $n+1$ identical sublayers (optical depth limits of 0 to $\delta$) is given by

$$L_{n+1}^{-} = t(n+1,1)L_1^{-} + r(1,n+1)L_{n+1}^{+} + \Sigma^{-}(n+1,1) \tag{2.1}$$

$$L_1^{+} = r(n+1,1)L_1^{-} + t(1,n+1)L_{n+1}^{+} + \Sigma^{+}(1,n+1). \tag{2.2}$$

$L$ and $\Sigma$ represent vectors of resultant and source radiances, respectively, at specified zenith (polar) angles. The $r$ and $t$ are reflection and transmission matrices, respectively.

Angular discretizations with quadrature formulae are used to approximate integrals for flux. The reflection matrix ($r$) and transmission matrix ($t$) are determined by first "doubling" the optical depth of multiple homogeneous layers until the desired $\delta$ limit is reached. Hence, this method is also often referred to as the adding-and-doubling (AD) model. The model formulation for this study accomodates vertical variations in the droplet size distributions and extinction parameters which specifically match observed microphysical conditions.

The infinitesimal generator initialization method of Wiscombe (1976b) is used to determine reflection and transmission matrices for the first sublayer of cloud (extremely small optical depth, $\triangle\delta = 10^{-4}$), following

$$r_0 = \frac{\tilde{\omega}}{2}\Upsilon^{-1}P^{-+}C\triangle\delta \tag{2.3}$$

$$t_0 = U - [\Upsilon^{-1}(U - \frac{\tilde{\omega}}{2}P^{--}C)]\triangle\delta \tag{2.4}$$

with the initial diffuse source radiation supplied from the forward ($P^{--}$) and backward ($P^{-+}$) scattering matrices integrated over the vector of direction cosines ($\Upsilon$) for the quadrature angles with integration coefficients $C$. $U$ represents the identity matrix.

The source matrices are derived from an initial direct solar source

$$\Sigma_0^{\pm} = \frac{\mu_0 E_0 \tilde{\omega}}{4\pi} \Upsilon P_0^{\pm} C(1 - e^{\frac{-\triangle\delta}{\mu_0}}) \tag{2.5}$$

where $E_0$ is the direct beam solar irradiance at vertical incidence, propagating from the zenith direction $\theta_0 = \arccos(\mu_0)$. This passes through the initial optical depth increment ($\triangle\delta$) and is scattered into the quadrature directions according to the magnitude of the single scattering albedo and the phase function matrix of forward ($P_0^-$) and backward ($P_0^+$) scattering. Subsequent diffuse source terms for incremental layers are given, following Wiscombe (1976a), by

$$\Sigma^-(n+1,1) = t(1,n)[1 - r(1,n)(1,n)]^{-1}[e_n r(1,n)\Sigma^+(1,n) + \Sigma^-(1,n)] + e_n \Sigma^-(1,n) \tag{2.6}$$

$$\Sigma^+(1,n+1) = t(1,n)[1 - r(1,n)r(1,n)]^{-1}[r(1,n)\Sigma^-(1,n) + e_n \Sigma^+(1,n)] + \Sigma^+(1,n) \tag{2.7}$$

with

$$e_n = exp\{\frac{-2^n \triangle\delta}{\mu_0}\}. \tag{2.8}$$

After the final reflection, transmission and source terms are determined for each homogeneous layer, "adding" these layers is accomplished by using their individual $r$ and $t$ sub-matrices in the recursion relationships

$$L_{n+1}^- = r(1,n+1)L_{n+1}^+ + V_{n+1/2}^- \tag{2.9}$$

$$L_n^+ = \hat{t}(n,n+1)L_{n+1}^+ + V_{n+1/2}^+ \tag{2.10}$$

where

$$\hat{t}(n,n+1) = T_{n+1/2} t(n,n+1) \tag{2.11}$$

$$T_{n+1/2} = [U - r(n+1,n)r(1,n)]^{-1} \tag{2.12}$$

$$r(1,n+1) = r(n,n+1) + t(n+1,n)r(1,n)[U - r(n+1,n)r(1,n)]^{-1} t(n,n+1). \tag{2.13}$$

Internal diffuse source vectors are given by

$$V^{-}_{n+1/2} = \hat{t}(n+1,n)V^{-}_{n-1/2} + \Sigma^{-}(n+1,n) + R_{n+1/2}\Sigma^{+}(n,n+1) \tag{2.14}$$

$$V^{+}_{n+1/2} = \hat{r}(n+1,n)V^{-}_{n-1/2} + T_{n+1/2}\Sigma^{+}(n,n+1) \tag{2.15}$$

These equations also use recursion to evaluate the sub-matrices

$$\hat{t}(n+1,n) = t(n+1,n)[U - r(1,n)r(n+1,n)]^{-1} \tag{2.16}$$

$$\hat{r}(n+1,n) = r(n+1,n)[U - r(1,n)r(n+1,n)]^{-1} \tag{2.17}$$

and

$$R_{n+1/2} = \hat{t}(n+1,n)r(1,n) \tag{2.18}$$

$$T_{n+1/2} = [U - r(n+1,n)r(1,n)]^{-1}. \tag{2.19}$$

Each homogeneous layer is "built down" upon preceeding layers from cloud top.

## 2.4 Assumptions and implementation

Each homogeneous layer of the model cloud has a specified droplet size distribution. Standard droplet size distributions compiled by Derr (1984) were applied in initial experiments, as were analytic size distributions based on the modified gamma function. In addition, microphysical data from airborne sampling in stratocumulus (Wetzel and Vonder Haar, 1986a) have also been used for the simulations in order to provide a wider range of droplet size distributions. Finally, droplet size distributions representing the cloud layers sampled during the 1986 field experiment were used in more specific model runs. These data are described in Chapter 4 and in the Appendix.

Mie scattering theory is used to calculate the single scattering albedo, asymmetry parameter, and extinction cross sections for each population, as well as the Mie phase function. The phase function based on the Henyey-Greenstein (H-G) analytic form was also used for comparitive purposes, as described later. The phase function may be numerically expanded in a finite number of terms which are functions of Legendre Polynomials. Thus,

$$P(cos\psi_s) = \sum_{n=0}^{N} (2n+1)\chi_n P_n(cos\psi_s). \tag{2.20}$$

$N$ is the order of expansion,and the $P_n$ identities are Legendre Polynomials for the value of $cos(\psi_s)$. The coefficients $\chi_n$ are the moments of $P_n$, given by

$$\chi_n = \frac{1}{2}\int_0^{\pi} P(cos\psi_s)P_n(cos\psi_s)sin\psi_s d\psi_s. \tag{2.21}$$

The coefficients of the Legendre Polynomials are calculated through the Mie scattering code.

A difficulty lies in attempting to represent the phase function in an analytic form, because of the strong forward and backward peaks. Wiscombe (1977) developed the delta-M expansion for this Legendre form in order to more correctly represent the strongly peaked scattering patterns of cloud droplet distributions:

$$P^*(cos\psi_s) = 2f\delta_f(1-cos\psi_s) + (1-f)\sum_{n=0}^{2M-1} (2n+1)\chi_n^* P_n(cos\psi_s). \tag{2.22}$$

The delta-function $\delta_f(1-cos\psi_s)$, not to be confused with optical depth $\delta$, is formally defined to be an integration over the limits of the term $cos\psi_s$. In usage here, the delta function is equal to unity if the argument $(1-cos\psi_s)$ is equal to zero, and is defined as zero otherwise. Thus, the phase function is composed of a contribution from the forward peak ($cos\psi_s = 1$) and a summation of terms accounting for all other scattering angles. $M$ is the number of angles at which the phase function will be determined. The new expansion coefficients are introduced to rescale the energy remaining outside the forward peak, using

$$\chi_n^* = \frac{\chi_n - f}{1-f}. \tag{2.23}$$

$f$ is defined as the truncated energy fraction. While the selection of $f$ is somewhat arbitrary, Wiscombe (1977) suggests that

$$f = \chi_{2M} \tag{2.24}$$

provides a consistent usage, since $f$ will decrease as the number of phase function angles ($M$) increases.

The spectral reflectance is here defined as a directional reflectance factor for hemispherical incidence at a monochromatic wavelength. It is calculated from

$$\rho_\lambda = \frac{\pi L_\lambda^+}{E_\lambda^-} \tag{2.25}$$

where $\lambda$ denotes the wavelength for which the calculation is valid. $L_\lambda^+$ is the upward spectral radiance at a specified quadrature angle which represents the viewing zenith angle of a sensor aloft. The term in the denominator is the downward spectral irradiance, which in the case of an isolated model cloud layer with no intervening atmosphere is equal to $\mu_0 E_{0\lambda}$. The solar spectral irradiance outside the atmosphere defines the parameter $E_{0\lambda}$, and in the radiative transfer model results this is scaled to unity. For calculations in which downward flux and upward radiance are obtained from measurements, an estimate of total spectral flux is placed in the denominator, and $L_\lambda^+$ is replaced by the measured upwelling spectral radiance.

The ocean surface albedo is assumed to be zero. The impact of surface reflectance is small in the shortwave for marine stratus, particularly where no breaks in the cloud layer are found. Nadir spectral reflectance of a planar ocean surface in any direction away from the area of sun-glint is not more than 2% in the visible, decreases into the near-infrared, and takes a sharp dip to below 1% between 2.4 and 2.7 $\mu$m (Stewart, 1985). This may increase when rough seas cause direct reflection from wave surfaces. Hemispherical (total) transmittance calculated from the adding-and-doubling method is typically not more than 30% at 0.85 $\mu$m and 1.6 $\mu$m wavelengths with solar zenith angle 50° for even small cloud optical depths (*e.g.* $\delta = 2$), and the diffuse transmittance portion of this is less than 5%, so transmission of shortwave energy reflected from the ocean is negligible unless cloud breaks allow considerable unattenuated irradiance to reach the ocean and the cloud layer itself has very small optical depth.

The solar zenith angles and observer view angles used for most of the model simulations were chosen to simulate typical remote sensing geometries for aircraft and satellite

viewing of marine stratus in the middle and lower latitudes. During the field observational program, solar zenith angles were in the range 30° to 60°. An eight-point Lobatto quadrature scheme was used to provide radiances (at 0°, 14°, 26°, 38°, 49°, 61°, 73°, and 84°), and a Gaussian scheme was used in some cases to provide radiances (at 8°, 19°, 30°, 41°, 52°, 63°, 74°, and 85°). The angles used in analysis were generally limited to those at or near nadir, for which aircraft observations were available. Monochromatic radiances obtained from the model are computed at the top and bottom of each cloud layer, for 8 angles in each half-hemisphere.

## 2.5 Model intercomparisons

Comparisons have been made of the AD model formulated for this study to other plane-parallel models published in the open literature. For example, results under similar conditions for a Rayleigh-scattering layer are plotted for this model and another (the matrix operator model used by Plass *et al.*, (1973)) in Figure 2.1. In both cases, $\tilde{\omega} = 1$, $g = 0.8$, and the solar zenith angle $(\theta_0) = 0°$. The plotted results are quite similar and at most points overlay each other, for a large range of layer optical depths. The model used in this study thus represents accurately the scattering and extinction by particles of small size parameter.

The Doubling model results of Joseph *et al.*, (1976) for layers representing clouds (using the Henyey-Greenstein phase function) were compared to this model, and found to be within 1% agreement on reflectance, transmittance, and absorptance. This is shown in Table 2.1 for variations of the parameters $\tilde{\omega}$, $g$, $\mu_0$, and $\delta$.

Discussion with another author (Stephens, personal communication) who provided guidance during the formulation of this model, also confirmed similar results to his version of the adding-and-doubling model (Stephens, 1978a). Finally, a check of spectral reflectance values obtained by Curran and Wu (1982) showed very good agreement.

Comparison of AD model runs from the Henyey-Greenstein phase function versus the Mie phase function was made. The H-G phase function has been commonly used for nearly 50 years (Henyey-Greenstein, 1941), beginning with application to interstellar dust, to represent forward-peaked scattering functions. It is expressed as

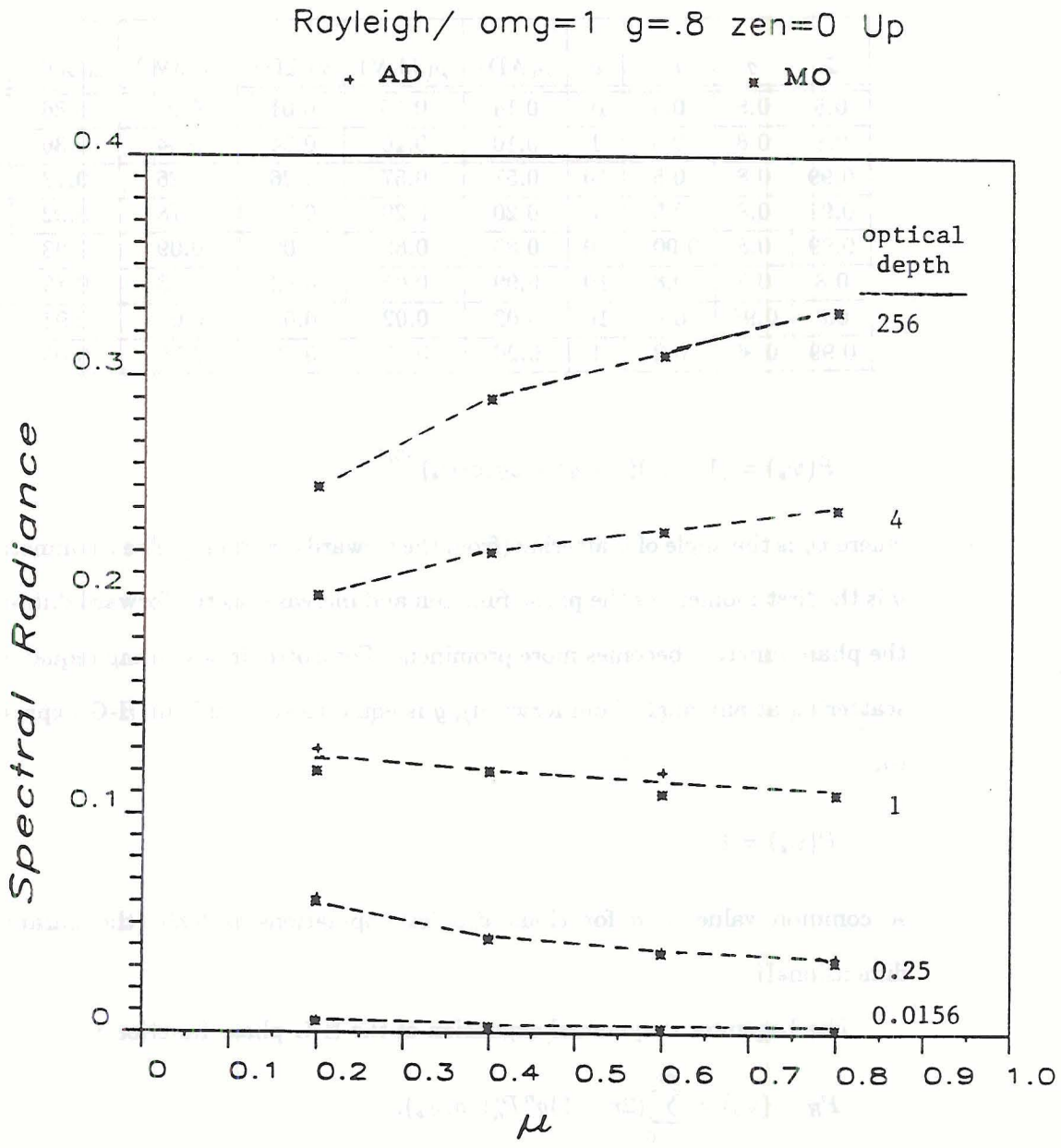


Figure 2.1: Reflectance as a function of the cosine of viewing angle ($\mu$) for Rayleigh scattering layers of optical depth 0.0156 - 256 from the results of the Matrix Operator and Doubling methods.

Table 2.1: Comparison of AD results to those of Joseph *et al.*, (1976), for reflectance ($\rho$), transmittance ($\tau$), and absorptance ($\alpha$).

| $\tilde{\omega}$ | $g$ | $\mu_0$ | $\delta$ | $\rho$(AD) | $\rho$(JJW) | $\tau$(AD) | $\tau$(JJW) | $\alpha$(AD) | $\alpha$(JJW) |
|---|---|---|---|---|---|---|---|---|---|
| 0.8 | 0.8 | 0.5 | 10 | 0.14 | 0.15 | 0.01 | 0.01 | 0.86 | 0.85 |
| 0.8 | 0.8 | 0.5 | 1 | 0.10 | 0.10 | 0.54 | 0.54 | 0.36 | 0.36 |
| 0.99 | 0.8 | 0.5 | 10 | 0.57 | 0.57 | 0.26 | 0.26 | 0.17 | 0.17 |
| 0.99 | 0.8 | 0.5 | 1 | 0.20 | 0.20 | 0.78 | 0.78 | 0.02 | 0.02 |
| 0.99 | 0.8 | 0.001 | 10 | 0.83 | 0.83 | 0.09 | 0.09 | 0.08 | 0.08 |
| 0.8 | 0.8 | 0.8 | 10 | 0.09 | 0.09 | 0.02 | 0.03 | 0.89 | 0.88 |
| 0.8 | 0.95 | 0.8 | 10 | 0.02 | 0.02 | 0.05 | 0.05 | 0.93 | 0.93 |
| 0.99 | 0.95 | 0.2 | 1 | 0.26 | 0.25 | 0.69 | 0.70 | 0.05 | 0.05 |

$$P(\psi_s) = (1-g^2)(1+g^2-2g\cos\psi_s)^{-3/2} \tag{2.26}$$

where $\psi_s$ is the angle of scattering (from the forward direction). The asymmetry parameter $g$ is the first moment of the phase function and increases as the forward diffraction peak of the phase function becomes more prominent. For isotropic scattering (equal probability of scattering at any angle from forward), $g$ is equal to zero and the H-G expression reduces to,

$$P(\psi_s) = 1 \tag{2.27}$$

A common value of $g$ for cloud droplet populations is 0.85 (the parameter is non-dimensional).

The Legendre Polynomial expansion of the H-G phase function is

$$P_{H-G}(\psi_s) = \sum_{n=0}^{\infty}(2n+1)g^n P_n^*(\cos\psi_s). \tag{2.28}$$

This is identical to the Legendre expansion given above, with the simplification that $\chi_n$ is equal to $g^n$. From Mie theory, $g$ is defined by an integration over a series of coefficients $a_n$ and $b_n$ which are determined from the elementary wave functions (based on Hankel and Bessel functions):

$$g = <\cos\psi_s> = \frac{4}{\chi^2 Q_s}\sum_{n=1}^{\infty}[\frac{n(n+2)}{n+1}Re(a_n a_{n+1}^* + b_n b_{n+1}^*) + \frac{2n+1}{n(n+1)}Re(a_n b_n^*)]. \tag{2.29}$$

In this equation the size parameter is given by $\chi$. $Q_s$ is the scattering efficiency for an individual sphere, and $a^*$, $b^*$ are the complex conjugates of $a$ and $b$.

The most noticeable differences in the results of the Mie versus the H-G phase function occur near nadir and near the horizon (Figure 2.2). The error induced by using the H-G assumption occurs throughout the range of optical depth, as shown in Figure 2.3 for a viewing angle near nadir. Due to the importance of near-nadir views for aircraft data analysis (and perhaps for satellite applications), it was determined that complete Mie phase function size distributions would be used in the numerical experiments, rather than simplifying the procedure by calculating only $g$ and $\tilde{\omega}$.

The model sensitivity to the eight-angle quadrature was examined by comparison to the results of 16-angle quadrature. As shown in Figure 2.4, misleading interpretation could be made near the horizon by extrapolating the last value in the 8-angle results upward. The higher order method displays slight limb darkening which the 8-angle version did not resolve. However, little information on the variation of reflectance with viewing angle is lost near nadir, where our study is concerned. Therefore the 8-angle quadrature, which is computationally faster, was used. The smooth transition from nadir to off-nadir reflectance results suggests small azimuthal dependence, such that small uncertainties in the viewing angle from nadir would not produce strong variations in the reflectance.

## 2.6 Cloud reflectance relationships for gamma size distributions

The range of $r_e$ reported in previous studies of marine stratiform cloud and sampled by the measurement programs reported in Chapter 4, is 3–15 $\mu$m. Larger values occur in precipitating stratiform cloud. The range of values of effective variance is 0.08–0.33. Several figures are presented here which demonstrate the variation in cloud near-infrared reflectance for $r_e$ values within the range of 3 to 30 $\mu$m, and for $v_e$ values of 0.1 and 0.3. The analytical functions used to establish these distributions are,

$$n(r) = Cr^{(1-3b)/b} e^{-r/ab} \tag{2.30}$$

where n(r)dr is the number of particles per unit volume with radius between r and r+dr (Hansen, 1971b), and

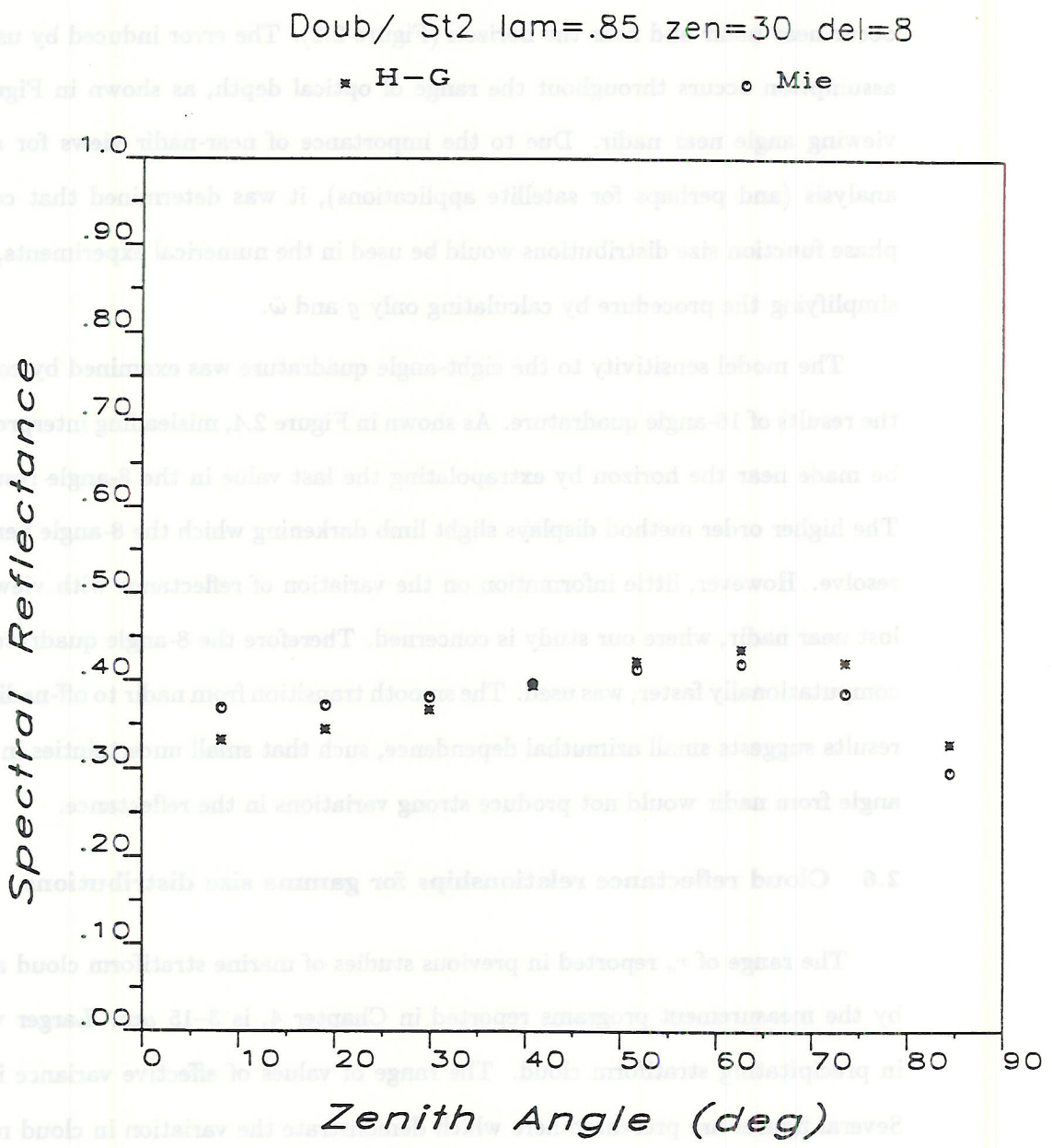


**Figure 2.2:** 0.85-$\mu$m reflectance as a function of viewing zenith angle. The Henyey-Greenstein and Mie phase functions are used to represent the Stratus 2 cloud.

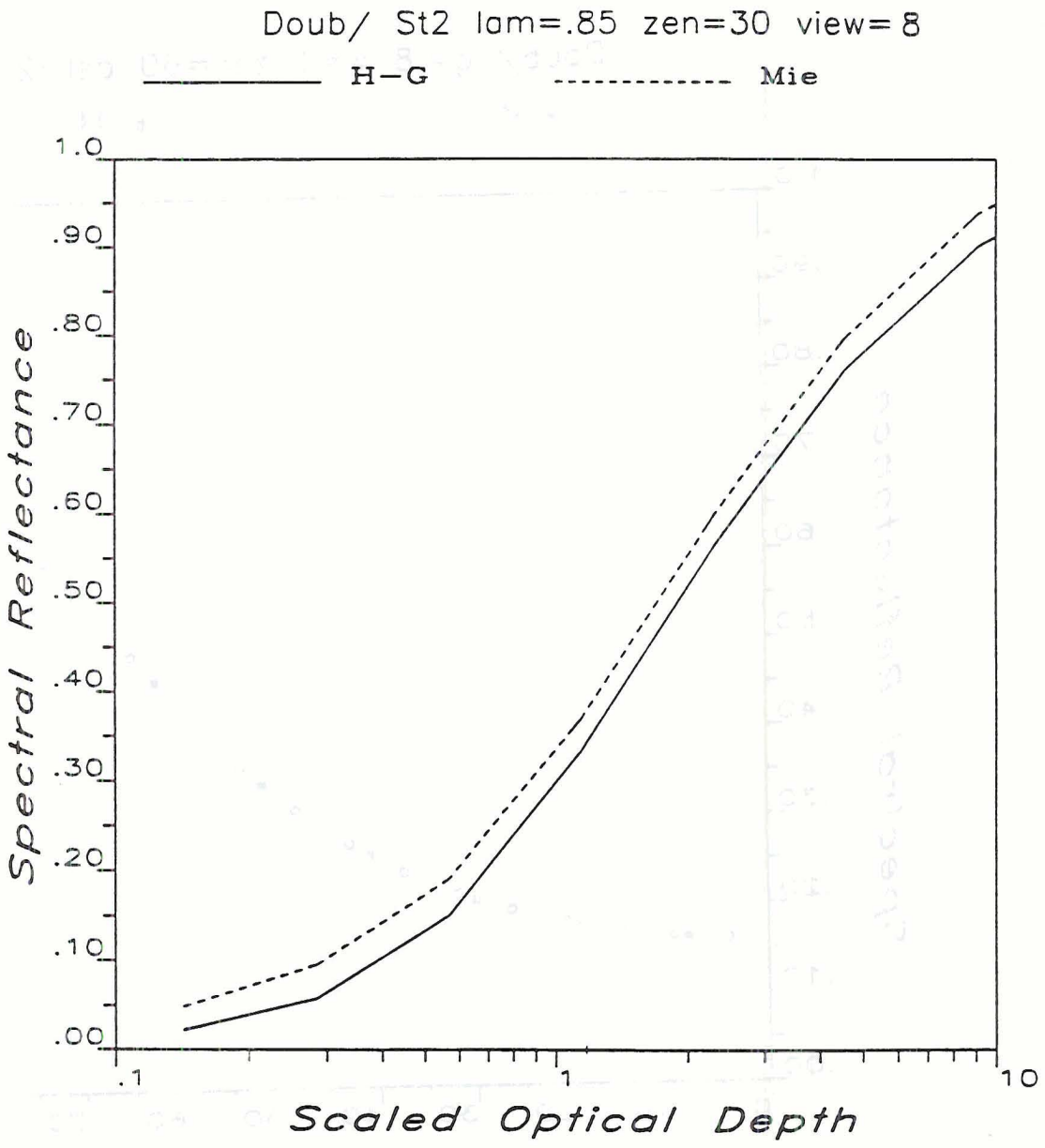


Figure 2.3: 0.85-$\mu$m reflectance as a function of scaled optical depth for Henyey-Greenstein and Mie phase functions.

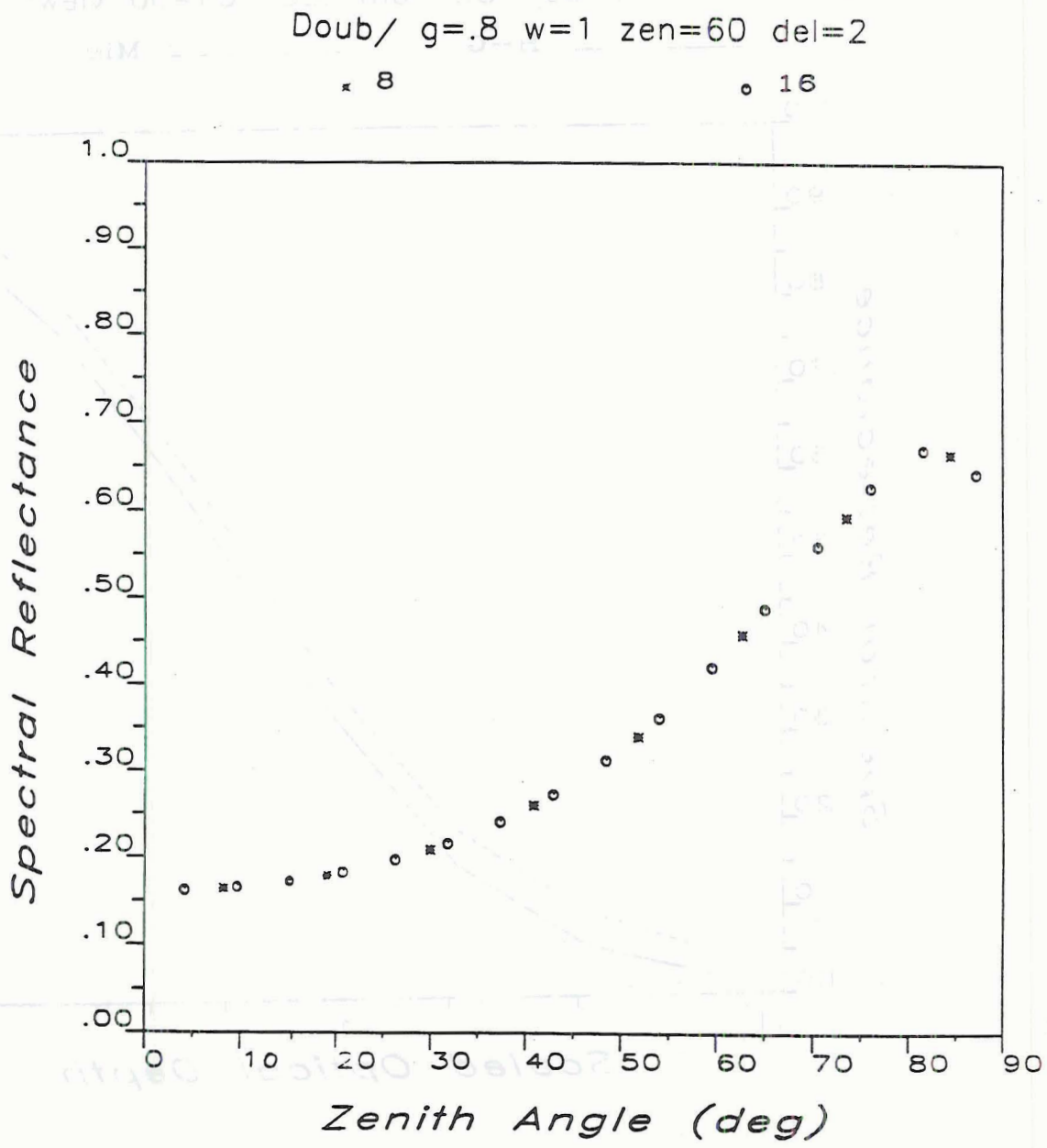


**Figure 2.4: Reflectance as a function of viewing zenith angle from model calculations using 8 and 16 quadrature angles.**

$$C = \frac{N(ab)^{(2b-1)/b}}{\Gamma[(1-2b)/b]}. \tag{2.31}$$

In these equations, a is the effective radius, b is the effective variance, N is the total particle concentration, and $\Gamma$ is the gamma function. Similar expressions based on the gamma function have often been used to represent cloud particle size distributions (Deirmendjian, 1964; Hansen and Pollack, 1970). The effective radius has been defined earlier (Eqn. 1.4), and the effective variance is calculated from,

$$v_e = \frac{\int (r - r_e)^2 \pi r^2 n(r) dr}{r_e{}^2 \int \pi r^2 n(r) dr}. \tag{2.32}$$

The weighting by particle area during integration is included to account for the fact that a particle scatters light in approximate proportion to its cross-sectional area. Hansen (1971b) discusses the utility of $r_e$ and $v_e$ for describing the scattering properties of size distributions. An observed size distribution will have very similar extinction properties to those of another measured or analytic size distribution if their values of $r_e$ and $v_e$ are the same.

The droplet size distributions were normalized during the Mie scattering calculations to a liquid water content of 0.3 g $m^{-3}$. This normalization has no effect on the resultant radiative transfer model relationships we will use to develop the predictor scheme for effective radius. Substituting another cloud liquid water content did not alter the relationships between scaled optical depth and droplet size for homogeneous clouds. However, the values of local liquid water content are a controlling factor for accurate representation of vertically inhomogeneous cloud. We will discuss this subject in Chapter 3.

The scaled optical depth is defined similarly to that used by Curran and Wu (1982), that is,

$$\delta_\lambda{}' = (1 - g_\lambda)\delta_\lambda \tag{2.33}$$

where the wavelength, $\lambda$, is chosen as 0.85 $\mu$m in order to utilize the direct relationship between spectral reflectance at 0.85 $\mu$m and $\delta'_{0.85}$ demonstrated in Figure 2.5.

In this figure, the relationship of spectral reflectance ot scaled optical depth is independent of the droplet size distribution for a large range of values for that optical depth.

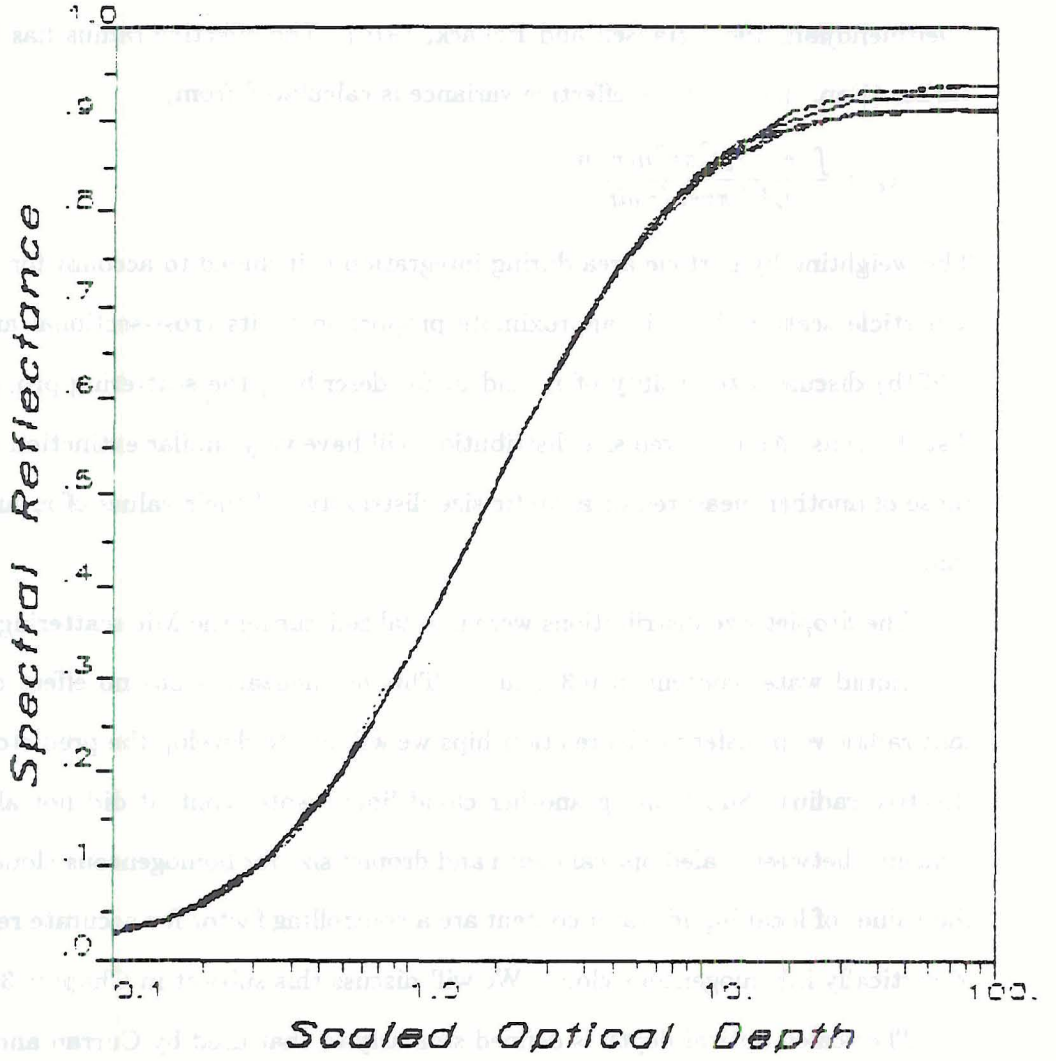


**Figure 2.5: Cloud-top reflectance at nadir as a function of scaled optical depth at 0.85 $\mu$m wavelength for four different droplet size distributions, with values of effective radius ranging from 5 to 30 $\mu$m.**

The independence of distribution type from 0.85-$\mu$m reflectance at a given value of $\delta'_{0.85}$ allows us to estimate scaled optical depth from cloud upward radiance measurements (assuming an accurate estimate or measurement of downwelling spectral flux at 0.85 $\mu$m). The 0.85 $\mu$m wavelength exhibits very little absorption by water. In contrast, the droplet absorption at 1.6 $\mu$m shows significant dependence on droplet size characteristics. Figure 2.6 shows the trends in 1.6-$\mu$m reflectance as droplet size increases. Note that the reflectance is plotted against the scaled optical depth at the 0.85-$\mu$m wavelength rather than the 1.6-$\mu$m wavelength, since we will use cloud reflectance data at 0.85 $\mu$m to estimate that scaled optical depth.

The cloud layer reflectances at 1.6 $\mu$m reach asymptotic values as the scaled optical depth exceeds approximately five. Since typical values of the asymmetry factor at 0.85 $\mu$m are 0.85, this corresponds to a cloud optical depth of 33. The physical depth of such cloud layers ranges from 193 meters for the droplet size distribution with effective radius three micrometers and effective variance 0.1, to 2137 meters for the size distribution with effective radius 30 micrometers and effective variance 0.1, because of the strong variation in the volume extinction parameter with $r_e$ at a normalized liquid water content of 0.3 g $m^{-3}$. However, the goal is not to estimate cloud depth or liquid water content, but droplet size. The separation of cloud reflectance by effective radius characteristics increases as the optical depth and scaled optical depths increase up to the asymptotic reflectance values. Also note in Figure 2.6 that for scaled optical depths less than approximately unity, the separation of reflectance values is less than 2%. For this reason, we expect that measurements of shallow clouds cannot be characterized by droplet size. The optical depth of this limit is equal to approximately seven, and this would correspond to cloud physical depths ranging from 40 to 434 meters for the gamma droplet size distributions with effective radius ranging from 3 to 30 $\mu$m, respectively. Because most stratus layers have size distributions with effective radius in the range 5–10 $\mu$m, cloud layers less than approximately 100 m depth would be expected to demonstrate only very weak changes in the magnitude of reflectance as size distribution is altered (for a given optical depth).

The effective variance of the modified gamma size distribution also has an impact on reflectance at 1.6 $\mu$m. Figure 2.7 demonstrates results for cloud layers differing values

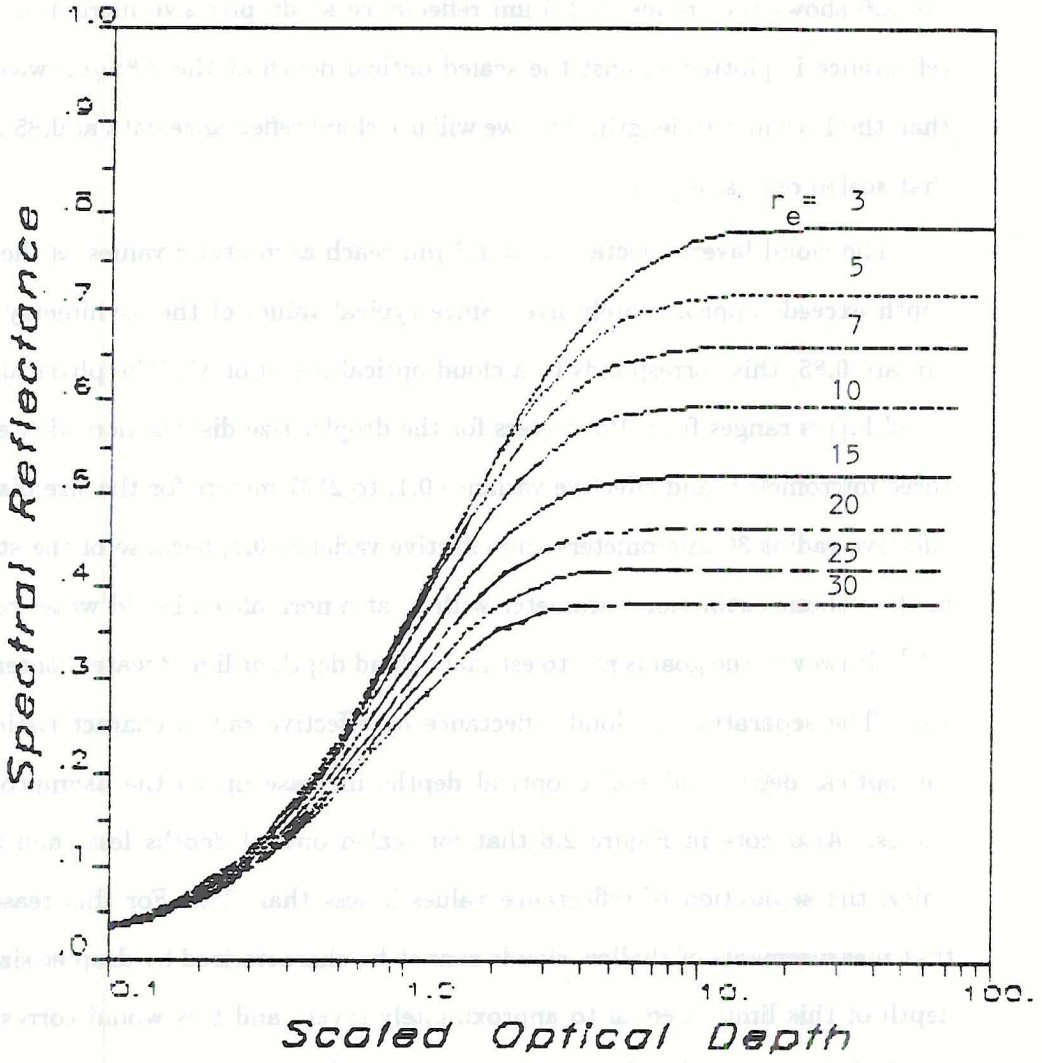


**Figure 2.6: Cloud-top reflectance at nadir for the wavelength 1.6 $\mu$m as a function of scaled optical depth at 0.85 $\mu$m for various droplet size distributions.**

of effective variance, 0.3 versus 0.1, which were chosen to represent the range of the majority of droplet size distributions for stratiform water cloud. The broader droplet size distribution clouds are slightly brighter (reflectance up to 2% larger), which allows a difference in the retrieved effective radius of 2–3 $\mu$m. Thus, averaging of the reflectance results for $v_e = 0.1$ and 0.3 provides values for a given $r_e$ distribution within 1–2 $\mu$m of the value for either of the two conditions of effective variance. The bias is toward smaller droplet size estimates for a broad size distribution, and toward size overestimates for a narrow size distribution.

Model simulations of published and measured size distributions were also performed for comparison with the simulations using the analytic size distributions. These simulations employed the size distributions summarized in Table 2.2. The size distributions are described by their mean radius ($r_m$), effective radius ($r_e$), liquid water content (W) and number concentration (N). The incorporation of aerosol-sized particles in the Stratocumulus (Sc) 2 and 3 distributions obtained from aircraft sampling (Wetzel and Vonder Haar, 1986a) is indicated by their small values of $r_m$ and enhanced particle counts, while the other (Derr, 1984) distributions do not include the aerosol. The results of cloud reflectance modeling show the same relationship between scaled optical depth and near-infrared reflectance as was observed in the simulations on analytic size distributions. We see in Figure 2.8 that the 1.6-$\mu$m reflectance increases with scaled optical depth up to an asymptotic value of reflectance, and that the magnitude of the asymptote is inversely related to the effective radius of the size distribution.

The relationships between scaled optical depth and spectral reflectance are closely reproduced at other solar and viewing angles. Some variation in the absolute magnitudes of the reflectances is noted. Figure 2.9 displays the fluctuation in reflectances for a changing viewing angle. In this example, the solar zenith angle is 50° and the optical depth at 0.85 $\mu$m is 16. The sensor can be moved a few degrees in view orientation from nadir without greatly altering model reflectance.The simultaneous measurement of reflectances at 0.85-$\mu$m and 1.6-$\mu$m is necessary, however, to ensure that effects due to small perturbations in the viewing angle are minimized.

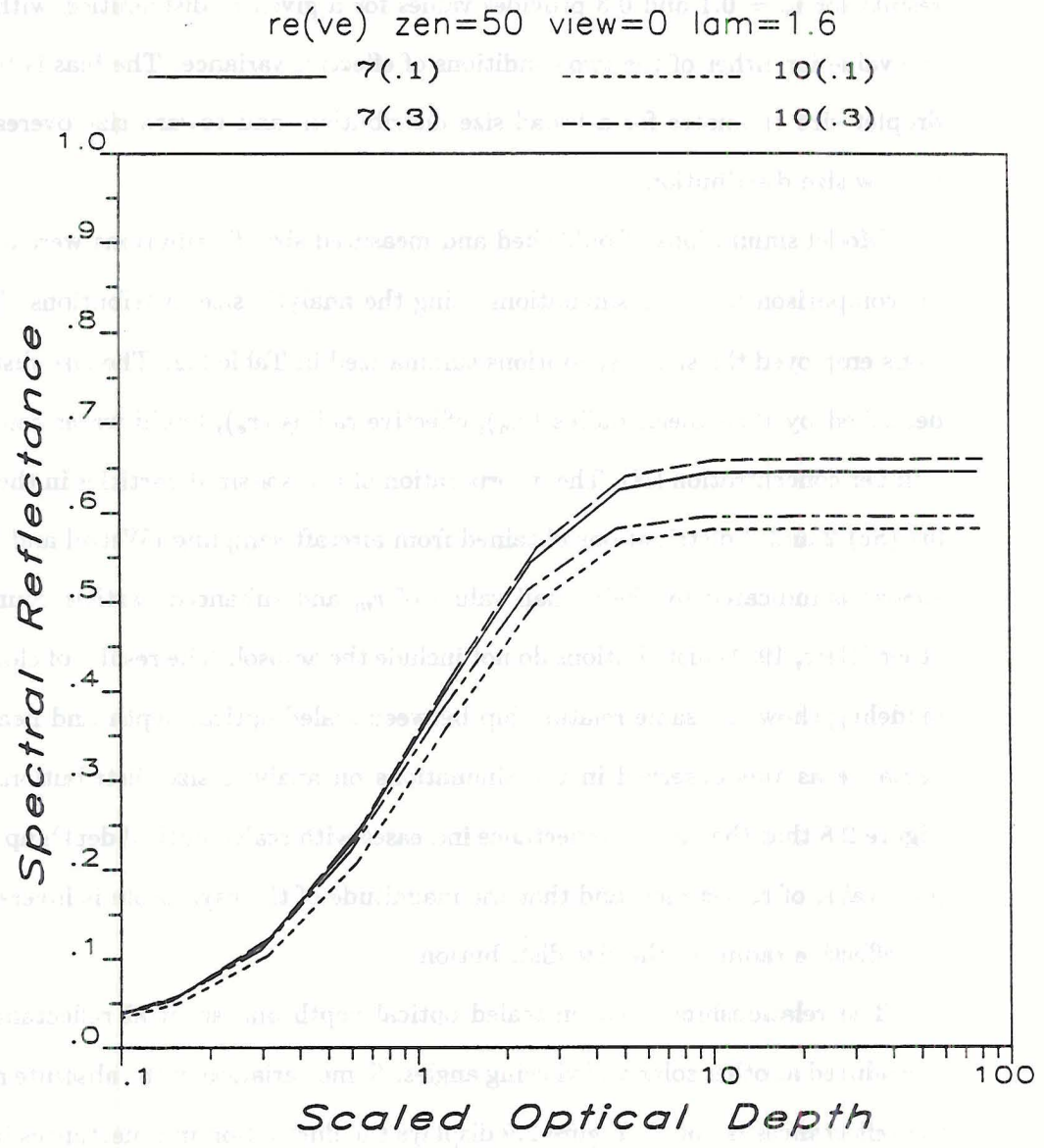


**Figure 2.7: Cloud-top reflectance at nadir for the wavelength 1.6 $\mu$m as a function of scaled optical depth at 0.85 $\mu$m for two pairs of gamma droplet size distributions with differing values of effective variance.**

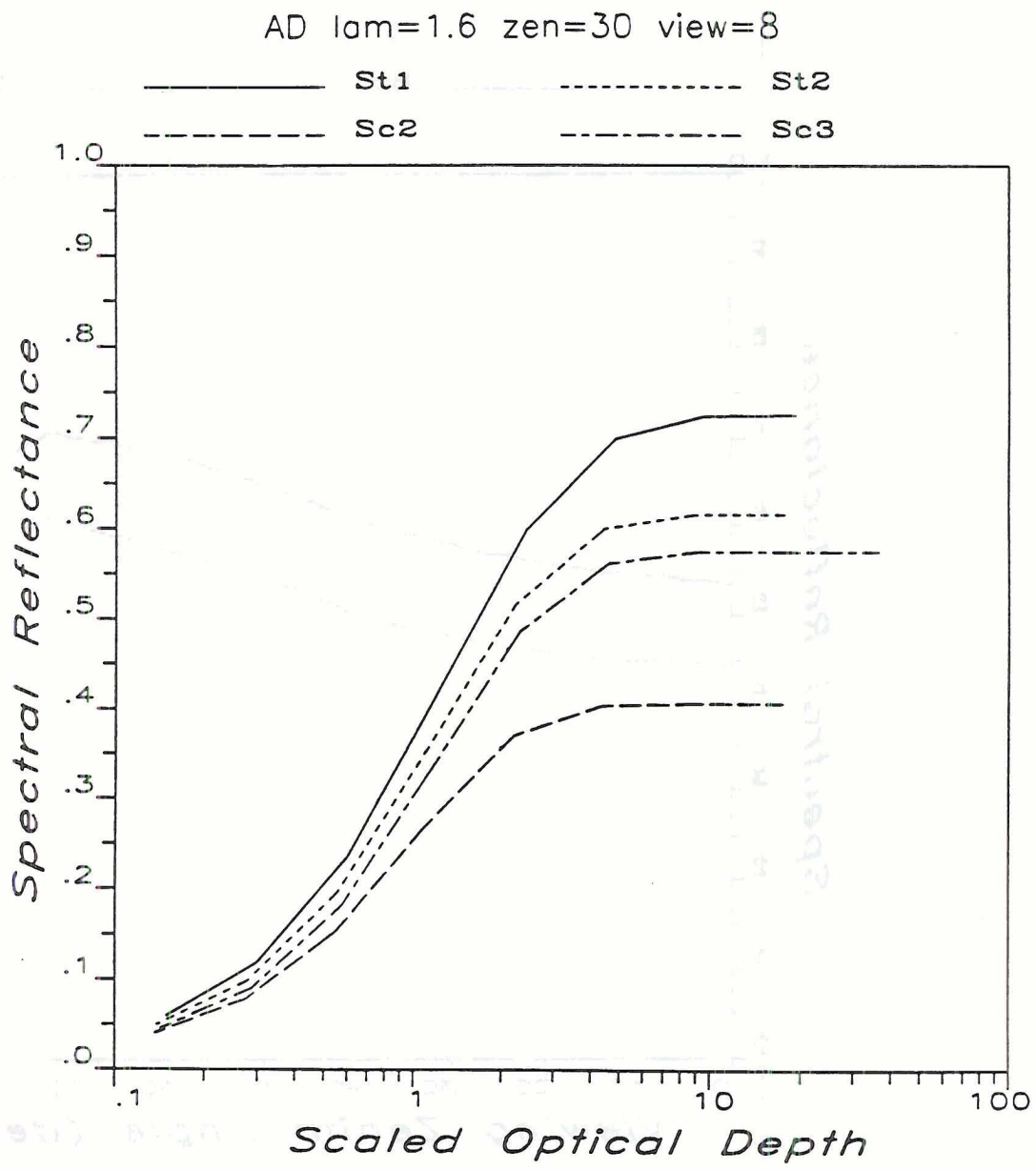


Figure 2.8: Cloud nadir reflectance at 1.6 $\mu$m as a function of scaled optical depth for a group of published and measured size distributions.

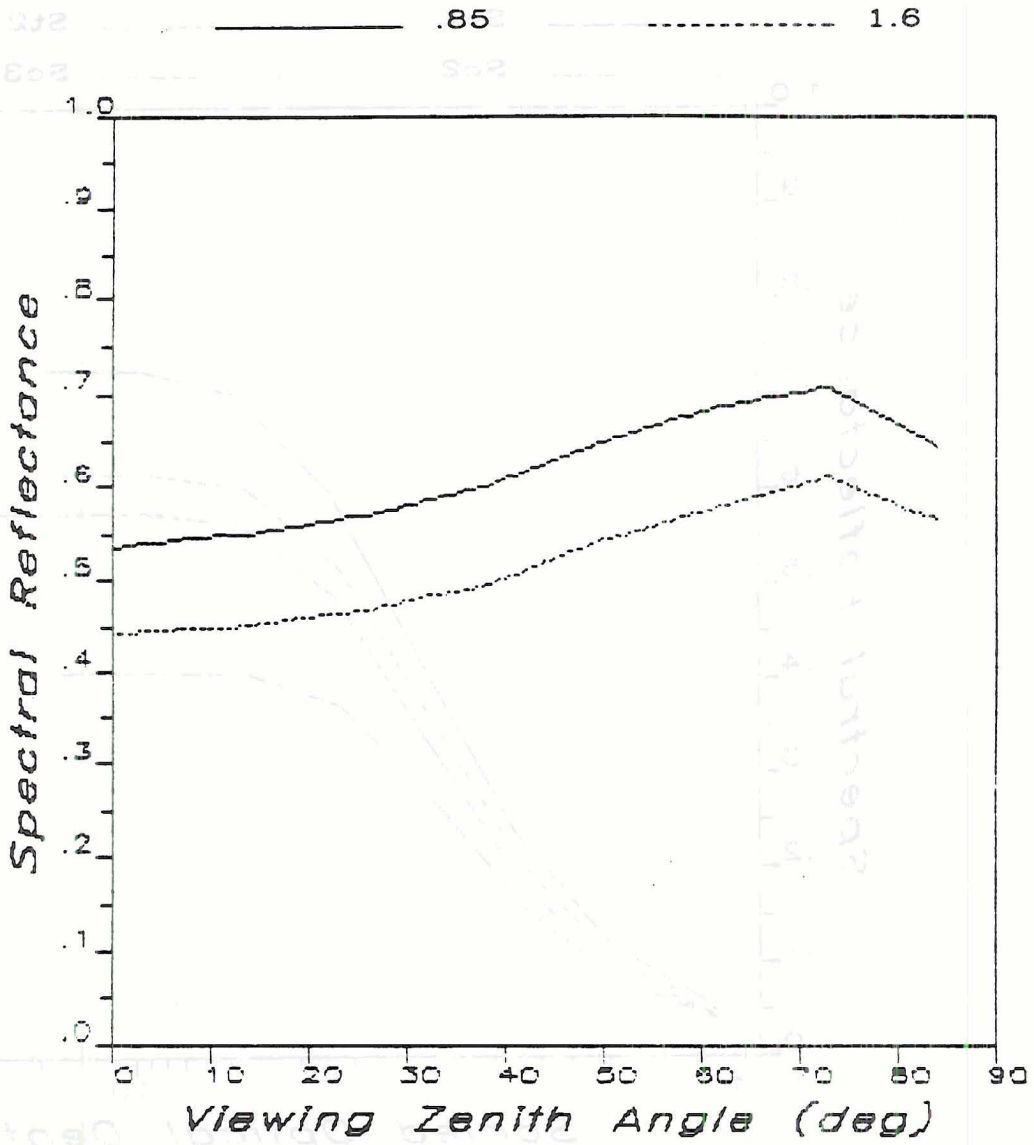


Figure 2.9: Cloud reflectance at 0.85 $\mu$m and 1.6 $\mu$m for various viewing angles.

Table 2.2: Characteristics of published and measured size distributions used in model simulations of stratiform clouds.

| *Label* | $r_m$ ($\mu m$) | $r_e$ ($\mu m$) | W ($g\ m^{-3}$) | N ($m^{-3}$) |
|---|---|---|---|---|
| Stratocumulus 1 | 3.93 | 5.57 | 0.16 | 371 |
| Stratus 1 | 4.22 | 6.57 | 0.28 | 458 |
| Nimbostratus | 6.75 | 10.86 | 0.90 | 326 |
| Stratus 2 | 6.55 | 11.13 | 0.70 | 260 |
| Stratocumulus 3 | 0.66 | 13.49 | 0.09 | 581 |
| Stratocumulus 2 | 0.68 | 37.79 | 0.36 | 547 |

## 2.7 Retrieval method for effective radius

The results described in the previous section were applied to an objective retrieval method based on co-located measurements of cloud reflectance at the 0.85- and 1.6-$\mu$m wavelengths, and using interpolation from families of curves from model simulations for a given viewing geometry. A scheme for cubic spline interpolation (Press *et al.*, 1986) was used to determine the scaled optical depth from model results of 0.85-$\mu$m reflectance values, for a specified solar zenith angle and sensor viewing angle. Spline interpolation was then applied a second time against the 1.6-$\mu$m reflectance curves versus scaled optical depth for a family of gamma size distributions with increasing values of effective radius and a constant value of effective variance. The two values of effective variance, 0.1 and 0.3 provide a range within which to estimate the effective radius. Assuming that the effective variance is also an unknown but within this observed range, the effective radius was obtained by averaging the values obtained for $v_e = 0.1$ and $v_e = 0.3$.

In order to assess the potential accuracy of the retrieval scheme, droplet size was estimated from model results for the 1.6-$\mu$m cloud reflectance at a wide range of optical depths. The adding model was applied to the Derr droplet size distributions and the gamma distributions. The resulting effective radius estimates were within the accepted uncertainty of 3 $\mu$m, as shown in Figure 2.10, for those cases where layer optical depth was not less than 4 (at the 0.85 $\mu$m wavelength). At lower values of optical depth, the behavior

of the relationship between layer reflectances at 0.85 and 1.6 $\mu$m becomes irregular, because the relationship between scaled optical depth and reflectance at 0.85 $\mu$m is not independent of droplet size at very small optical depths. This is likely a consequence of the reduction in multiple scattering, such that the weighting of the scaled optical depth with the asymmetry parameter does not accurately represent the transmission and reflection of the cloud layer. Thus, cloud optical depths equal to or greater than 4 are needed for implementation of the retrieval procedure. The retrieval accuracy is best for large optical depth, and the droplet size estimates reach an asymptotic value at an optical depth of 64.

Sensitivity tests were carried out to determine the measurement accuracy required for the estimation scheme. The retrieval method is sensitive to the magnitude of the spectral reflectance values. For example, if we alter the absolute magnitude of the 1.6-$\mu$m reflectance of the Stratus 2 cloud layers by 0.01, the resulting droplet size estimate varies by 1 to 2 $\mu$m. Therefore, the error or uncertainty in the magnitude of cloud reflectance derived from the measurement system should not exceed 0.03. This is possible for aircraft systems in which upward and downward radiance are measured together near cloud top, but may be difficult to achieve from satellites, or for that matter, from aircraft flying above an intervening aerosol layer. Potential extinction of the downward irradiance and upward radiance due to accentuated water vapor absorption in the cloudy layers should also be estimated for inclusion in the reflectance calculation, to limit this source of error.

Simulations of reflectance at varied solar zenith angle were utilized within the retrieval scheme to investigate the sensitivity to accurate location of the observation point relative to solar position. Figure 2.11 shows the effect of solar angle, which demonstrates that a small uncertainty or temporal change (5 degrees) in solar position during sampling alters the reflectance less than a 3 $\mu$m change in effective radius would, for effective radius in the range 3–20 $\mu$m. Cloud layers with larger droplets would thus require solar zenith angle specification accuracy better than 5 degrees. These results can be used to determine the pixel area over which droplet size retrievals for a constant value of solar zenith angle should be valid. It is evident that the retrieval procedure should utilize model solutions for solar zenith angle increments of one degree or better. Also, the results suggest that the spatial

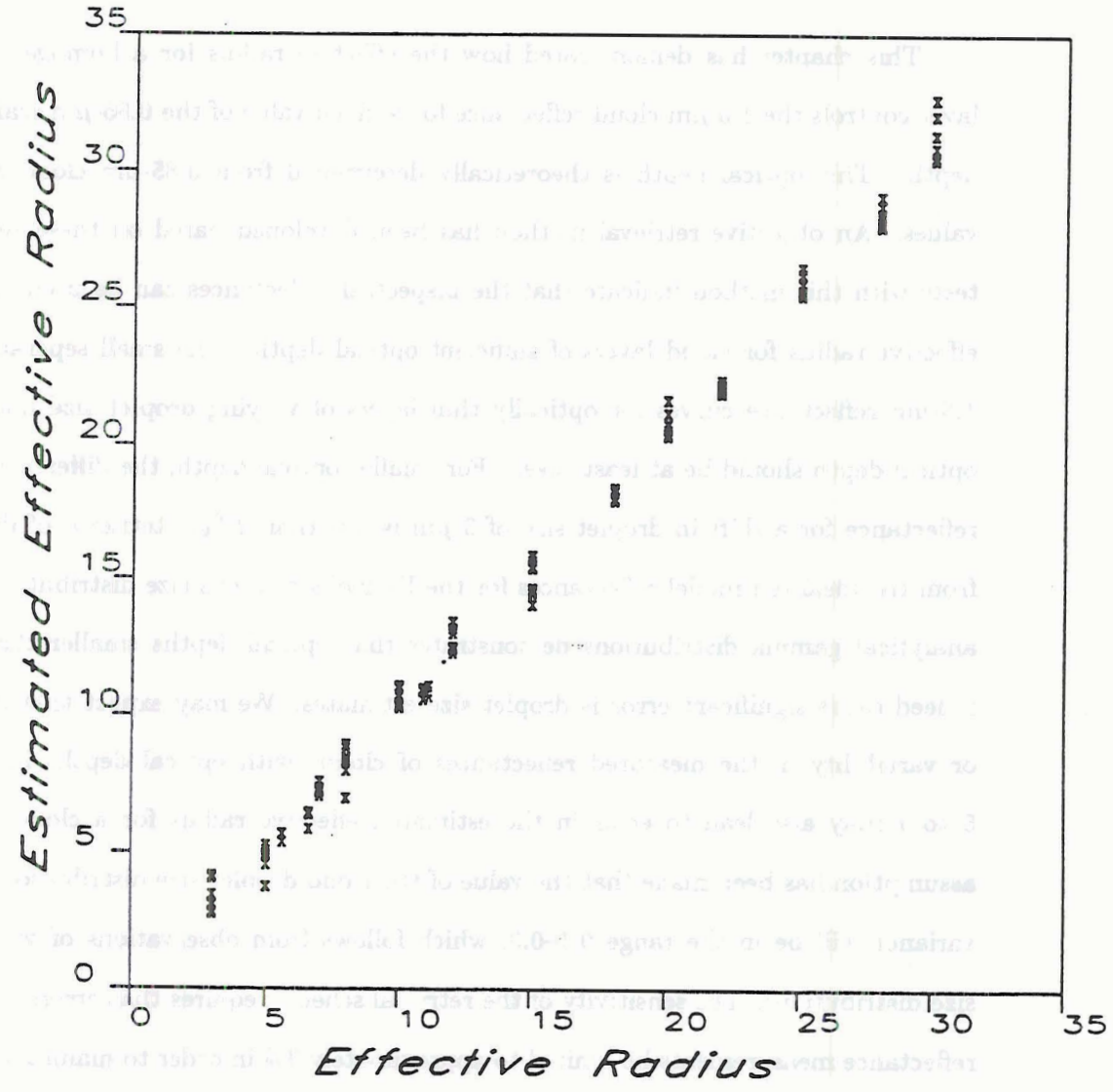


Figure 2.10: Comparison of effective radius values for selected droplet size distributions with those estimated from the retrieval scheme.

patterns seen by simple image combinations such as a ratio of 0.85 and 1.6 $\mu$m channels should be related to spatial varations in droplet size over regions up to approximately 200 km across.

## 2.8 Summary

This chapter has demonstrated how the effective radius for a homogeneous cloud layer controls the 1.6-$\mu$m cloud reflectance for a given value of the 0.85-$\mu$m scaled optical depth. This optical depth is theoretically determined from 0.85-$\mu$m cloud reflectance values. An objective retrieval method has been developed based on these results, and tests with this method indicate that the bispectral reflectances can be used to estimate effective radius for cloud layers of sufficient optical depth. The small seperation of the 1.6-$\mu$m reflectance curves for optically thin layers of varying droplet size indicate that optical depth should be at least seven. For smaller optical depth, the difference in model reflectance for a shift in droplet size of 3 $\mu$m is less than 2 %. Retrieval of droplet size from the idealized model reflectances for the Derr observations size distributions and the analytical gamma distributions demonstrates that optical depths smaller than four do indeed cause significant error is droplet size estimates. We may expect that small error or variability in the measured reflectances of clouds with optical depths in the range 5 to 7 may also lead to error in the estimated effective radius for a cloud layer. An assumption has been made that the value of the cloud droplet size distribution's effective variance will be in the range 0.1–0.3, which follows from observations of various cloud size distributions. The sensitivity of the retrieval scheme requires that errors in the cloud reflectance measurements be limited to approximately 3% in order to maintain a retrieval accuracy of 3 $\mu$m for the effective radius. The retrieval accuracy improves as cloud optical depth increases, but reaches asymptotic values at the moderate optical depth of 64. The effects of cloud inhomogeneity on droplet size estimates are explored in the following chapter.

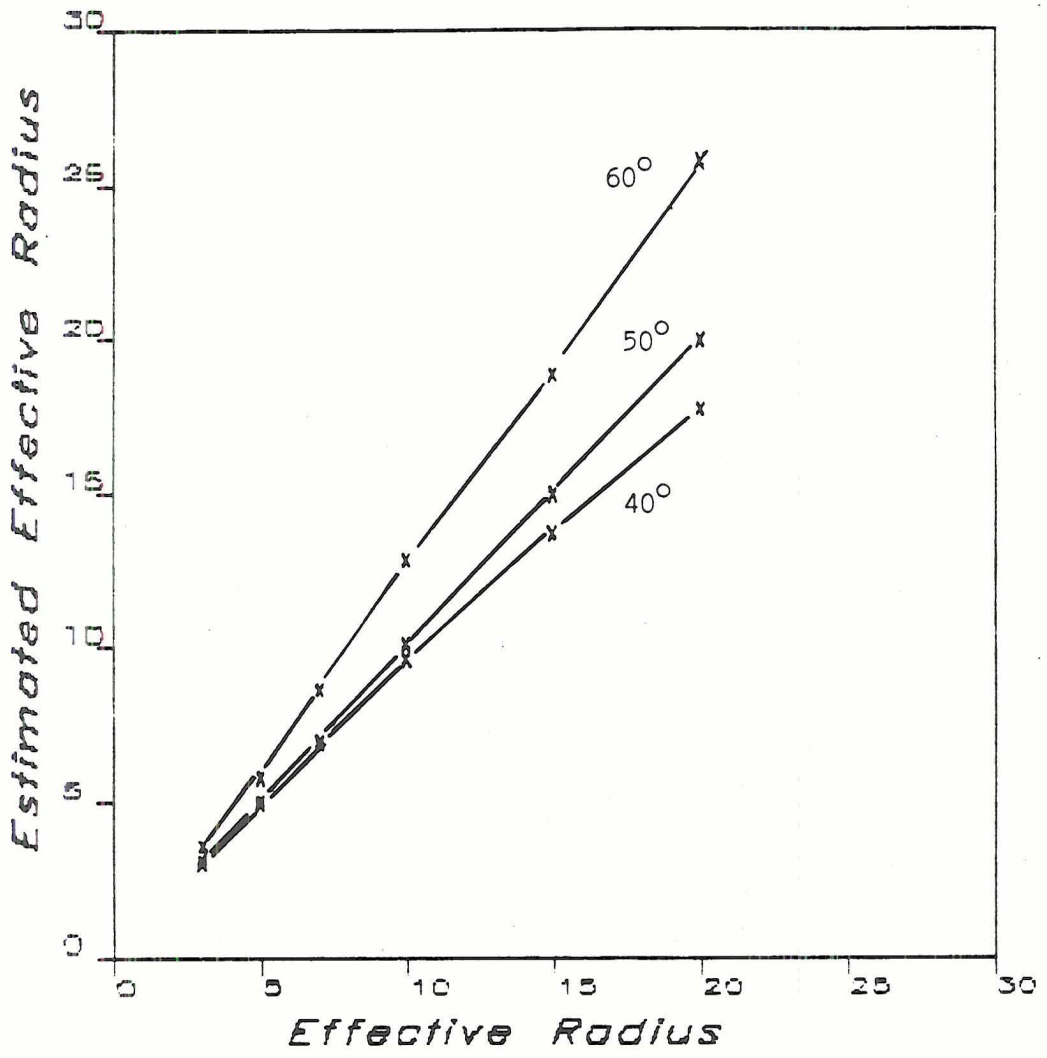


Figure 2.11: Effective radius estimated from model results with solar zenith angle varied from 40 to 60 degrees. The "true" effective radius is for solar zenith angle of 50 degrees.

Estimated Effective Radius
Effective Radius

# Chapter 3

# CLOUD STRUCTURE INFLUENCES ON REFLECTANCE

## 3.1 Introduction

This chapter contains a description of the models used to simulate vertical and horizontal inhomogeneity of stratiform cloud, and the results obtained from those simulations. The radiative transfer Adding model for plane-parallel multiple scattering layers was utilized to examine the influence of cloud vertical structure variability on the spectral reflectance in the two near-infrared window bands. Droplet size distributions within the model clouds were varied, and aerosol was included both within the clouds and in isolated layers above cloud top. The influence of refractive index was investigated for the droplet population as a whole, and for the aerosol population alone. A Monte Carlo radiative transfer model was also utilized, to simulate spectral reflectance from horizontally inhomogenous cloud. Analysis of the model results provided quantitative information on the potential errors in retrieved droplet size due to cloud structure. The types of cloud structures modeled were generally limited to those sampled during our field experiments, in order to focus on the interpretation of measurements and droplet size estimates in observed conditions.

## 3.2 Reflectance of multilayer clouds

The Adding method was used to simulate the radiances reflected from clouds consisting of multiple, adjoining plane parallel layers of differing droplet size characteristics. The resulting nadir reflectances were applied to the retrieval method described in Chapter 2 to estimate first the scaled optical depth at 0.85 $\mu$m wavelength and then the effective radius. The Derr and gamma size distributions were utilized. We will discuss the results for three

cloud simulations, each of which is a two-layer cloud, with solar zenith angle equal to 50°. As the droplet size in stratus typically increases with height, size distributions with larger values of effective radius were situated in the upper layers. The physical depths of the top and bottom cloud layers were varied to measure the effect on droplet size estimates of transmission from lower layers. We will assume that the goal of the remote sensing technique is to identify the droplet size in the upper region of the cloud. The first model cloud is composed of the Derr Stratus 2 ($r_e$ = 11.1 $\mu$m) distribution at cloud top and Stratus 1 ($r_e$ = 6.6 $\mu$m) at cloud base. The second simulation contains the gamma distribution of effective radius 15 $\mu$m at cloud top and that of effective radius 5 $\mu$m at cloud base. The effective variance for this pair is 0.3 in both instances. The last cloud simulation we will discuss is composed of the gamma size distributions with effective radius of 7 $\mu$m at cloud top and 3 $\mu$m at cloud base. The two gamma distributions in this case have an effective variance equal to 0.1. The characteristics and results of the layered cloud simulations are summarized in Table 3.1.

Table 3.1: Characteristics of layered cloud simulations.

| DSD (top) | DSD (base) | $\triangle$z (top) (m) | $\triangle$z (base) (m) | $\rho_{0.85}$ (%) | $\delta^{est}_{0.85}$ (n.d.) | $\rho_{1.6}$ (%) | $r_e^{est}$ ($\mu$m) |
|---|---|---|---|---|---|---|---|
| Gam 7 | Gam 3 | 50 | 50 | 52.63 | 2.09 | 55.53 | 4.9 |
| Gam 7 | Gam 3 | 100 | 100 | 71.10 | 4.29 | 66.42 | 5.1 |
| Gam 7 | Gam 3 | 200 | 200 | 83.54 | 8.46 | 68.04 | 5.8 |
| Gam 7 | Gam 3 | 400 | 400 | 90.87 | 16.34 | 65.53 | 7.0 |
| St2 | St1 | 50 | 50 | 38.31 | 1.26 | 39.08 | 9.1 |
| St2 | St1 | 100 | 100 | 58.00 | 2.53 | 51.78 | 10.0 |
| St2 | St1 | 200 | 200 | 74.47 | 5.05 | 56.83 | 10.7 |
| St2 | St1 | 400 | 400 | 85.66 | 9.99 | 57.08 | 11.1 |
| Gam 15 | Gam 5 | 50 | 50 | 32.26 | 1.01 | 34.25 | 8.8 |
| Gam 15 | Gam 5 | 100 | 100 | 52.40 | 2.07 | 50.30 | 8.1 |
| Gam 15 | Gam 5 | 200 | 200 | 71.17 | 4.30 | 58.47 | 9.1 |
| Gam 15 | Gam 5 | 400 | 400 | 83.77 | 8.57 | 56.63 | 11.3 |
| Gam 15 | Gam 5 | 800 | 800 | 91.21 | 16.68 | 52.96 | 13.8 |
| Gam 15 | Gam 5 | 400 | 200 | 75.14 | 5.25 | 55.02 | 12.0 |
| Gam 15 | Gam 5 | 400 | 100 | 66.26 | 3.53 | 51.95 | 12.9 |

The relative effects of the cloud base and top layers can be seen by plotting the effective radius estimated for the clouds against the true values of effective radius in the cloud top layer (Figure 3.1). The smaller droplet sizes in the lower layers causes a brightening of cloud top, and this increased reflectance causes the estimated effective radius to be less than the cloud top value. The model results demonstrate the stronger influence of the layer characteristics at cloud top.

The retrieved value of droplet size is weighted by both the upper and lower cloud layers under conditions of typical optical depths. In the first two types of model simulations shown in Table 3.1, the cloud top droplet size is retrieved within an accuracy of 2.1 $\mu$m or better for each of the cloud depth variations. Under the limitation that the cloud base layer is not deeper than the cloud top layer, the effective radius was correctly estimated. The accuracy of the estimates improved as the cloud top depth increased. A change in the liquid water content of a given cloud sub-layer would alter the cloud layer physical depths. Increasing the liquid water content (from the value of 0.3 g $m^{-3}$ used here) would decrease the cloud layer depths necessary to produce accurate estimates of the cloud top droplet size. In stratus, where liquid water content is observed to increase with height, the droplet size retrieval will be even more weighted toward the upper cloud layer conditions.

The third type of model represented a stronger difference in droplet size between cloud base and cloud top (5 versus 15 $\mu$m). In these cases, the increased cloud brightness due to reflection from the lower cloud layer strongly biases the retrieved droplet size. The results from this model show correct droplet size estimates in the cases where the cloud top layer is deep (more than approximately 500 meters) or deep relative to the lower layer. The last two cases for this model represent a 400 m cloud top layer, and shallower (200 and 100 m) cloud base layers which are equivalent to a reduction in liquid water contents to 0.15 and 0.075 g $m^{-3}$, respectively, for a 400 m cloud base layer. Droplet size retrievals for these cases are within 3 $\mu$m of the cloud top value. The effect of small droplet size at cloud base is minimized by the attendant low liquid water contents. We therefore expect acceptable droplet size estimates from stratus clouds with typical vertical variations in droplet size and liquid water contents.

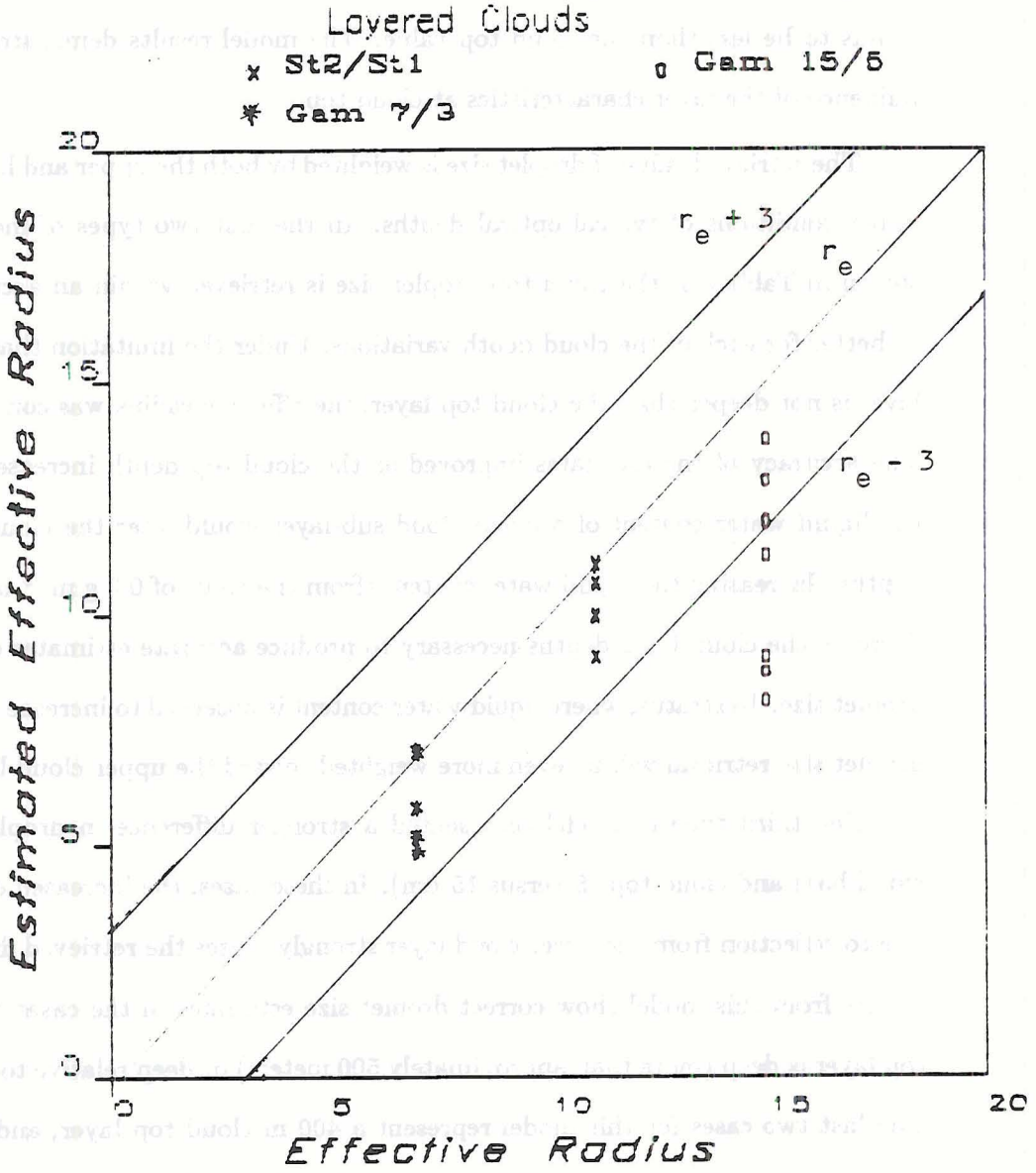


Figure 3.1: Retrieved values of droplet effective radius for vertically nonhomogeneous cloud simulations.

### 3.3 Incorporation of aerosol populations

Refractive index variations designed to represent the aerosol populations were included in a set of the Adding model runs. First, aerosol refractive indices were used to simulate an aerosol layer overlying a cloud droplet layer. For these cases, the aerosol size distribution was obtained by clear-air sampling a short distance above a stratus cloud top on day 177 during the California sampling program (see Chapter 4 and the Appendix for a description of the data collection program). Refractive indices were taken from Hänel (1976) to represent an absorbing urban aerosol layer at low ambient relative humidity. The F7 population is assumed to include carbon-based constituents, and is assigned $n_{r,0.85} = 1.53$, $n_{i,0.85} = 0.06$, and for the longer wavelength $n_{r,1.6} = 1.50$ and $n_{i,1.6} = 0.12$. F3 represents the cloud-top droplet size distribution, assumed to be pure water.

The influence of the F7 layer is to reduce the cloud brightness. The aerosol optical depth is 0.02, while the cloud optical depth is varied from 2 to 128 and the solar zenith angle is 50°. As can be seen in Figure 3.2, the presence of aerosol above the cloud increases the estimate of effective radius, but this increase is less than 1 $\mu$m. The F3 stratus droplet size distribution has an effective radius equal to 5.9 $\mu$m, while the maximum value of retrieved effective radius is 6.6 $\mu$m, occurring when cloud optical depth is at the minimum value 2.0.

A second source of data on aerosol refractive indices was Shettle and Fenn (1979). These were used to simulate a marine haze layer. Aircraft sampling in the marine boundary layer produced size distributions of haze aerosol. One of these has been selected for use in the simulation of marine haze beneath the F3 stratus cloud. It is designated as F12, and was assigned the refractive indices for the Shettle and Fenn oceanic aerosol at 70% relative humidity. The oceanic haze is assumed to account for the majority of aerosol in the marine boundary layer. It displays a relatively strong spectral variation in the values of the imaginary refractive index ($n_i$), such that absorption for a population of this aerosol is similar to that of water at 0.85 $\mu$m, but at 1.6 $\mu$m the absorption is larger than for water.

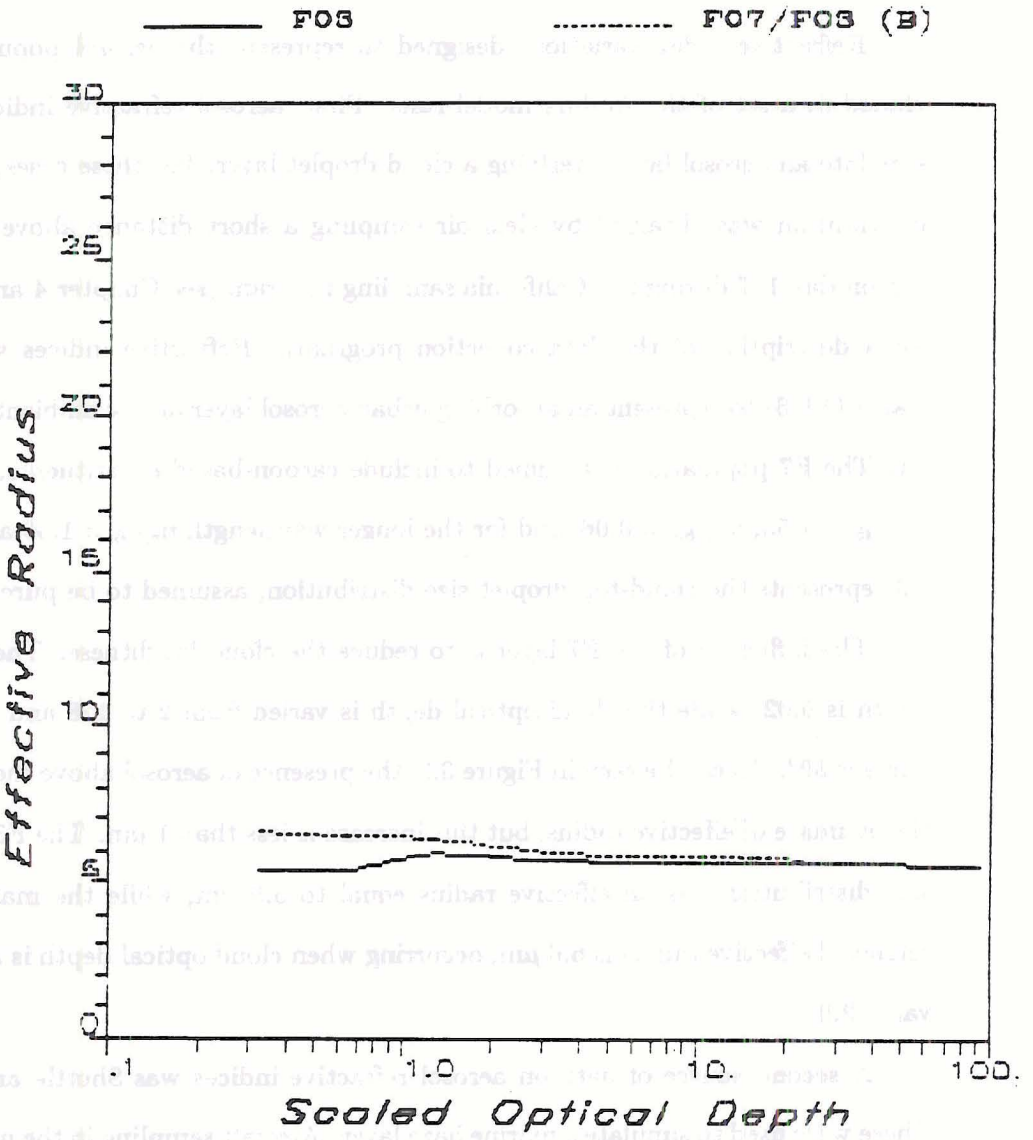


**Figure 3.2: Effective radius estimates for stratus and for aerosol above stratus.**

Figure 3.3 displays results of effective radius retrievals for stratus and for stratus with underlying haze. The haze depth is 500 m, and solar zenith angle is 50°. The lower haze brightens the cloud-haze ensemble at small values of cloud optical depth, but the resulting influence on estimated droplet size decreases rapidly as the scaled optical depth of the cloud increases. The error in effective radius is less than 1 $\mu$m for scaled optical depths greater than 1. This corresponds to a 0.85-$\mu$m optical depth of approximately seven, shown in Chapter 2 to be a value above which we can expect to measure differences in 1.6-$\mu$m reflectance due to signficant changes in droplet effective radius. Thus, the effects of haze on droplet size retrieval are small for the layers which would be otherwise deemed suitable for the retrieval procedure.

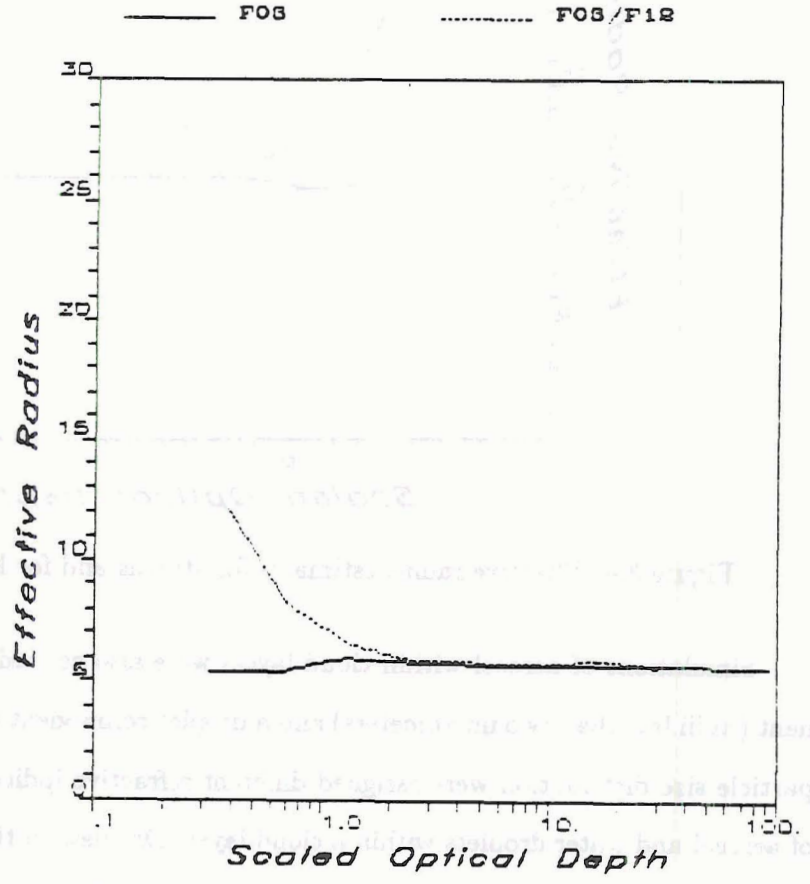


Figure 3.3: Effective radius estimates for stratus and for haze below stratus.

We see the same behavior for a simulation of marine haze below the Derr Stratus 2 cloud type. The results for this model are shown in Figure 3.4. In this case, the effective radius of the cloud itself is 11.1 $\mu$m. For very small cloud optical depths, the retrieved

effective radius is more than 10 $\mu$m too large, but this error is reduced to 2.5 $\mu$m as the scaled optical depth of the cloud-haze ensemble exceeds 1.0. Some bias toward larger droplet size is foreseeable in this case, for cloud optical depths near this limit (optical depths 7 to 10).

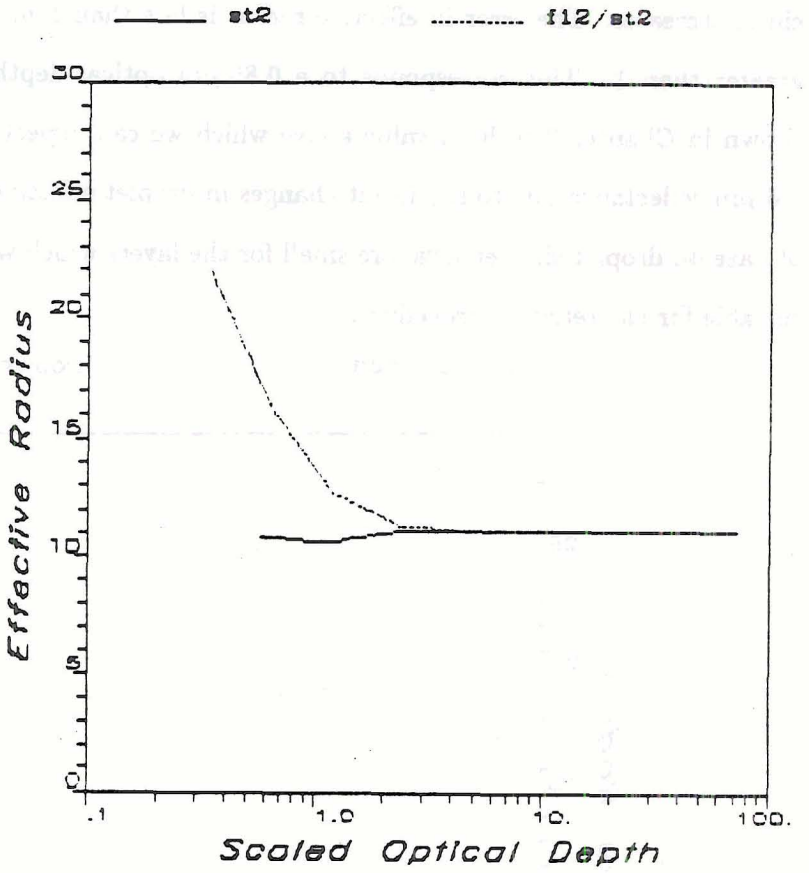


Figure 3.4: Effective radius estimates for stratus and for haze below stratus.

Simulations of aerosol within cloud layers were also carried out. An aerosol component (radii less than two micrometers) and a droplet component (all larger sizes) of the F3 particle size distribution were assigned different refractive indices to represent a mixture of aerosol and water droplets within a cloud layer. Droplets in the aerosol size range were given the refractive indices for oceanic haze under conditions of 99 % relative humidity (Shettle and Fenn, 1969). Larger droplets were assumed to be pure water. The negligible influence of the attendant haze is demonstrated by retrieving estimates of effective radius for a range of cloud optical depths. Results of such an experiment are given by Figure 3.5, in which is plotted the retrieved values of effective radius based on calculated

spectral reflectances at 0.85 and 1.6 $\mu$m wavelengths for pure water and the water-haze size distributions. Secondly, the presence of aerosol within the cloud droplets larger than 2 $\mu$m has little effect on the extinction properties, since typical concentrations of aerosol in these larger droplets is less than 0.1

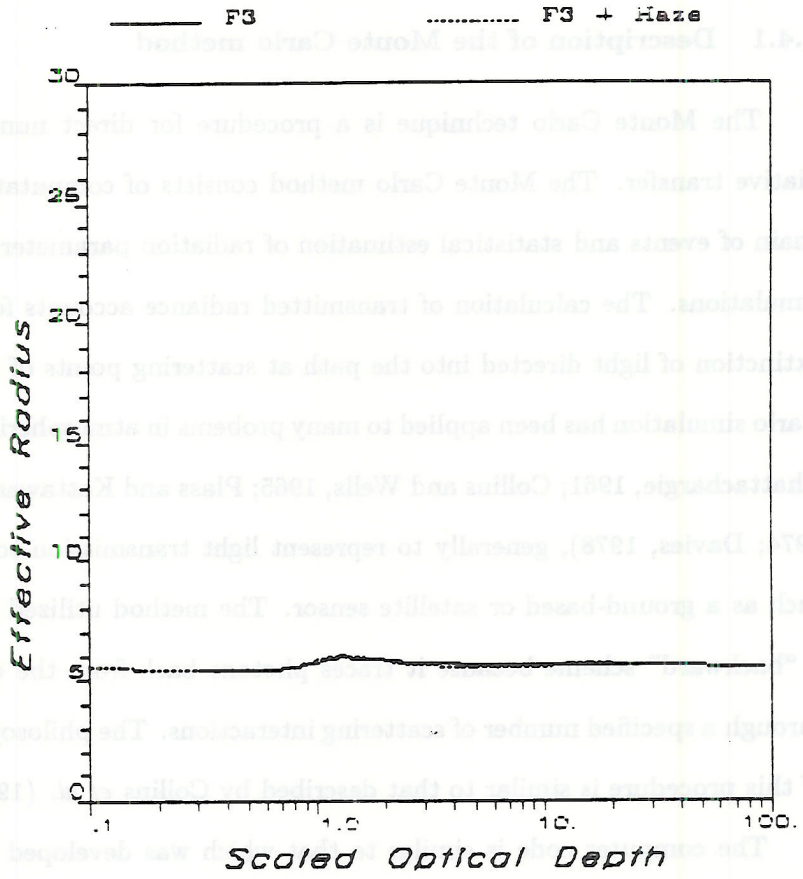


Figure 3.5: Effective radius estimates for a measured stratus particle size distribution and for the same stratus but containing oceanic haze in the aerosol size range.

Other studies of aerosol effects in cloud have assumed certain particle size distributions, under assigned values of liquid water content. We have utilized actual measurements of the relative numbers of particles in aerosol and droplet size ranges to provide a more realistic calculation of reflectance changes. The spectral dependence of refractive indices for aerosol-and-droplet mixtures is not fully known, and chemical sampling was not a part of our field measurement program. We have used previously documented refractive indices, and have shown that the reflectance of non-pure water clouds causes relatively small deviations in the droplet size retrieval. An exception in the case of optically thin

cloud (scaled optical depths less than approximately one), where sub-cloud haze can cause droplet size to be overestimated. In order to explore another possible control on spectral reflectance properties, the radiative modeling of broken cloud fields was pursued.

## 3.4 Simulation of cloud horizontal inhomogeneity

### 3.4.1 Description of the Monte Carlo method

The Monte Carlo technique is a procedure for direct numerical simulation of radiative transfer. The Monte Carlo method consists of computational simulations of the chain of events and statistical estimation of radiation parameters from the results of the simulations. The calculation of transmitted radiance accounts for successively increased extinction of light directed into the path at scattering points of increasing order. Monte Carlo simulation has been applied to many probems in atmospheric optics (Skumanich and Bhattachargie, 1961; Collins and Wells, 1965; Plass and Kattawar, 1968; McKee and Cox, 1974; Davies, 1978), generally to represent light transmission to or from a finite target such as a ground-based or satellite sensor. The method utilized for this study is termed a "backward" scheme because it traces photons back from the collecting point (sensor) through a specified number of scattering interactions. The philosophy and implementation of this procedure is similar to that described by Collins *et al.* (1972).

The computer code is similar to that which was developed by Davis *et al.* (1985), and has been recently documented by Tsay *et al.* (1987). The key steps involve the determination of the characteristics of each scattering event; that is, the distance between each successive scatter, the type of scatter and the angle of scattering. In each collision, radiance is redistributed, not only in angle but also in polarization. The radiance and polarization are described by the four components of the Stokes vector, which have dimensions of radiant intensity. The results discussed herein focus on the cloud radiance only, $L$.

The energy source for the model is a monodirectional, monochromatic, plane emitting one photon per unit area in the direction $\Omega_0$, so for a solar source this can be scaled by $cos(\Omega_0)$ to incorporate solar zenith angle dependence. The estimating function used to

determine the Stokes vector for the path segment of the $j^{th}$ photon after exactly $n$ scatters is given by

$$S_n{}^n = \prod_{i=1}^{n} W_i e^{-\delta_T} P(\Omega_{n-1}, \Omega) P(\Omega_{n-2}, \Omega_{n-1}) \cdots P(\Omega_1, \Omega_2) P(\Omega_0, \Omega_1) \prod_{i=2}^{n} c_i. \qquad (3.1)$$

The parameter $W_i$ is a weighting factor which is introduced to allow a portion of the photon energy to escape the model during each collision. When the photon intersects the ground, the weighting factor is equal to the surface albedo, so that the individual photon radiance scattered back from the ground has been reduced by the factor (1-albedo). When the photon direction of motion is toward the ground but it encounters a scatter above the ground surface, $W_i$ is set equal to $\frac{\sigma_S}{\sigma_T}$, where $\sigma_S$ is the local scattering coefficient (including both particle and molecular coefficients, if applicable), and $\sigma_T$ is the local extinction coefficent. If, on the other hand, the photon is directed toward space prior to the collision, the reducing factor for radiance resulting from that event is

$$W_i = \frac{\sigma_S}{\sigma_T}[1 - e^{-\delta_a}], \qquad (3.2)$$

where $\delta_a$ is the total atmospheric optical depth along the photon direction vector.

The second term on the RHS of Equation 3.1 reduces the incoming source radiation by a factor equal to the optical depth between the top of the model atmosphere and the scatter point. It is obtained by determining the direction vector along this path and summing the extinction for each individual model grid space through which the vector passes according to the length of the path segment within that grid space.

The product of phase matrices $P$ given in Equation 3.1 traces the sequence of scattering events which the photon has experienced in its prior history, and therefore is generally a combination of matrices corresponding to particle, Rayleigh, and ground reflection. These matrices represent the process of multiple scatter from the "initial" scatter between the sun and $n^{th}$ scatter point, back along the photon path and into the sensor. The Monte Carlo model as it is used here computes the polarization matrix for the current scattering into the photon path from information on the old and new direction vectors and the local scattering phase matrix.

The last term on the RHS of Equation 3.1 provides a normalization coefficient, $c$, for each phase matrix. This normalization is used to correct for bias introduced by random sampling of scattering angles from a density function defined by the local phase function. In other words, the scattering angles are chosen from the region of the phase function where scattering is most likely, but the magnitude of the phase function at that point is subsequently normalized to remove its larger magnitude at those angles.

The Stokes vector for the entire ensemble of $j$ photons throughout their complete histories of $n$ scattering events is calculated from

$$S(\overline{L},\overline{Q},\overline{U},\overline{V}) = \frac{1}{j}\Sigma_j\Sigma_n S_{j,n}(L,Q,U,V)\,. \tag{3.3}$$

A probabilistic factor is used in making each of the scattering angle and other "random" determinations. The process is not entirely random, since the random number factor is found through a pseudo-random computational procedure and is then weighted according to the physical characteristics of the attenuating medium. As noted by Plass and Kattawar (1968), the standard deviations of the model results for relative radiance are (roughly) inversely proportional to the square root of the computing times! Accuracy can be assessed by comparing the mean values of the model radiances when different random number series are employed, and by evaluating the similarity of the results to those of different numerical methods.

The percent error within 99% probability limits is defined as

$$E_{99} = \frac{3\sigma_L}{\overline{L}\sqrt{j}}100\,. \tag{3.4}$$

The error level generally decreases very slowly because of the the large values of the standard deviation of the radiance induced by using pseudo-random selection of scattering angles and other factors. Validity of the error estimate was verified by running the model under identical conditions with a varied random seed number. The radiance results for these tests were within the percent error limit defined by the equation above.

### 3.4.2 Methodology

The backward Monte Carlo simulation proceeds as described in the following paragraphs. First, several parameters are initialized, including the number of photons and photon scatters, a random number seed value, the monochromatic model wavelength, surface albedo, solar elevation and azimuth angles, and observer elevation and azimuth angles. Input data files are used to establish cloud geometry and internal structure, and also to specify the cloud droplet distribution Mie phase function. A cumulative probability table is then generated for the density function of scattering angles. A multi-segment path and resulting Stokes vector for each photon are the primary output of the model. A seed value ($s$) pre-determines the sequence of values that will function as random numbers in the calculations. The first step calling for a random number is specification of the optical depth of a photon path segment between scattering points. This optical depth is given by

$$\delta_s = -log^{-1}(1 - (W_\delta RN) \tag{3.5}$$

where the weighting applied to the random number is determined from

$$W_\delta = 1 - e^{-\delta_p}. \tag{3.6}$$

The parameter $\delta_p$ is the sum of optical depths encountered in grid spaces along the projection of the current photon direction vector until it leaves the model boundaries. If the vector leaves the model at a solid boundary, it is assumed that $e^{-\delta_p} = 0$.

The initial direction vector is defined by the observer viewing azimuth and elevation angles. The sum of optical depth along any direction vector is determined from the starting position of the vector and the intersection of the vector with the model grid volumes of specified extinction values. The distance along the vector at which scatter takes place sets the grid volume within which scatter occurs, and hence the scatter type. The interaction subsequently influences the contribution of radiance to the photon path segment between this and the previous interaction, and also determines a new direction vector for the photon path from that position. Because the process traces the photon backwards from an

observation point, contributions of radiance from the later path segments are diminished due to extinction along the path between a given segment and the observer.

The zenith and azimuth of the scattering angle are chosen from random functions which are biased according to the scatter type. If the scatter type is for a solid surface, the scattering is assumed to be isotropic. In this case, the photon's incoming direction is irrelevant, and the new zenith angle is chosen at random (between 0° and 90°). For Rayleigh scatter, the zenith angle between the old and new direction vectors (*i.e.* the scattering angle) is chosen at random. For Mie scatter, the scattering zenith angle is selected by random sampling of the cumulative phase function array. The cumulative array is used in order to increase the probability that angles corresponding to the maxima of the phase function will be chosen. Finally, the azimuth angle of scattering is selected at random, based on the assumptions that, (1) solid surface scatter is isotropic, and (2) the Rayleigh and Mie scatterers are spheres. The model grid volumes are delimited by horizontally parallel boundaries in the east-west and north-south directions, and vertically-spaced spherical shell levels.

### 3.4.3 Numerical results

The radiance calculated by the Monte Carlo model is non-dimensional. The results of the adding-and-doubling model discussed in the previous section are also a relative radiance, but are produced per unit solid angle ($sr^{-1}$) and thus must be multiplied by $\pi$ for direct comparison to the Monte Carlo model. The ray-tracing philosophy of the Monte Carlo procedure provides both the zenith and azimuth angular dependance of scattering.

The Monte Carlo (MC) results were tested against those published by Coulson *et al.* (1960) (CDS) for radiance downwelling from a Rayleigh atmosphere. The comparison is shown in Figure 3.6, which is valid for a 0.55-$\mu$m wavelength, solar zenith angle of 53°, azimuth angle of 0°, and atmospheric optical depth of 0.1.

The adding model compared well to the Monte Carlo model in several point comparisons for small cloud optical depths. Computations at cloud optical depths larger than 8 were not carried out due to the computational requirements. Figure 3.7 presents a comparison of reflectance calculated for a homogeneous cloud layer representing the Stratus 2

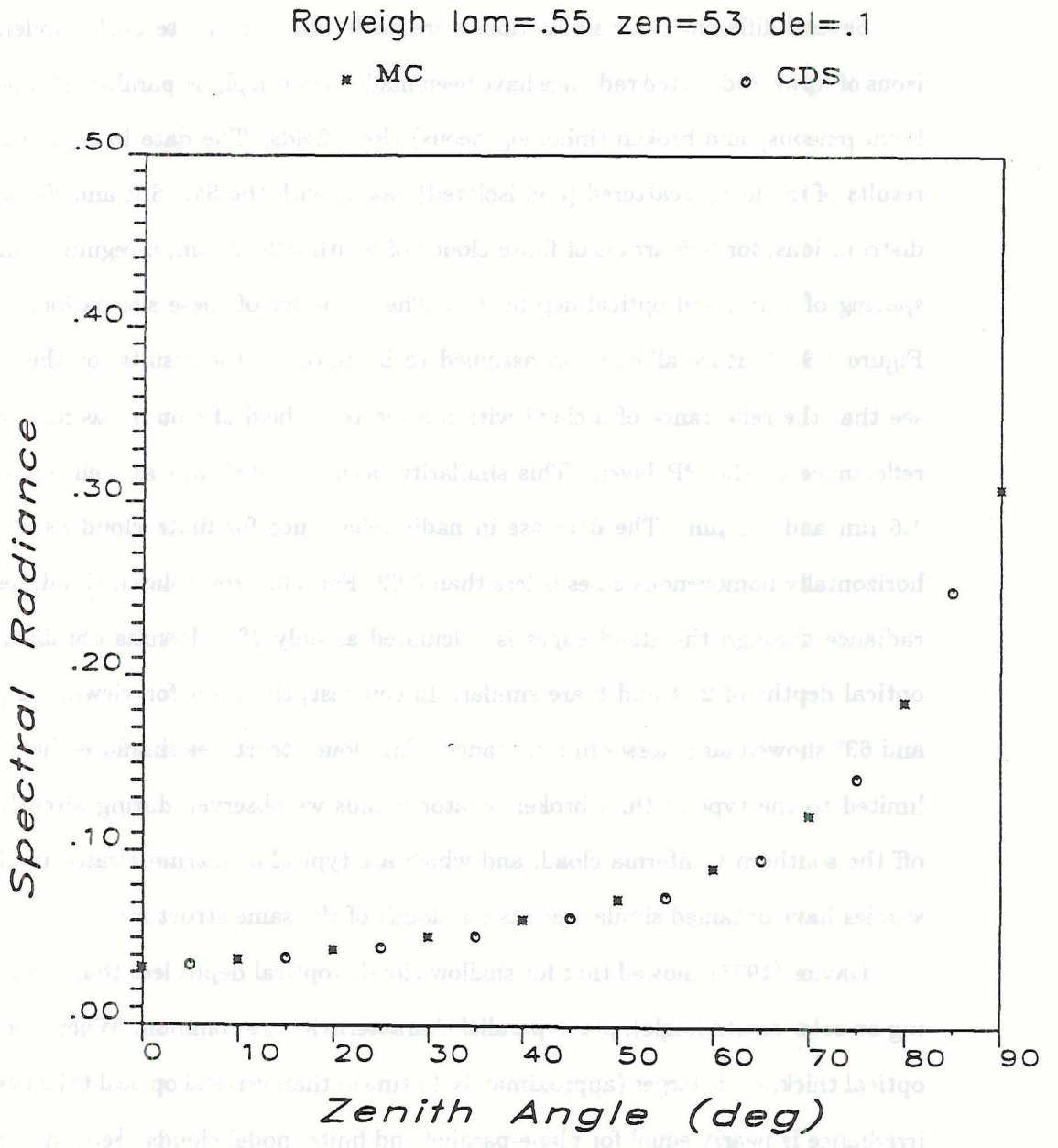


**Figure 3.6: Downward radiance of a Rayleigh atmosphere as a function of viewing zenith angle for the Monte Carlo model and the results of Coulson *et al.* (1960).**

droplet size distribution. The agreement of the Monte Carlo model and the adding model results is actually better than that of the adding model utilizing the Henyey-Greenstein phase function versus the Mie phase function.

Several different cloud simulations were made with the Monte Carlo model. Comparisons of upward-directed radiance have been made between plane-parallel (PP; horizontally homogeneous) and broken (inhomogeneous) cloud fields. The data in Figure 3.8 present results of modeling scattered (and isolated) clouds with the St2, Sc1 and F4 particle size distributions, for 5x5 arrays of finite clouds of width 0.2–1.0 km, a regular cloud element spacing of 1 km, and optical depths 2–8. The geometry of these simulations is shown in Figure 3.9. Surface albedo was assumed to be zero. In the results for these cases, we see that the reflectance of a cloud within a scattered field of clouds has nearly the same reflectance as the PP layer. This similarity occurs at 0.85 $\mu$m as well as at 0.65 $\mu$m, 1.6 $\mu$m and 2.1 $\mu$m. The decrease in nadir reflectance for finite cloud as compared to horizontally homogenous cases is less than 0.02. For a 0.5-km isolated cloud, loss of nadir radiance through the cloud edges is calculated as only 1%. Results obtained for cloud optical depths of 2, 4 and 8 are similar. In contrast, the cases for viewing angles of 30° and 63° showed large losses in reflectance. The cloud structures simulated here have been limited to the type of thin, broken stratocumulus we observed during aircraft sampling off the southern California cload, and which are typical of marine stratocumulus. Other studies have obtained similar results for clouds of the same structure.

Davies (1978) showed that for shallow clouds (optical depth less than 10–20, depending on solar zenith angle), plane-parallel characteristics are common. When the horizontal optical thickness is larger (approximately 10 times) than vertical optical thickness, upward irradiance is nearly equal for plane-parallel and finite model clouds. Secondly, cloud radiance differences for shallow finite and infinite cloud are shown by Davis *et al.* (1979) to be a minimum near nadir, increasing with the viewing zenith angle. Foot (1988) showed that the 1.6 $\mu$m nadir reflectance (normalized against the 1.2 $\mu$m reflectance) obtained from a Monte Carlo model, for cloud 100 m in depth cloud top undulations of 200 m width, was reduced only 3% from the plane-parallel reflectance.

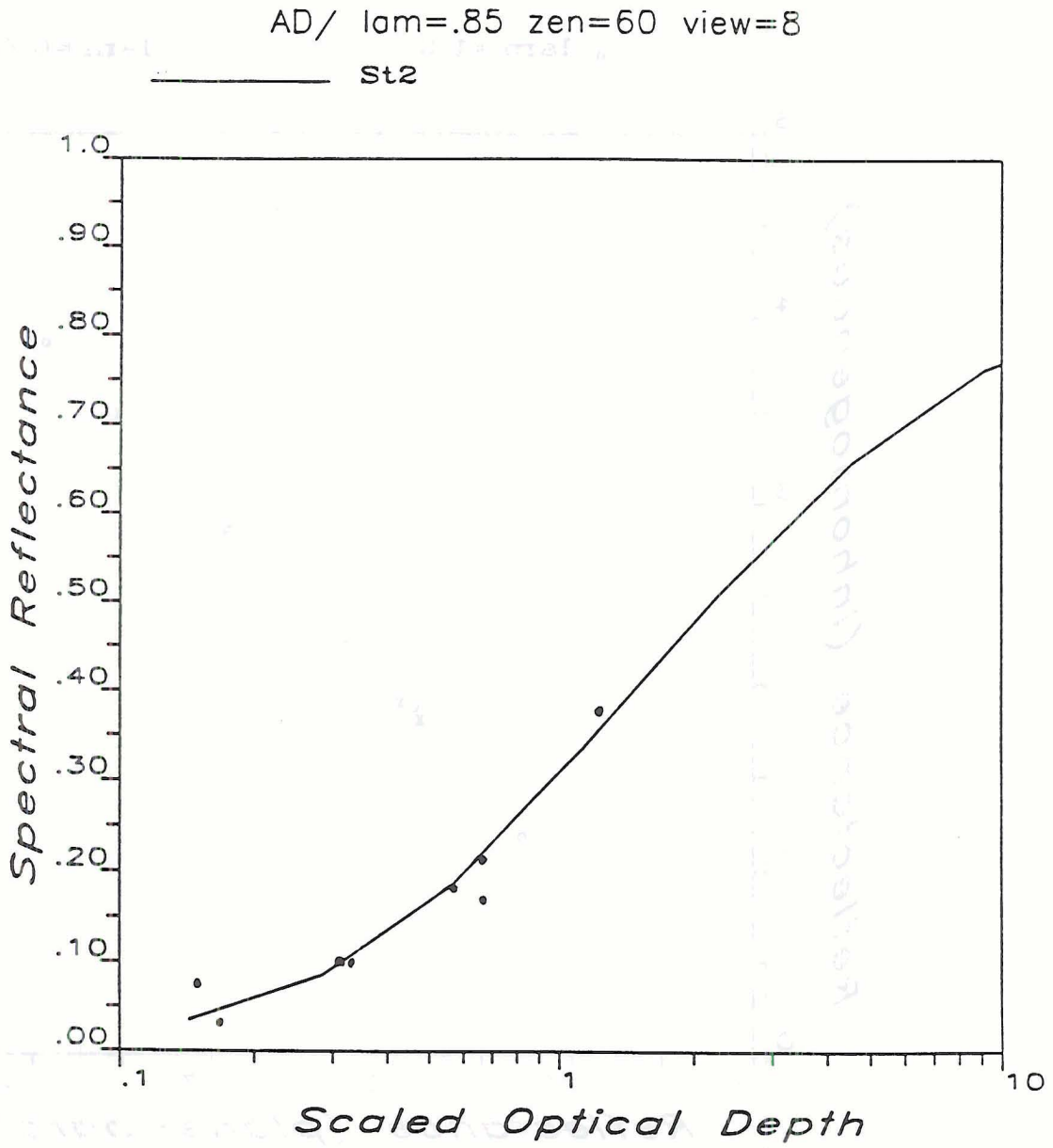


Figure 3.7: Reflectance from the AD model and a group of Monte Carlo model results.

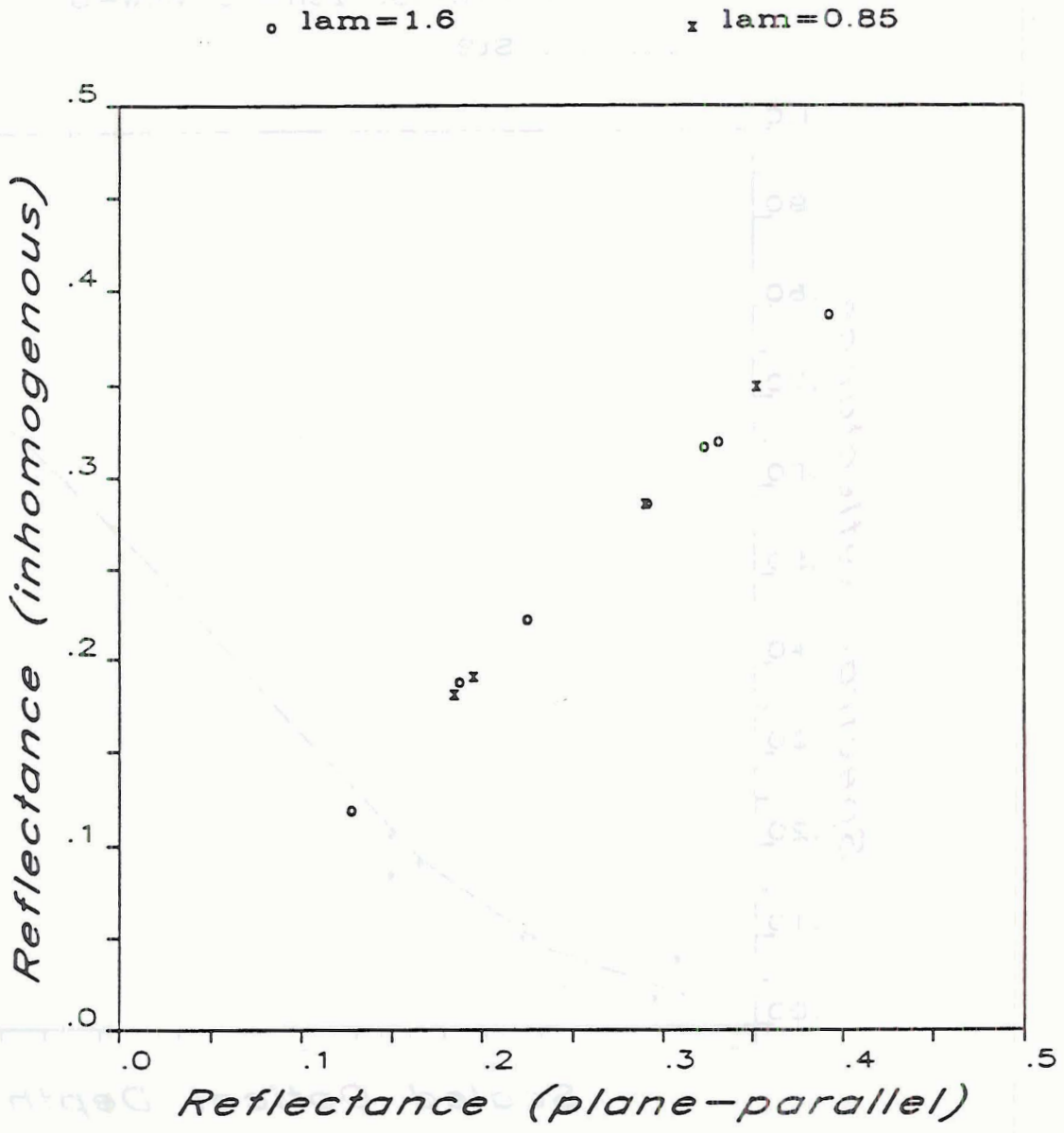


Figure 3.8: Reflectance calculated from Monte Carlo model for plane-parallel and broken cloud layers.

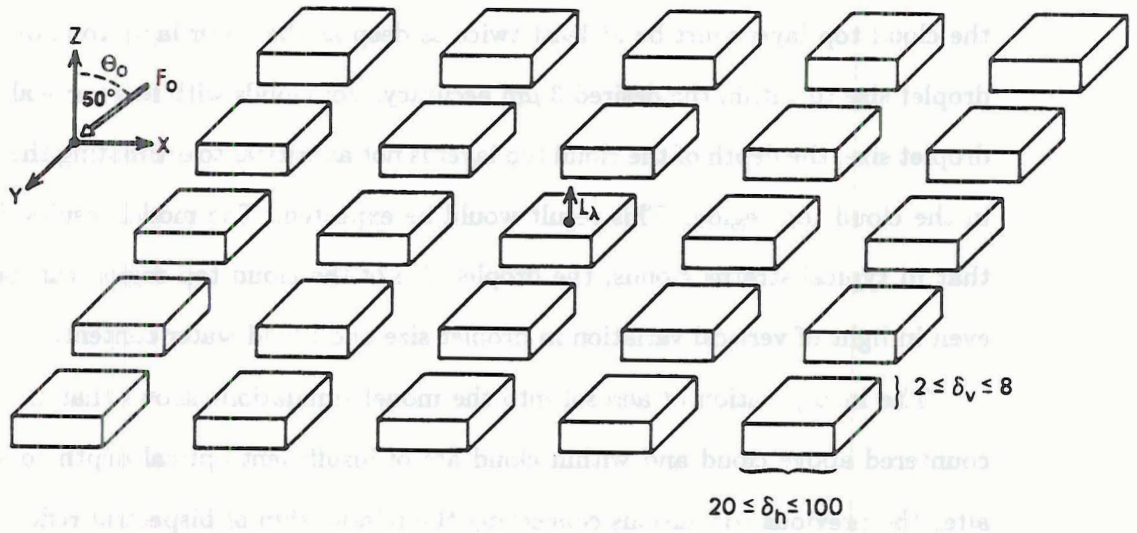


Figure 3.9: Schematic of cloud structures simulated with the Monte Carlo model. Cubic clouds are arranged in the x-y plane, with the range of optical thickness indicated for the horizontal ($\delta_h$) and vertical ($\delta_v$).

The observation of cloud reflectance from a nadir-viewing sensor minimizes the effects of energy loss from cloud sides. The shallowness of the cloud elements with respect to cloud width has the same effect. Similarity of finite cloud reflectances to the plane-parallel values leads to the conclusion that horizontal inhomogeneity will not strongly influence nadir spectral reflectance from thin stratus.

## 3.5 Chapter summary

The effects of vertical and horizontal inhomogeneity on spectral reflectance relationships have been examined in this chapter. Multilayer clouds were simulated using the Adding model. Three simulations representing vertical variation in the droplet size distribution demonstrate the controlling influence of cloud top microphysics in determining reflectance. In the case where the effective radius of the cloud top layer is much larger than that of the cloud base (15 $\mu$m versus 5 $\mu$m), which may occur in thicker stratus, the cloud top layer must be at least twice as deep as the lower layer to allow retrieval of droplet size to within the desired 3 $\mu$m accuracy. For clouds with less vertical variation in droplet size, the depth of the cloud top layer is not as critical to estimating the droplet size in the cloud top region. This result would be expected. The model results demonstrate that in typical stratus clouds, the droplet size of the cloud top region can be estimated even in light of vertical variation in droplet size and liquid water content.

The incorporation of aerosol into the model simulations shows that the aerosol encountered above cloud and within cloud are of insufficient optical depth to significantly alter the previous conclusions concerning the relationship of bispectral reflectances to effective radius. However, the presence of a haze layer between cloud base and the surface provides a larger optical depth. In the cases where the cloud layer itself is thin, extinction in this underlying haze has been calculated. The haze is assumed to have the properties of oceanic aerosol near saturation. The extinction is greater at 1.6 $\mu$m than at 0.85 $\mu$m, so that transmission of the shortwave energy through cloud leads to smaller relative backscattering at the longer wavelength. The resulting increase in estimated effective radius is dramatic for cloud scaled optical depths less than 1.0, corresponding to a 0.85-$\mu$m optical

depth of approximately 7. The actual cloud depths necessary to eliminate the effects of underlying haze would be determined by individual cloud layer and aerosol characteristics, but the results shown in this Chapter are typical of marine stratus conditions. Without the presence of a concentrated haze layer, the cloud droplet size should be retrievable from thinner cloud (optical depth of 4 or greater). The aircraft data of aerosol and droplet size distributions obtained during the California field program of this study provided realistic microphysical conditions on which to base the simulations of cloud and haze layers. The Australian program data set allows detailed comparison of spectral reflectance and cloud droplet populations with model-derived retrievals of effective radius. The field programs are discussed in Chapter 4 in association with the results of radiometric measurements, and in the Appendix.

The effects of horizontal inhomogeneity on spectral reflectance at nadir views were briefly explored through the use of the Monte Carlo multiple scattering radiative transfer model. Intercomparison of the nadir reflectance at the 0.85- and 1.6-$\mu$m wavelengths for plane parallel and broken or isolated thin stratus elements demonstrated little deviation. The work of previous, more general applications of Monte Carlo modeling is called upon, to conclude that these thin stratus have relatively little energy directed outward toward the lateral cloud edges, particularly with respect to that which would ordinarily exit in the nadir direction for the plane parallel cases. Simulations for cloud layers with optical depth larger than 8 were not pursued, due to computing constraints and the small optical depth of the cloud layers which were sampled during the field programs.

The combined results of the simulations summarized above indicate that thin stratiform clouds such as were sampled during the field programs may demonstrate the predicted relationship between bispectral reflectance and effective radius in the cloud top layer, if optical depths were large enough to allow the relative extinction at 1.6 $\mu$m under the influence of cloud droplet size. The next Chapter addresses the observed microphysical characteristics of stratus during two field sampling programs, and the results of comparing these characteristics to the radiometric data obtained simultaneously and to the estimated values of cloud droplet effective radius.

project through the cooperation and support of NOSC. Specific descriptions of the instrumentation, including the pyranometer and radiometer components from Colorado State University (CSU) which were installed on the Navajo for this field project, are given in the Appendix.

The aircraft was flown in near-coastal areas at different times during the daylight hours. The measurement flight periods for June 1986 are listed in Table A.1. Time references are given as Coordinated Universal Time (UTC).

Table 4.1: Aircraft measurement periods during June 1986.

| *Date* | *Julian day* | *Time period (UTC)* |
|---|---|---|
| 24 June | 175 | 2012–2201 |
| 25 June | 176 | 2202–2340 |
| 26 June | 177 | 1523–1744 |
| 27 June | 178 | 0132–0250 |
| 28 June | 179 | 1406–1445 |
| 28 June | 179 | 1555–1612 |
| 29 June | 180 | 1420–1755 |
| 30 June | 181 | 1418–1757 |

The aircraft flight sequences were designed to provide measurements of cloud radiance directly above cloud top and cloud microphysical structure within the cloud top layer. The CSU Spectral Radiometer (SR), manufactured by CI, Ltd. as Model SR-1000 was utilized. The SR was positioned in the tail section of the Navajo aircraft looking toward nadir, to provide measurements of upward radiances. The time resolution of the sampling was 0.1 second, and occasionally 0.2 seconds, and aircraft velocity was nominally 54 m $s^{-1}$. During fixed-wheel operation of the SR, this provided high spatial resolution data for a given filter, and during DFW scan sequences this sampling produced several sets of multiple filter radiances during an aircraft pass over the cloud top. The fixed filter mode was utilized to observe horizontal variability of cloud upward radiance, and the filter scan mode was operated to intercompare the radiances at 0.65, 0.85, and 1.60 $\mu$m wavelengths.

The Spectral Radiometer provided only upward radiance measurements, so an estimate of downward spectral flux was required in order to calculate the spectral reflectance.

The spectral filters transmit only a small percentage of the total solar irradiance. Table 4.2 lists the typical percentage of solar irradiance at 1 km elevation contained within the SR filter bands, as calculated from LOWTRAN estimates based on soundings taken during the field sampling periods.

Table 4.2: Percentage of downwelling solar flux within each of the Spectral Radiometer filter channels.

| *Filter wavelength* ($\mu$m) | *Filter width* ($\mu$m) | *Irradiance* (%) |
|---|---|---|
| 0.65 | 0.0106 | 1.4 |
| 0.85 | 0.0103 | 0.99 |
| 1.64 | 0.1524 | 4.0 |

The sensitivity of downwelling spectral irradiance in the visible and NIR windows to variations in aerosol and water vapor were examined using the LOWTRAN-6 atmospheric transmission model, which incoporates specific extinction parameters for aerosol (marine haze, tropospheric aerosol, and stratospheric aerosol) and atmospheric gases (Kneizys *et al.*, 1983). Assuming the sun-target-sensor geometry is known and the climatological atmospheric profile is chosen, the probable error of LOWTRAN flux estimates is primarily controlled by the boundary layer profile. The values of downwelling spectral irradiance in the Spectral Radiometer bands were obtained by using *in situ* measurements of flux obtained from the Eppley pyranometers. Field measurements of downwelling solar flux agreed closely with the LOWTRAN estimates to altitudes above the inversion, but sharp decreases in solar flux (up to 20%) were recorded as the aircraft moved from above to below the inversion, due to haze (and smog) occurring near the coast.

These variations were reproducible in the LOWTRAN estimates by using the "marine aerosol" model options of LOWTRAN. This model option required the use of a vertical sounding which locates the height of the boundary layer. The error in estimating spectral solar flux is generally less than the observed reduction in total solar flux, due to the use of water vapor window channels. However, examination of the trends in the upwelling signal

in the spectral radiometer measurements above cloud indicated that significant extinction of the direct solar beam occurred at the 0.65-$\mu$m wavelength, and not in the two near-infrared channels, as the aircraft descended from above to within the inversion. Remote sensing methods which rely on extinction models such as LOWTRAN to estimate solar spectral irradiance at cloud top may have greater uncertainty with the 0.65 $\mu$m band. Our subsequent analysis will focus on the variations in the 0.85-$\mu$m and 1.6-$\mu$m measurements only.

### 4.1.2 Australian program

A complete description of the experimental procedures, instrumentation, and several interesting conclusions for this program are given in the paper by Stephens and Platt (1987). A brief summary is provided here as background to the following analysis. An aircraft observational program was carried out to study the spectral variation in cloud reflectivity. The Australian CSIRO Fokker F-27 aircraft was equipped with a spectrally scanning radiometer (SPERAD), a narrow field of view infrared radiometer, upward- and downward-looking pyradiometers and pyrgeometers, and PMS cloud microphysics probes for droplets and precipitation. Aerosol-sized particles (radii less than 2 $\mu$m) were not sampled. Standard thermodynamic parameters were recorded. Thirteen flights were conducted during May-June 1984 off the east coast of Australia. The spectral reflectances and other variables were obtained for stratocumulus and cumulus clouds, primarily over the ocean.

The SPERAD instrument system provided downward-viewed calibrated cloud reflectances in 72 spectral channels ranging from 0.4 to 2.5 $\mu$m wavelength, 10 Hertz. At the typical aircraft speed, this sampling rate supplied a complete reflectance spectrum every 8 meters along the aircraft path. Droplet size distributions were recorded at 1 Hertz. The cloud internal structure was characterized by several constant-altitude passes at various elevations within cloud. The most significant differences between the data supplied from this experiment were the availability of nearly coincident multispectral reflectances at very high spatial resolution, and the fact that the reflectances themselves were determined directly from well calibrated upward radiance and downward flux measurements.

Thus, these data provide more detailed and quantitative information on cloud reflectance variability.

## 4.2 Results from California measurement program

### 4.2.1 Microphysical data

The data obtained from the measurement program were utilized in model representations of marine stratus cloud and aerosol layers. In general, the cloud layers sampled during the California field program were characterized by small mean and effective droplet radii. The flights showed that liquid water content as well as effective radius increased toward cloud top, reaching maxima of $W \approx 0.1$ g m$^{-3}$ and $r_e \approx 6$ $\mu$m. Microphysical parameters were derived both for the entire particle size distribution measured, including both aerosol and droplets, as well as the droplet size distribution (excluding aerosol).

Table 4.3 presents a summary of parameters of the droplet size distributions which were sampled in three of the research flight periods. Calculations of these parameters did not include particles in the aerosol size ranges (less than 2 $\mu$m radius).

Table 4.3: Average values of mean radius, effective radius, liquid water content and number concentration for droplet size distributions on Julian days 175 and 177.

| *Label* | $Z$ $(m)$ | *Description* | $\overline{r_m}$ $(\mu m)$ | $\overline{r_e}$ $(\mu m)$ | $\overline{W}$ $(g\ m^{-3})$ | $\overline{N}$ $(cm^{-3})$ |
|---|---|---|---|---|---|---|
| 175A | 518 | Cloud top | 5.40 | 6.25 | 0.113 | 136 |
| | 488 | Below top | 4.90 | 5.93 | 0.078 | 119 |
| | 427 | In cloud | 4.07 | 5.14 | 0.051 | 129 |
| 177A | 549 | Above cloud | 2.37 | 2.41 | <0.001 | <1 |
| | 457 | Cloud tops | 4.95 | 6.21 | 0.004 | 6 |
| | 427 | Upper cloud | 4.65 | 5.50 | 0.088 | 161 |
| | 396 | In cloud | 4.35 | 5.39 | 0.062 | 131 |
| | 366 | In cloud | 3.81 | 4.78 | 0.027 | 85 |
| 177B | 427 | Cloud top | 4.60 | 5.57 | 0.112 | 206 |
| | 396 | In cloud | 4.55 | 5.53 | 0.095 | 180 |
| | 366 | In cloud | 3.86 | 4.90 | 0.032 | 94 |
| | 335 | In cloud | 3.51 | 4.52 | 0.013 | 50 |

The average values and dispersion (ratio of standard deviation to mean) for effective radius, liquid water content, and number concentration of the particle size distributions obtained while sampling extended cloud, scattered cloud, and clear air are listed in Table 4.4.

Table 4.4: Mean and dispersion values for particle size distributions on Julian days 175–178.

| *Label* | $Z$ $(m)$ | *Description* | $\overline{r_e}$ $(\mu m)$ | $D_{r_e}$ | $\overline{W}$ $(g\ m^{-3})$ | $D_W$ | $\overline{N}$ $(cm^{-3})$ | $D_N$ |
|---|---|---|---|---|---|---|---|---|
| 175A | 518 | Cloud top | 4.69 | 0.532 | 0.114 | 0.822 | 377 | 0.373 |
| | 488 | Below top | 4.78 | 0.479 | 0.080 | 0.803 | 346 | 0.307 |
| | 427 | In cloud | 4.78 | 0.142 | 0.052 | 0.511 | 334 | 0.178 |
| 177A | 549 | Above cloud | 0.314 | 0.083 | <0.001 | 0.353 | 41 | 0.270 |
| | 457 | Cloud tops | 1.65 | 1.45 | 0.004 | 2.50 | 99 | 0.586 |
| | 427 | Upper cloud | 4.93 | 0.297 | 0.088 | 0.457 | 337 | 0.226 |
| | 396 | In cloud | 5.21 | 0.086 | 0.063 | 0.308 | 316 | 0.120 |
| | 366 | In cloud | 4.40 | 0.143 | 0.028 | 0.271 | 295 | 0.097 |
| 177B | 427 | Cloud top | 5.41 | 0.091 | 0.113 | 0.333 | 339 | 0.169 |
| | 396 | In cloud | 5.37 | 0.079 | 0.096 | 0.231 | 321 | 0.088 |
| | 366 | In cloud | 4.50 | 0.158 | 0.033 | 0.349 | 309 | 0.115 |
| | 335 | In cloud | 3.62 | 0.183 | 0.014 | 0.654 | 302 | 0.099 |
| 178A | 457 | Above haze | 0.316 | 0.105 | <0.001 | 0.244 | 48 | 0.236 |
| | 305 | At inversion | 0.324 | 0.064 | <0.001 | 0.735 | 135 | 0.584 |
| | 122 | In haze | 0.732 | 0.846 | <0.001 | 1.16 | 256 | 0.197 |
| | 30 | In haze | 0.518 | 0.179 | <0.001 | 0.262 | 523 | 0.228 |

Averaging of size distributions along constant-altitude flight segments reveal a decrease in the mean value of the effective radius at lower altitudes below cloud top. Figure 4.1 and Figure 4.2 present summaries of the height dependency for effective radius and variation of $r_e$ computed from the entire particle size distribution, including the aerosol sizes. Comparison of Figure 4.2 with Figure 4.3, and Figure 4.4 with Figure 4.5 demonstrates how the inclusion of the aerosol population decreases magnitudes of $r_e$ very little but decreases $r_m$ values quite sharply. The liquid water contributed by sampled particles in the aerosol size range was less than 0.005 $g\ m^{-3}$.

Aerosol concentrations above the boundary layer were lower than those below or within cloud, due to the relative humidity and assumed source mechanisms. The cloud

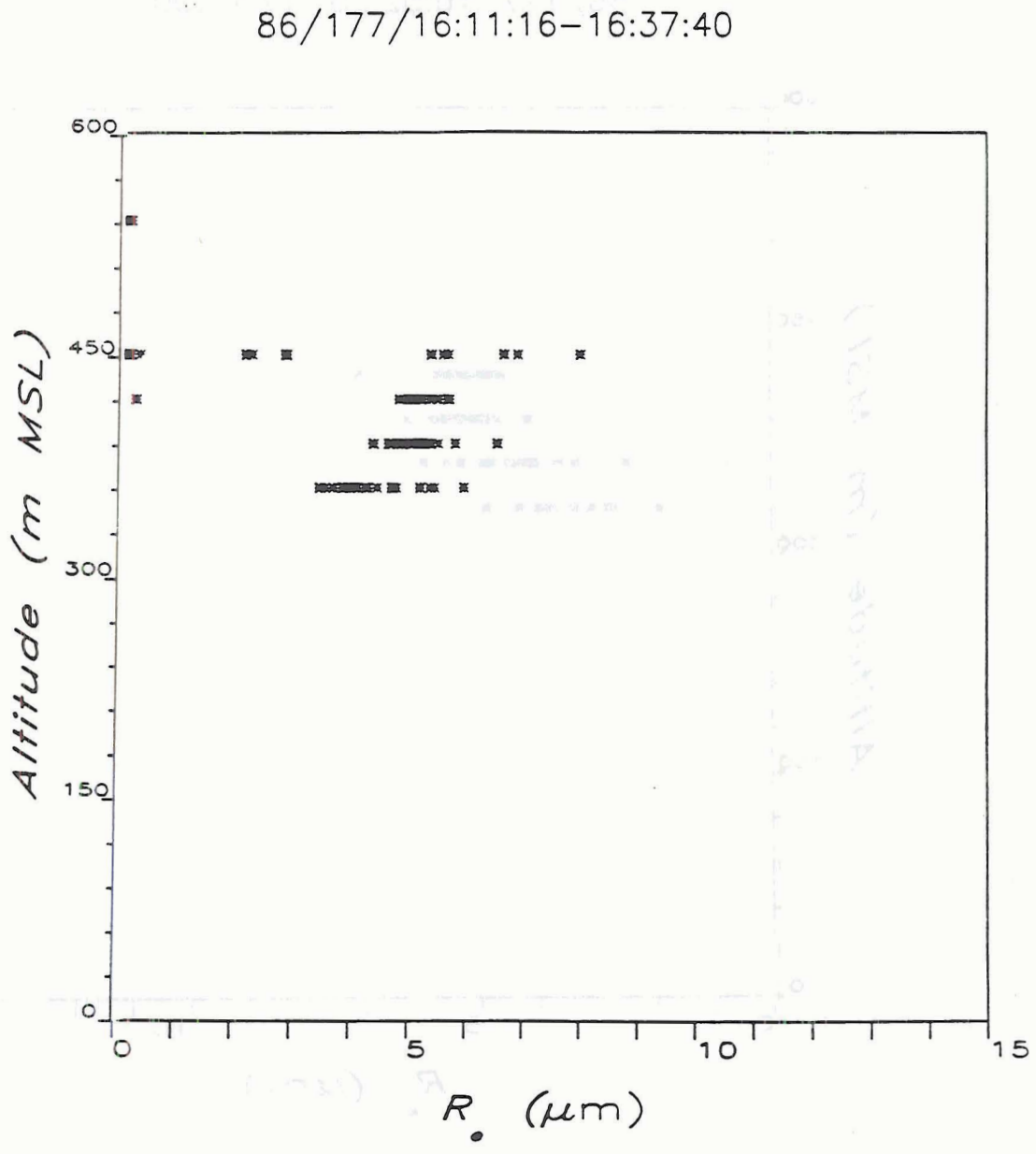


Figure 4.1: Particle effective radius measured during flight 177A.

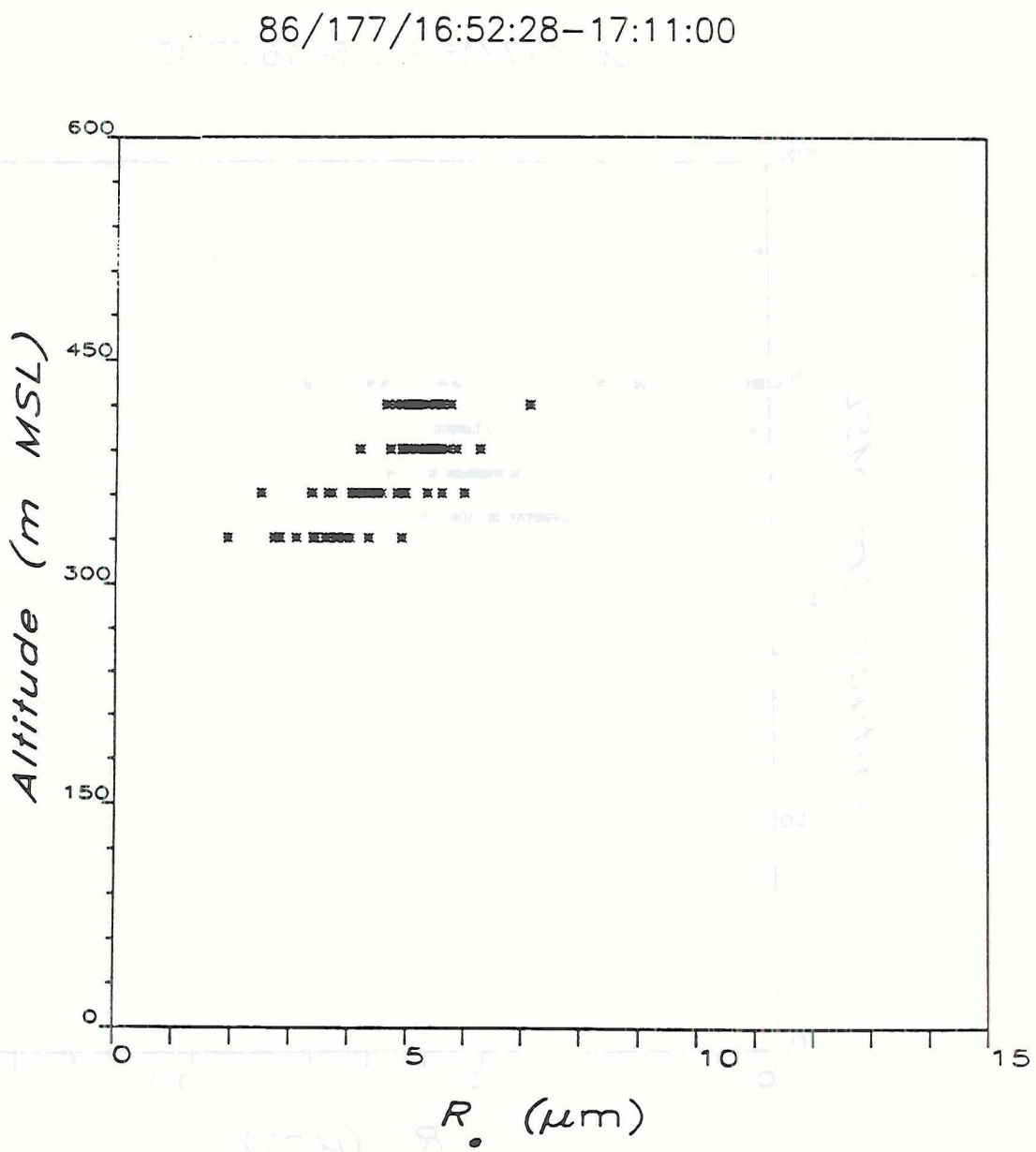


Figure 4.2: Particle effective radius measured during flight 177B.

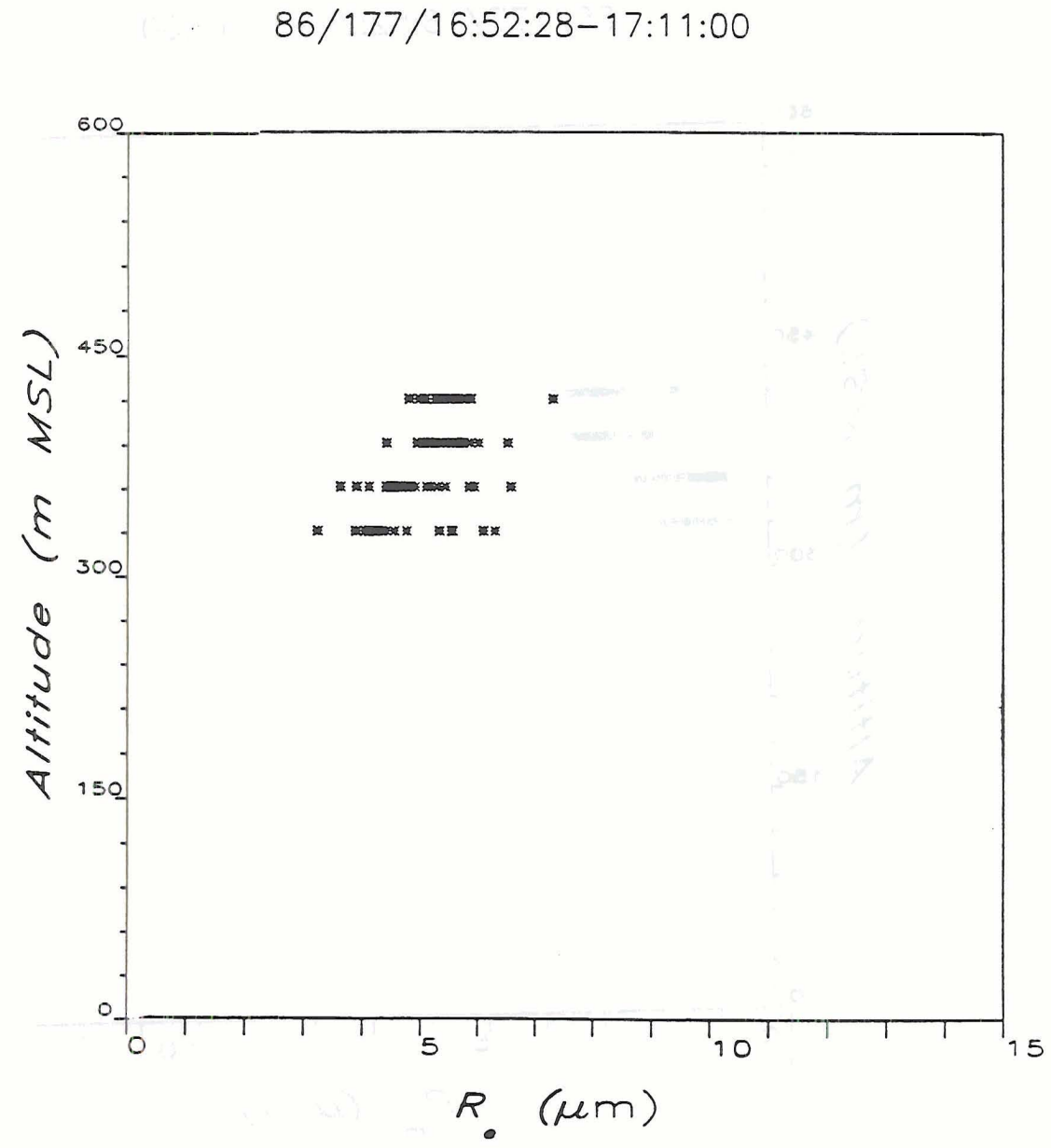


Figure 4.3: Droplet effective radius measured during flight 177B (without aerosol population).

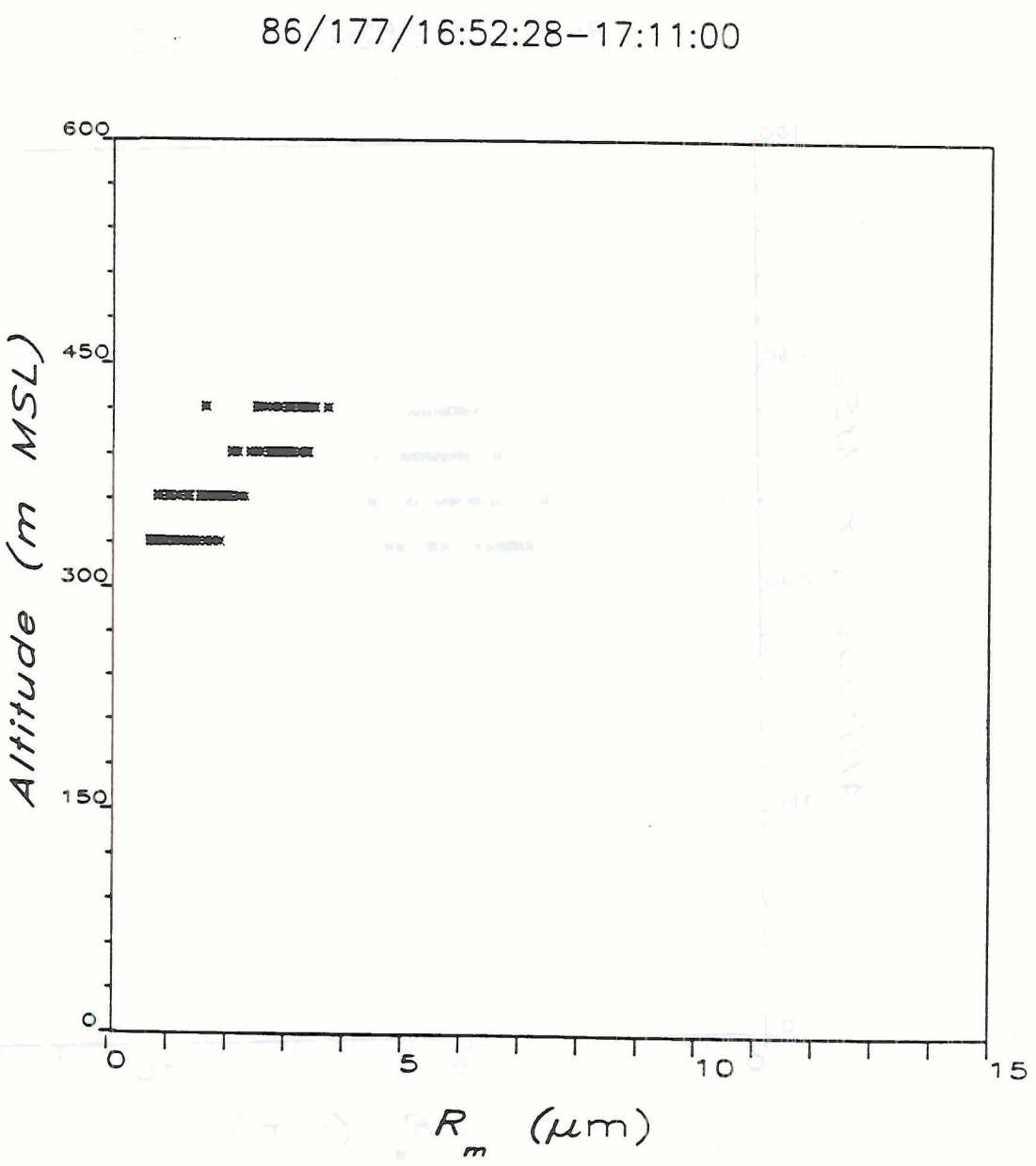


Figure 4.4: Particle mean radius measured during flight 177B.

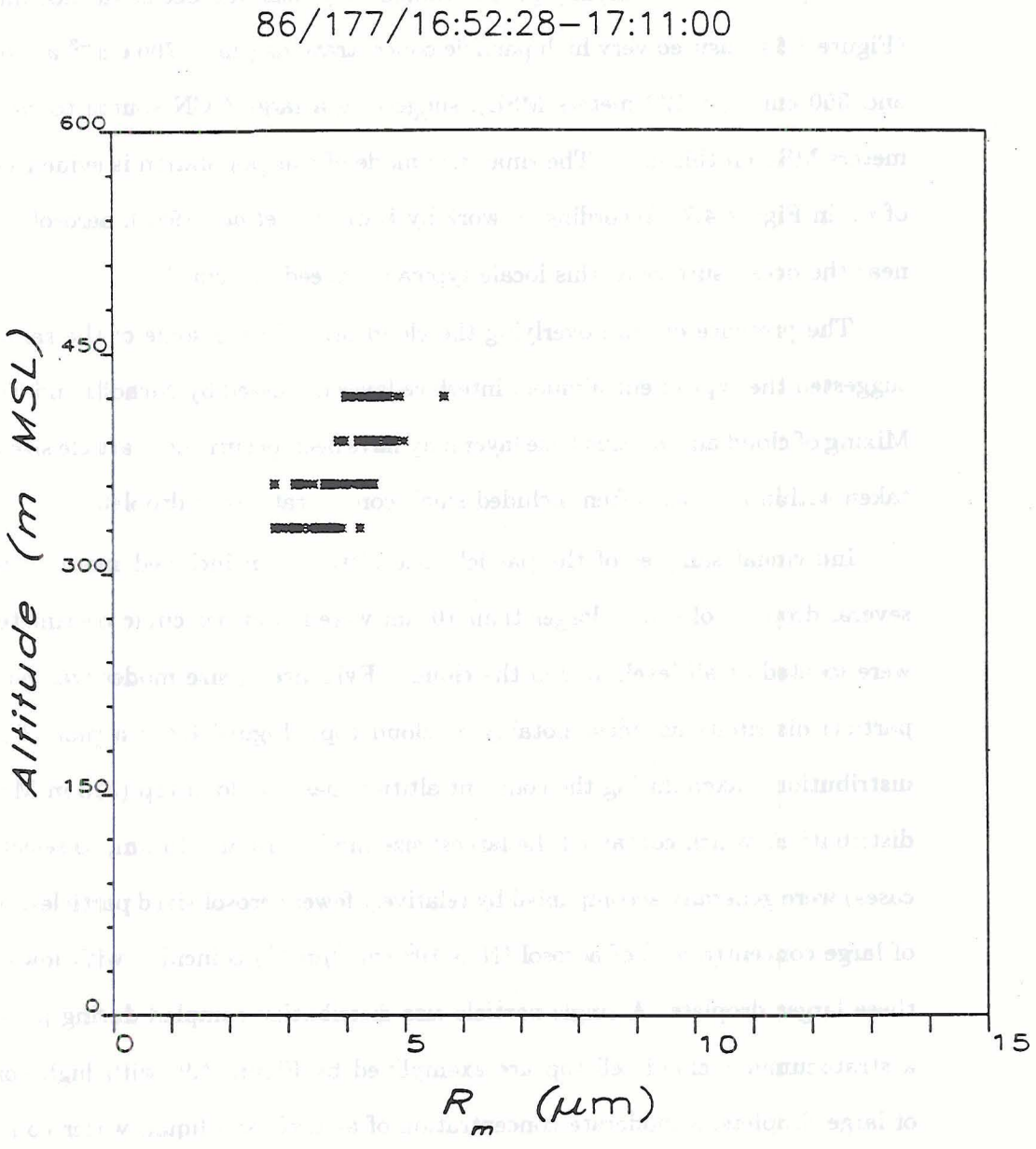


Figure 4.5: Droplet mean radius measured during flight 177B (without aerosol population).

top was located at or a short distance below the boundary layer temperature inversion. Above the inversion, aerosol concentrations were less than 100 $cm^{-3}$. It is possible that aerosol within the cloud layer were transported through the lower cloud boundary from a sea spray source. A sampling pass obtained very near the ocean surface during day 178 (Figure 4.6 measured very high particle concentrations (up to 700 $cm^{-3}$ at 30 meters MSL and 350 $cm^{-3}$ at 122 meters MSL), suggesting a large CCN source to cloud base (183 meters MSL on this day). The small size mode of this population is evidenced by the plot of $r_m$ in Figure 4.7. According to work by Battalino *et al.* (1982), aerosol concentrations near the ocean surface at this locale typically exceed $10^2$ $cm^{-3}$.

The presence of haze overlying the cloud layer during some of the sampling periods suggested the type of entrainment interface layer discussed by Nicholls and Turton (1986). Mixing of cloud air into this haze layer may have been occurring. Particle size distributions taken within the haze often included small concentrations of droplets.

Individual samples of the particle size distribution included many instances where several droplets of radius larger than 10 $\mu$m were found per cubic centimeter, and these were located at all levels within the clouds. Evidence of size modes was recorded in the particle distributions, most notably at cloud top. Figure 4.8 is a plot of multiple size distributions taken during the constant altitude pass at cloud top (518 m MSL). The size distributions which contained the largest size modes (10 and 15 $\mu$m, to select two general cases) were generally accompanied by relatively fewer aerosol-sized particles. The presence of large concentrations of aerosol ($N > 10^3$ $cm^{-3}\mu m^{-1}$) coincided with lower numbers of these larger droplets. A single particle size distribution sampled during passage through a stratocumulus cloud cell top are exemplified by Figure 4.9, with high concentrations of large droplets, a moderate concentration of aerosol, and liquid water content equal to approximatlely 0.1 g $m^{-1}$.

Much more uniformity in the size distributions was encountered while fully in stratiform cloud, as shown by Figure 4.10. Fluctuations in $r_e$ along the constant-altitude flight tracks were generally less than 2.0$\mu$m, except for those flight levels immediately at cloud upper and lower boundaries, during which the PMS probes were in and out of cloudy

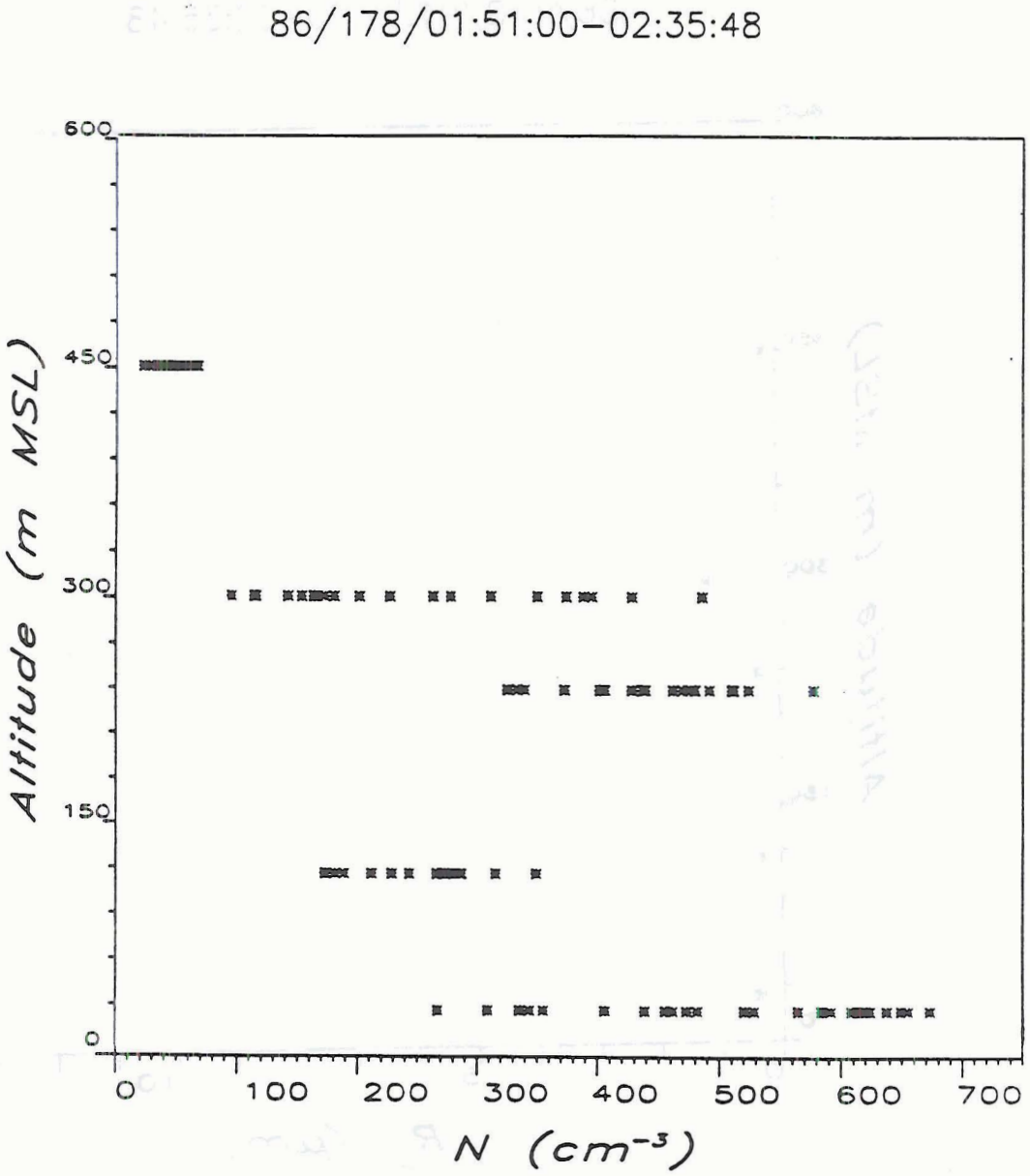


Figure 4.6: Particle number concentration measured during flight 178A.

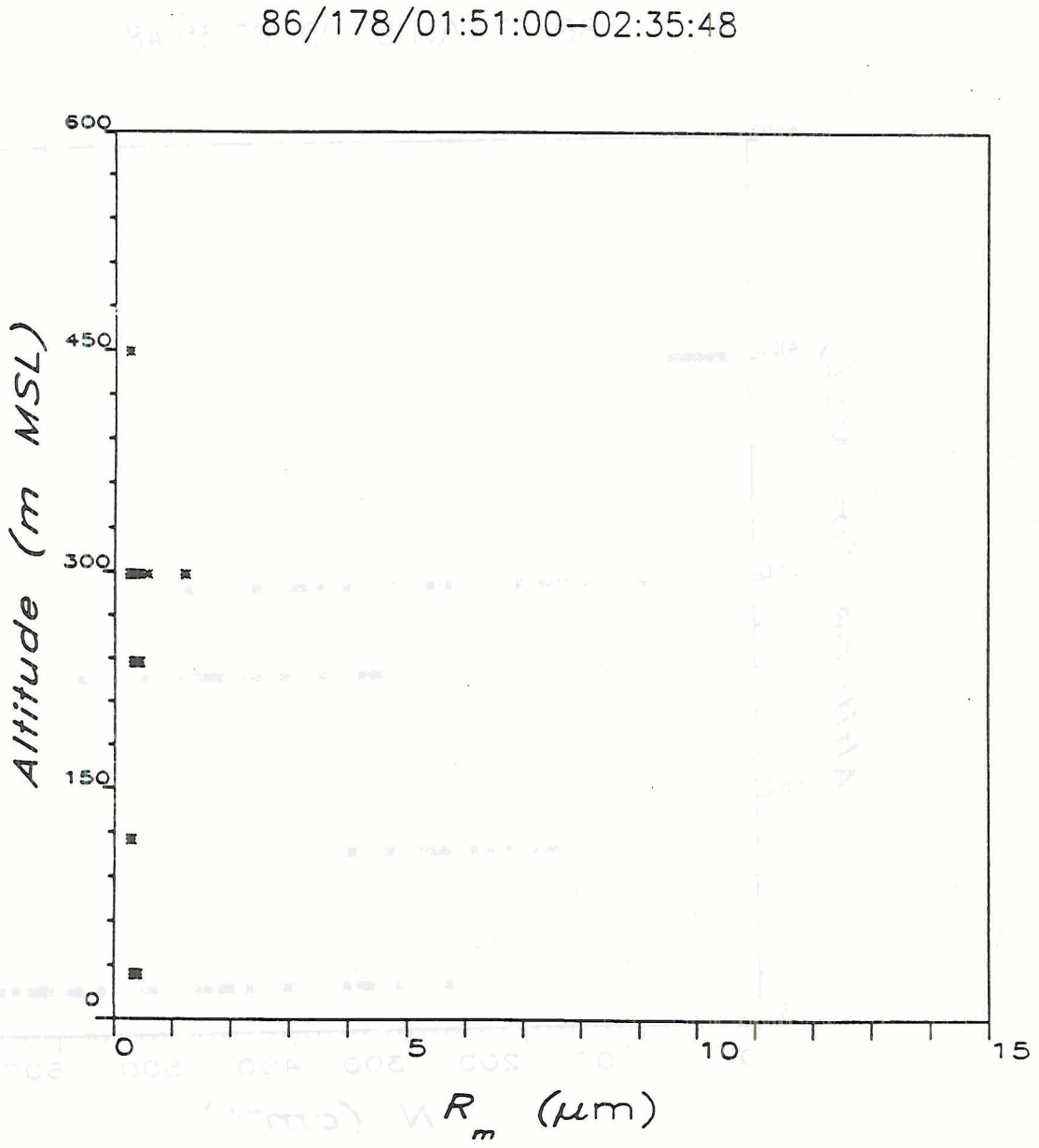


Figure 4.7: Particle mean radius measured during flight 178A.

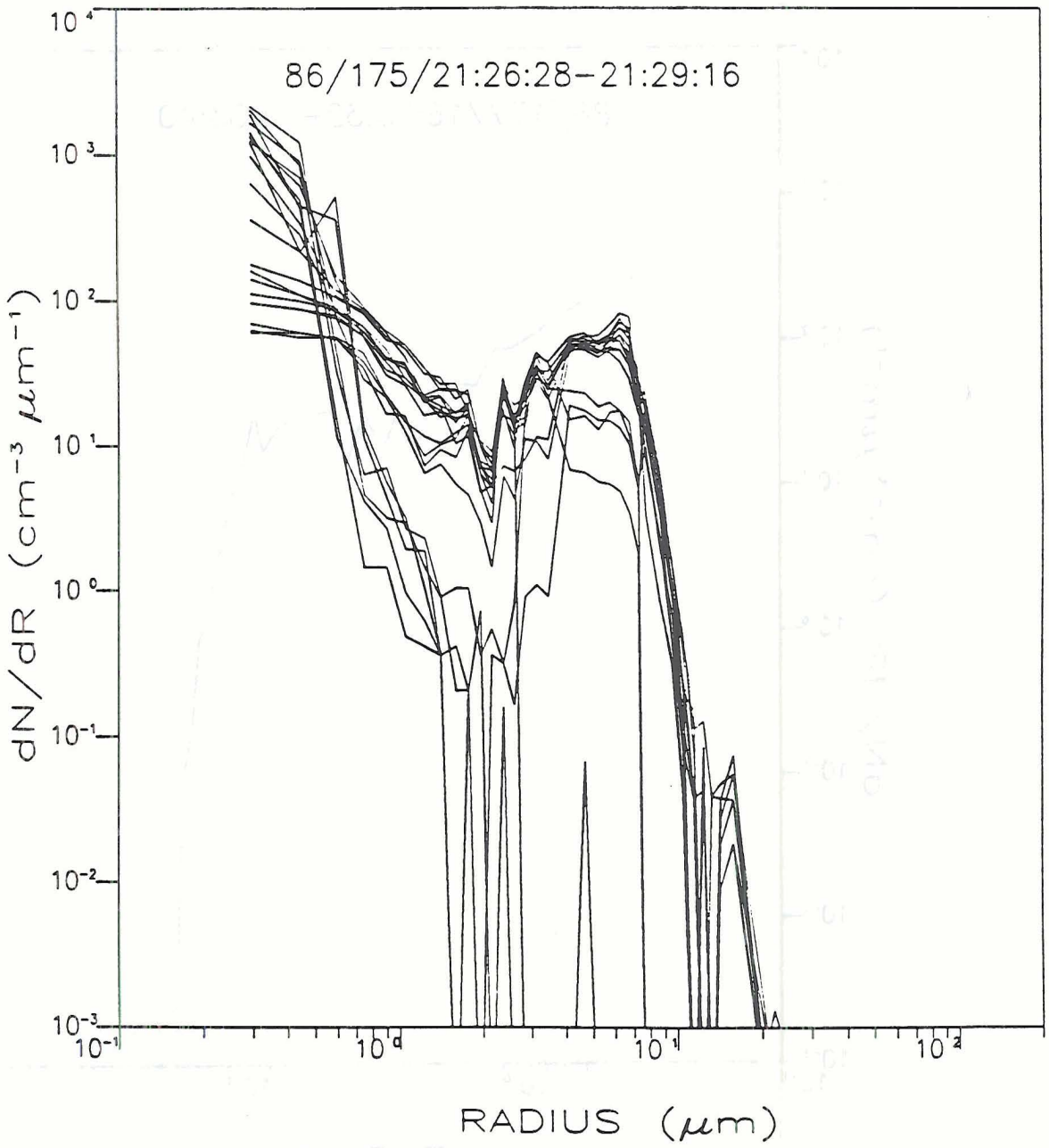


Figure 4.8: Particle size distributions sampled along a flight track at cloud top.

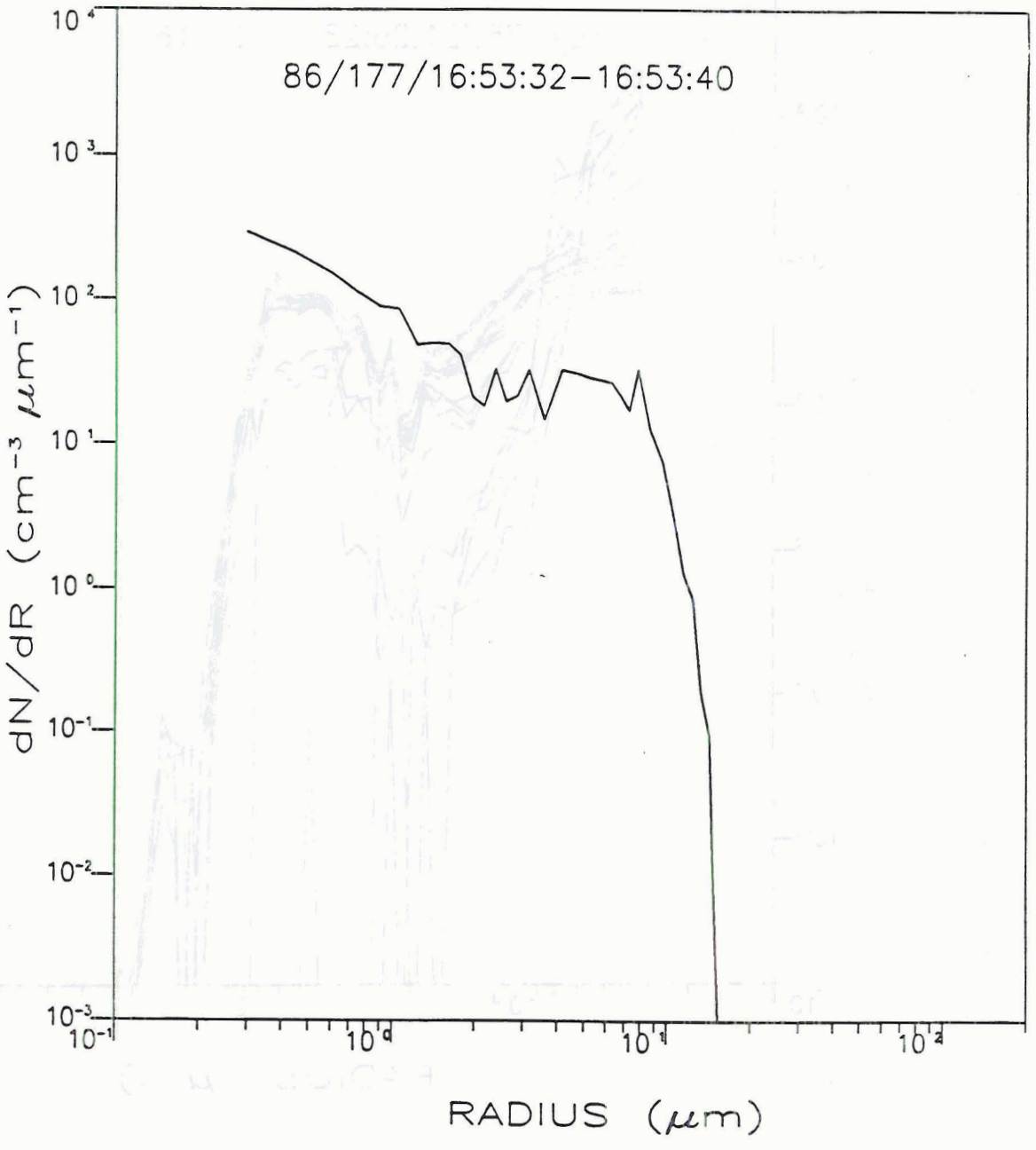


Figure 4.9: A particle size distribution sampled within the top of a cloud cell.

parcels during the sampling time. Significant reduction in the numbers of droplets larger than 5 $\mu$m radius while in cloud was only found in two instances, which were associated with updrafts. The presence of updrafts was inferred by sudden uncontrolled ascent of the aircraft. An example of the particle size distribution during passage through an updraft is shown by Figure 4.11. Since the sampled clouds were only 200-300 meters in depth, the small number of larger droplets may be due to the short time for condensation within the updraft parcel.

The aircraft microphysical data provided information useful in modeling the structure of marine boundary layer cloud. The droplet size distribution is relatively narrow, and values of the droplet effective radius for constant-altitude flight segments increased from approximately 4 $\mu$m to 6 $\mu$m between cloud base and cloud top. Aerosol exists in significant concentrations (200–500 $cm^{-3}$) below cloud and in a narrower layer between cloud top and the boundary layer inversion. Liquid water contents were small (less than 0.2 g $m^{-3}$ in all but one flight segment) in the clouds sampled.

### 4.2.2 Radiometric data

The Eppley Precision Spectral Pyranometers (PSP) and CI Spectral Radiometer (SR) were utilized to obtain experimental measurements of the broadband flux and spectral radiance of the cloud layers. These measurements were designed to provide information on the spatial variability of the radiation components, and to offer comparison of measured spectral radiance to the results of the modeling of cloud radiance in relation to the estimation of droplet size. The horizontal variability of irradiance components and upward radiance for individual filters is shown by time plots of the PSP and SR signals (Figure 4.12 and Figure 4.13). For a plot extending one minute, the horizontal distance traveled by the aircraft is 3.2 kilometers. For a sampling rate of 0.1 second, the distance between sampling points is 5.4 meters, but the time constant of the PSP is one second. The spatial variability of the 1.6-$\mu$m signal appears in the irradiance data. The signal is better defined in the total shortwave than the near infrared.

A great deal more detail is represented in the measurements from the SR, which has a narrow field of view, than from the domed pyranometers. This is due somewhat to

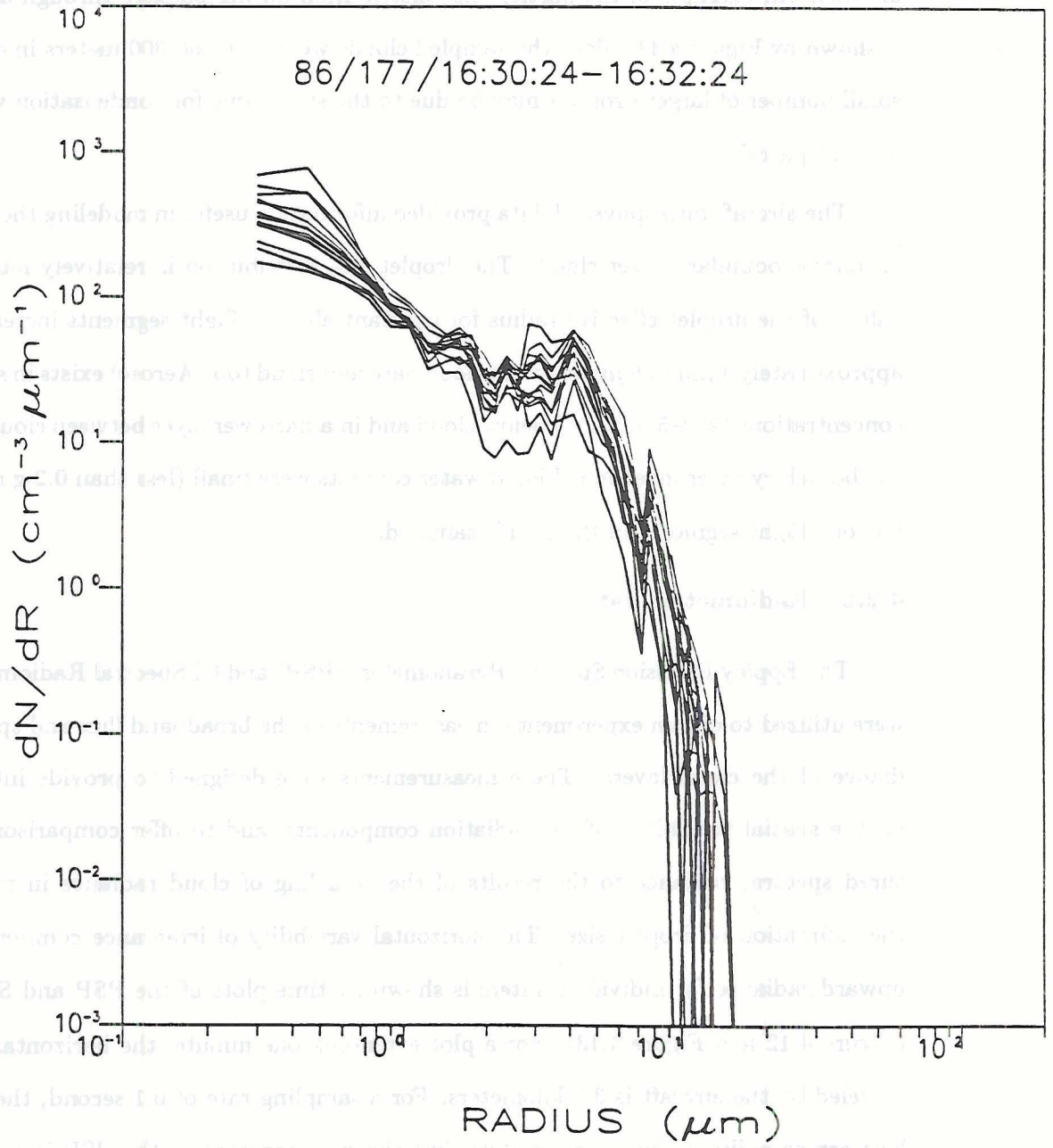


**Figure 4.10: A particle size distribution sampled along a flight track in cloud.**

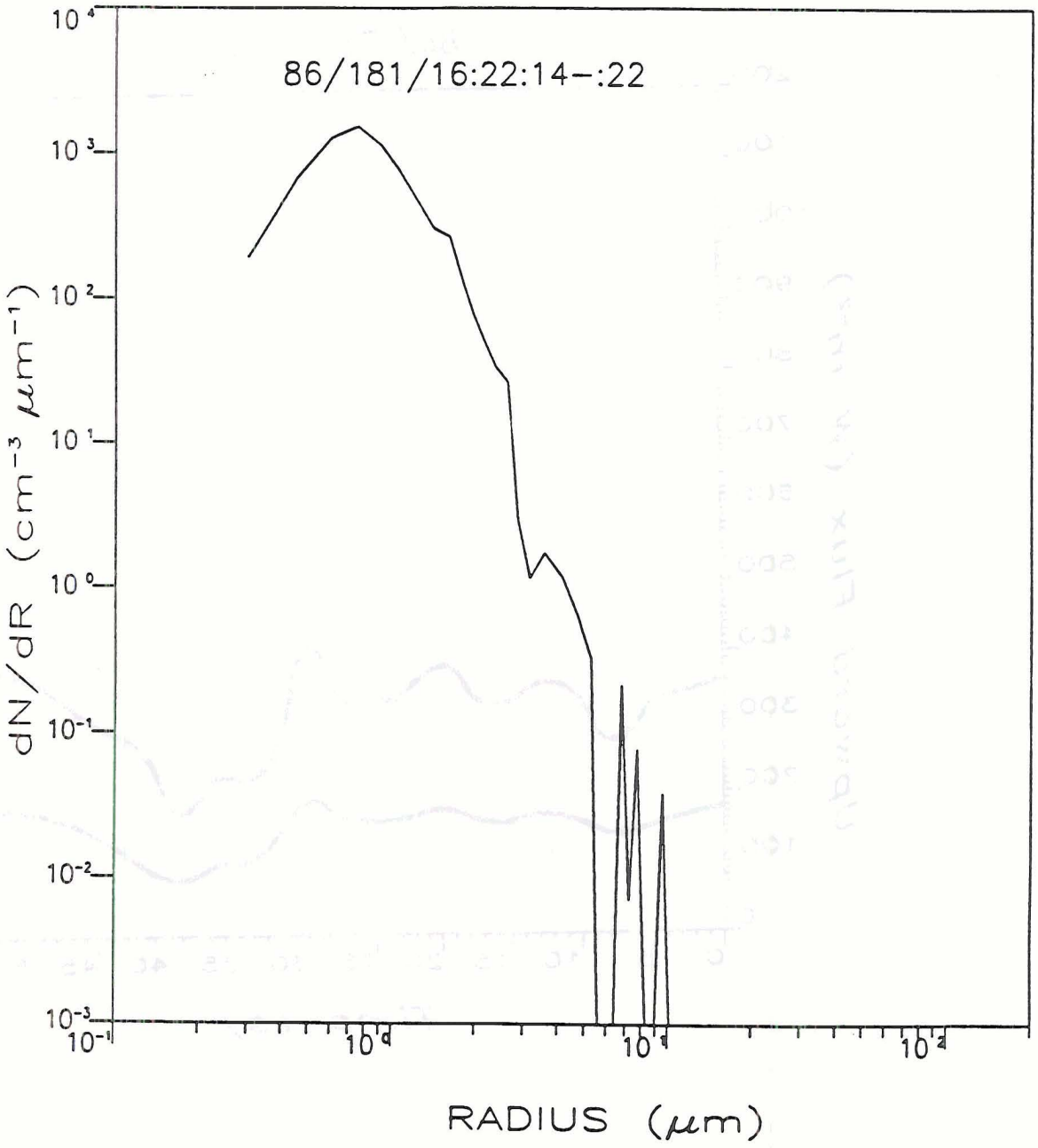


Figure 4.11: A particle size distribution sampled during passage through an updraft.

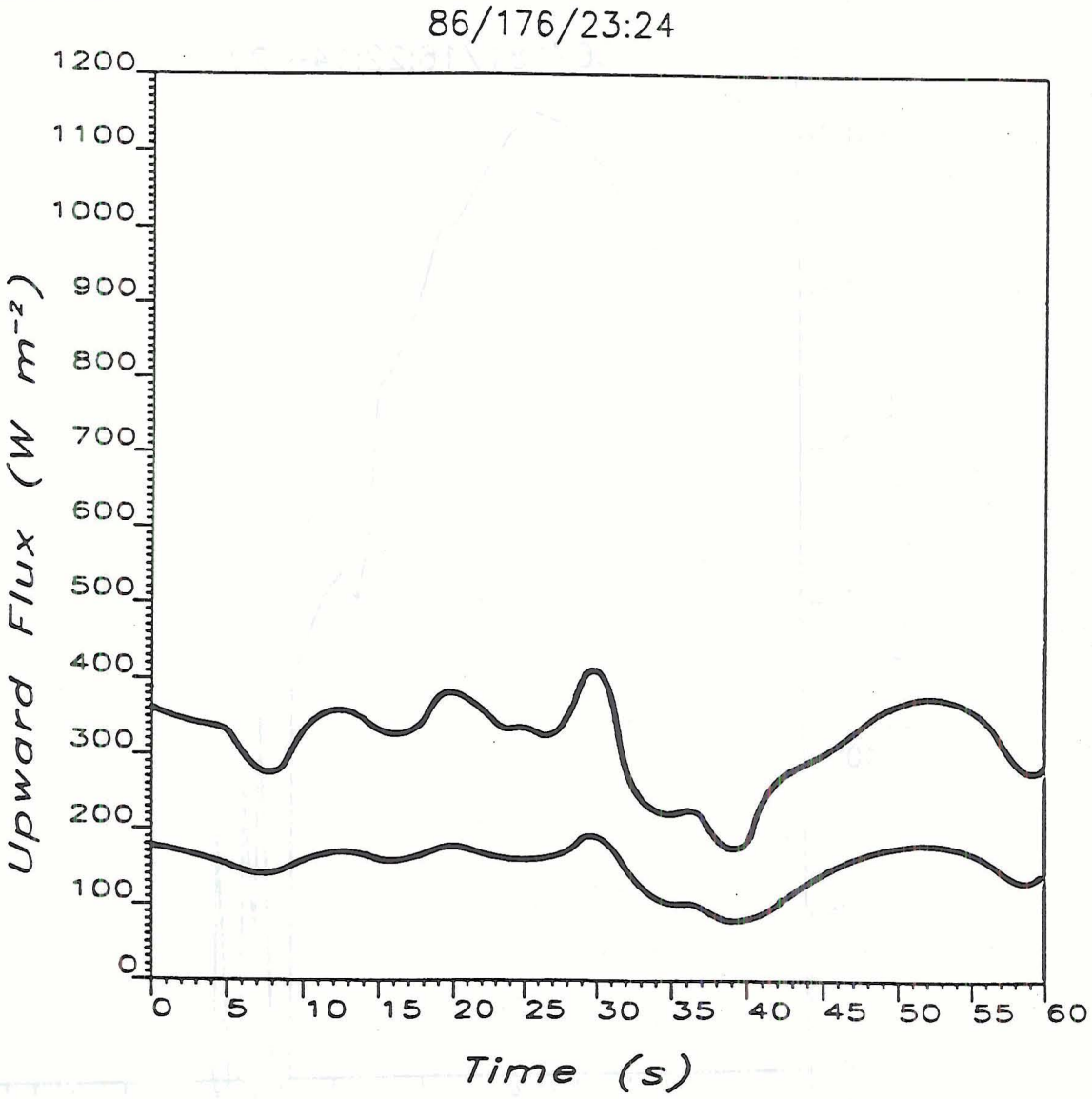


Figure 4.12: Time sequence of upward irradiance measurements. The upper curve represents the total shortwave values, and the lower curve represents the near-infrared values.

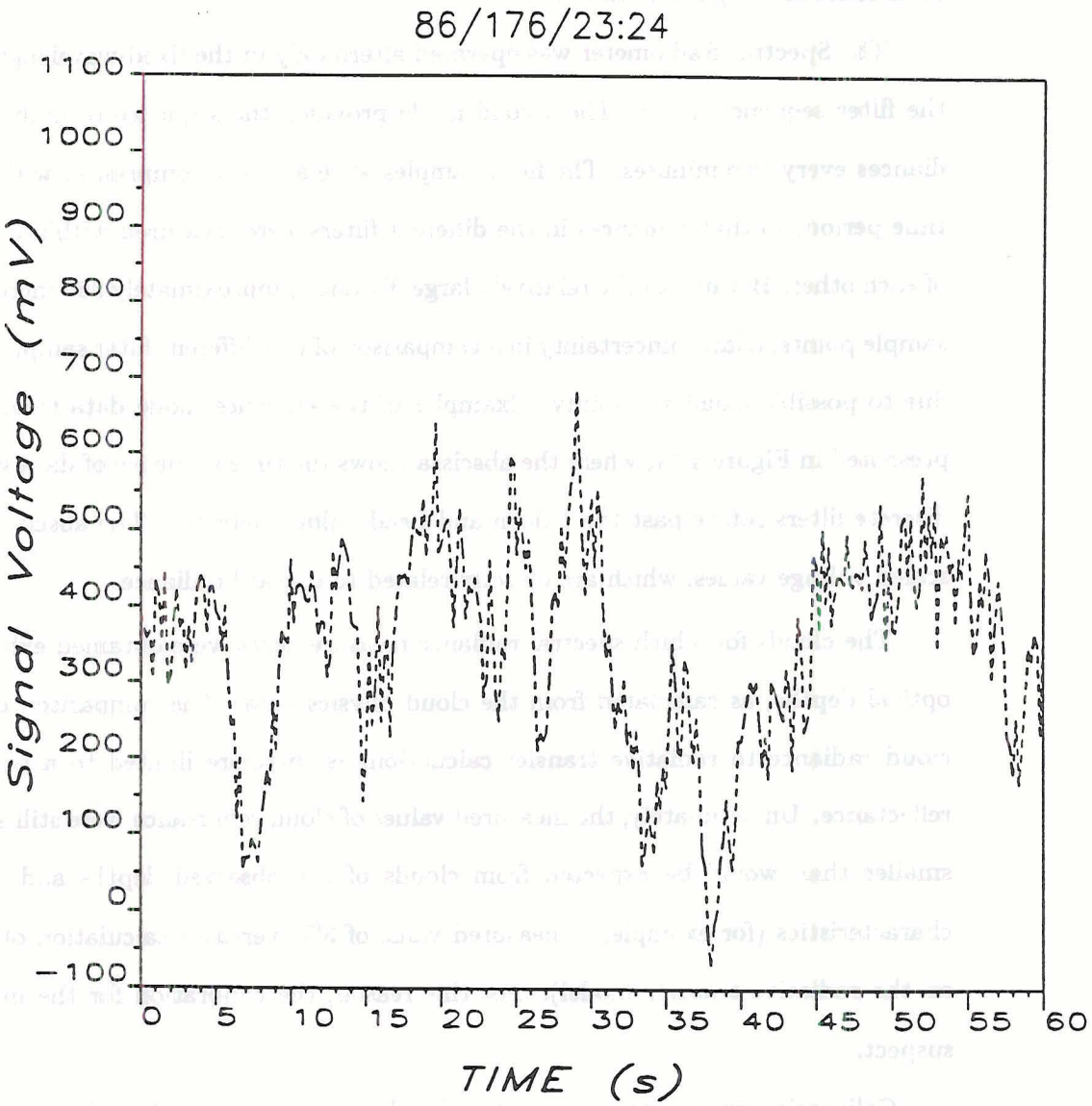


Figure 4.13: Time sequence of Spectral Radiometer data for the 1.6-$\mu$m wavelength.

noise inherent in the 1.6-$\mu$m Lead Sulfide detector, but the PSP signal is also considerably affected by the hemispheric field of view. The SR field of view is only six milliradians, allowing cloud edges which create shadow and breaks to be easily detected. The time sequences of the filters centered at 0.65 $\mu$m and 0.85 $\mu$m also correspond directly to the total shortwave signature above cloud.

The Spectral Radiometer was operated alternately in the fixed-wavelength mode and the filter sequence mode. The second mode provided the sequence of multiple-filter radiances every two minutes. The filter samples were actually compressed within a shorter time period, so that radiances in the different filters were measured within a few seconds of each other. Because of the relatively large distance (approximately 300 meters) between sample points, a large uncertainty in a comparison of the different filter samples is incurred due to possible cloud variability. Examples of the sequence mode data from the SR are presented in Figure 4.14, where the abscissa shows the time sequence of data values as the discrete filters rotate past the Silicon and Lead Sulfide detector. The abscissa represents scaled voltage values, which are directly related to upward radiance.

The clouds for which spectral radiance measurements were obtained exhibited small optical depths, as calculated from the cloud physics data. The comparison of measured cloud radiance to radiative transfer calcuations is therefore limited to a regime of low reflectance. Unfortunately, the measured values of cloud reflectance were still significantly smaller than would be expected from clouds of the observed depths and droplet size characteristics (for example, a measured value of 3%, versus a calculation of 20% based on the radiative transfer model). For this reason, the calibration for the instrument is suspect.

Calibration procedures were undertaken both prior to and after the field study. The follow-up calibration did not take place until several months following the field work, so preference is given to those results obtained from the initial calibration. The initial procedure supplied only an estimate of a calibration constant for the two 1.6 $\mu$m filters, due to the output wavelength limitation of the standard radiance lamp which was employed.

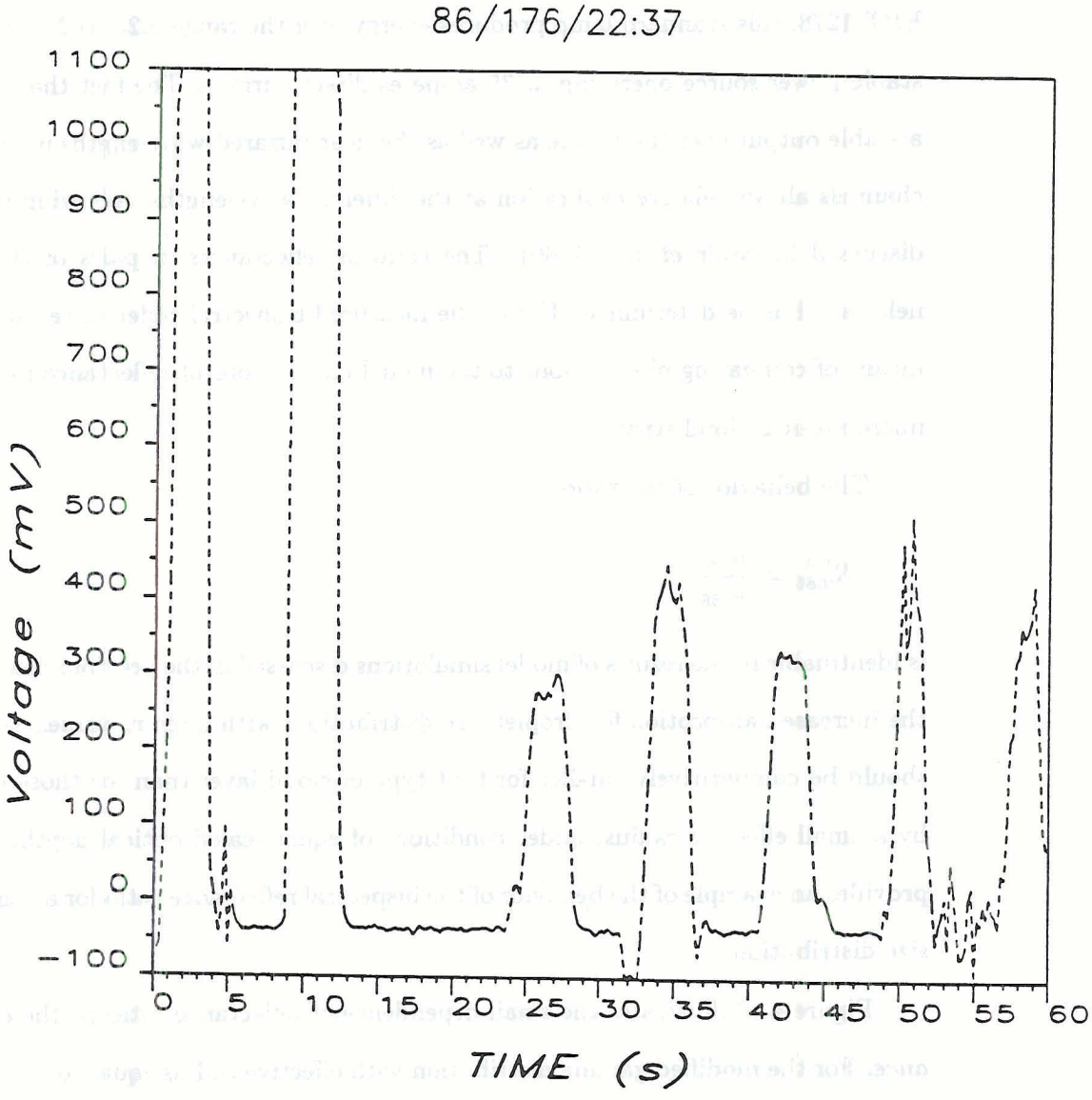


Figure 4.14: Recorded signal of upwelling radiance detected by the Spectral Radiometer.

During the calibration procedure, the optical configuration of the lamp and instrument setup may have caused improper signal measurements. There was discrepancy between calibration constants obtained using two different standard lamps requiring different optical configurations. However, the relative calibration between the filter channels is expected to be correct for the calibration performed with the Eppley tungsten filament lamp EPT-1278, this standard lamp produces energy over the range 0.25 to 2.6 $\mu$m with a very stable power source operating at 35 amperes direct current. The fact that this lamp has a stable output over the visible as well as the near-infrared wavelengths used for the filter channels allows relative calibration at the different wavelengths, following the procedure discussed by Stair *et al.* (1960). The ratio of reflectances in pairs of the filter channels can thus be determined. Use of the measured bispectral reflectance ratio provided a means of comparing observations to the model calculations of reflectance for the sampled microphysical cloud structure.

The behavior of the ratio

$$R_{0.85}^{1.6} = \frac{\rho_{1.6}}{\rho_{0.85}} \tag{4.1}$$

is identifiable in the results of model simulations discussed in the previous chapters. Due to the increased absorption for droplet size distributions with large $r_e$ values, the ratio $R_{0.85}^{1.6}$ should be comparitively smaller for that type of cloud layer than for those characterized by a small effective radius, under conditions of equal scaled optical depth. Figure 4.15, provides an example of the behavior of the bispectral reflectance ratio for a range of droplet size distributions.

Figure 4.16 illustrates the small dependence of reflectance ratio on the effective *variance*. For the modified gamma distribution with effective radius equal to 10 $\mu$m, the value of the reflectance ratio is 0.02 larger for an effective variance of 0.3 than for an effective variance of 0.1. This condition holds throughout the wide range of scaled optical depth displayed in the Figure. This magnitude of variation is similar to that caused by changing the effective radius value by 1 $\mu$m, as shown in Figure 4.15.

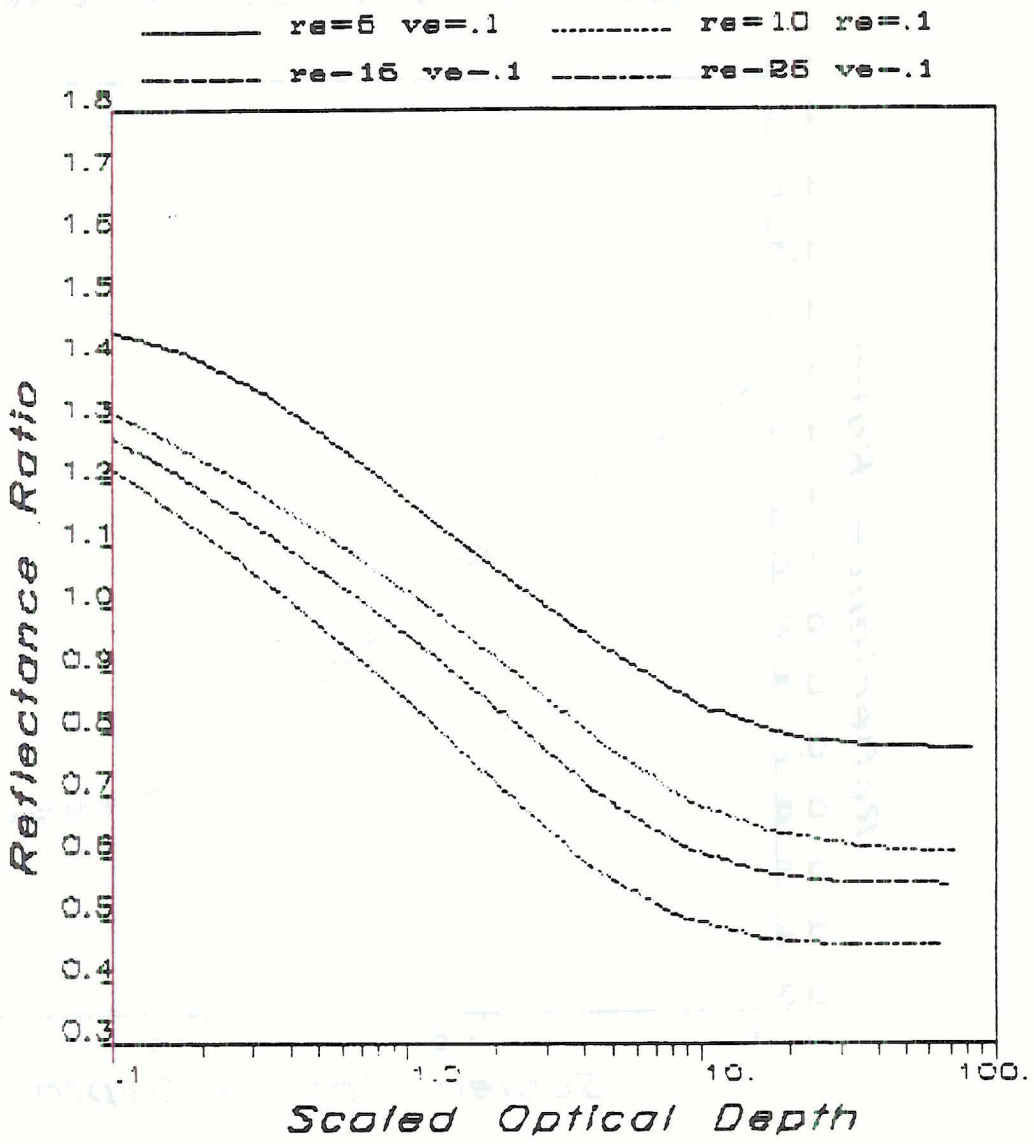


Figure 4.15: Ratio of cloud reflectances at 0.85 $\mu$m and 1.6 $\mu$m for differing effective radius.

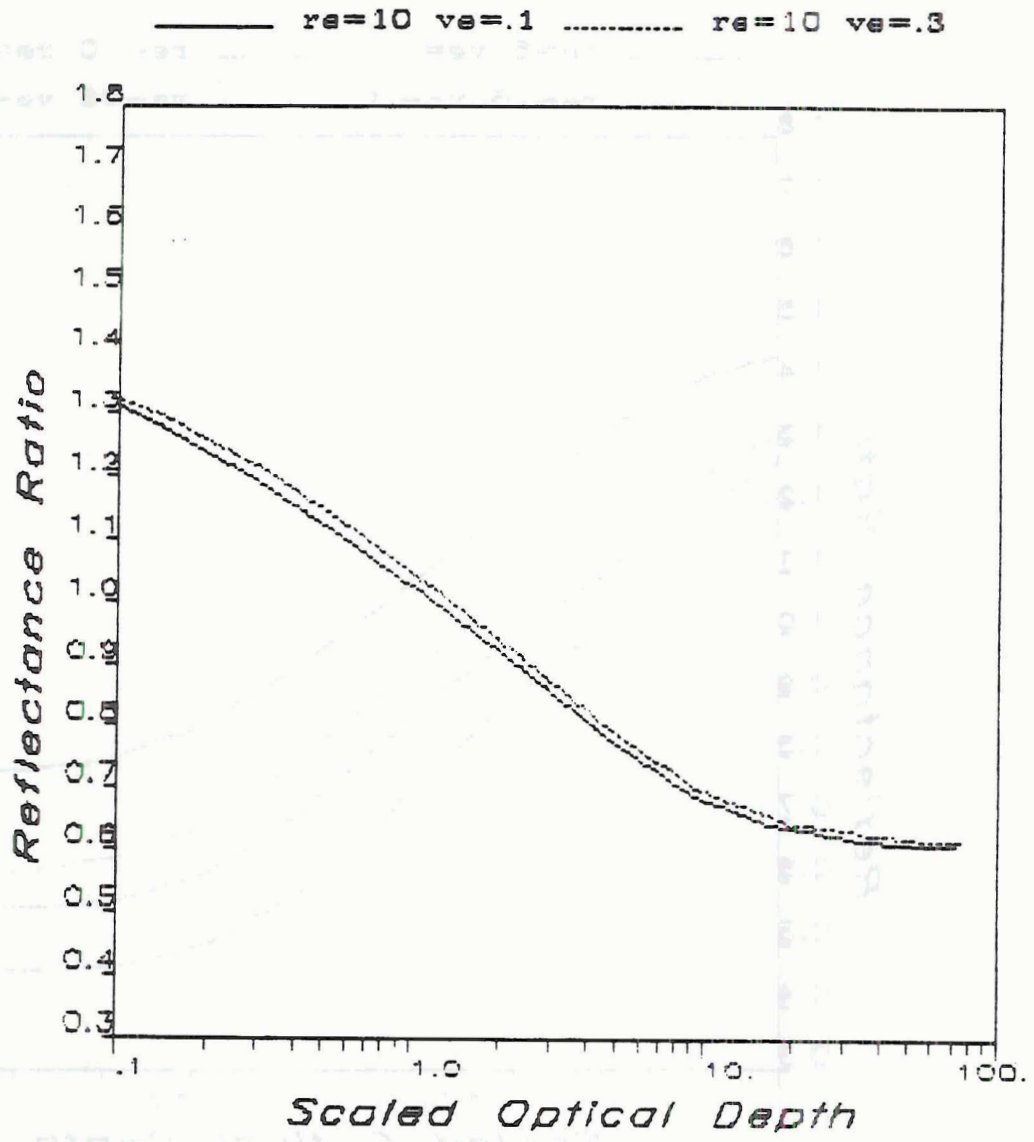


Figure 4.16: Ratio of cloud reflectances at 0.85 $\mu$m and 1.6 $\mu$m for differing effective variance.

Table 4.5 lists the ratios of 1.6-$\mu$m to 0.85-$\mu$m spectral reflectances calculated from Spectral Radiometer measurements in the present study, which were taken at various altitudes above cloud top during the aircraft horizontal sampling passes.

Table 4.5: Measured reflectance ratios.

| *Label* | $Z$ (m) | *Description* | $R_{0.85}^{1.6}$ |
|---|---|---|---|
| 175 | 549 | Above haze & St | 0.89 |
| | 549 | Above haze & St | 0.95 |
| | 549 | Above haze & St | 0.60 |
| | 518 | Above St | 0.61 |
| 176 | 1341 | Thin St below | 0.82 |
| | 1280 | Continuous thicker St | 0.56 |
| | 427 | Skimming tops | 0.77 |
| | 762 | Patchy | 0.53 |
| 177A | 549 | Above haze & St | 0.69 |
| | 518 | In haze, above St | 0.77 |
| | 457 | Cloud top | 0.67 |
| 177B | 488 | In haze, above St | 0.86 |

These values are consistently less than one. The aircraft sampling of the cloud layers themselves allowed the scaled optical depths to be estimated. These values ranged from 0.4 to 0.9. Thus, the measured $R_{0.85}^{1.6}$ values were found to be significantly smaller than model simulations of the cloud layer would provide. Relatively more extinction was indicated at the longer wavelength than predicted from the numerical model, but this could have been due to the non-coincident sampling of cloud in the two spectral bands. Secondly, the relationship between scaled optical depth and the 0.85-$\mu$m reflectance is not constant for cloud optical depths less than 4, as shown in Chapter 2. The optical depths estimated for the sampled cloud layers were 3.6 to 4.7. It was hoped that clouds of larger optical depth would have been encountered during the experimental program. The Australian program offered the opportunity to utilize the microphysics and spectral reflectance data from stratocumulus of somewhat larger optical depths. These data also provided higher spatial resolution and coincident multispectral reflectance information.

### 4.3 Analysis of data from Australian experiment

Results from three of the flights during the Australian measurement program have been used to investigate the droplet size retrieval method in stratocumulus. These cloud layers were characterized by an increase in droplet size and liquid water content toward cloud top, with maximum values of 15 $\mu$m for the droplet effective radius and 0.55 g m$^{-3}$ liquid water content. Figure 4.17 compares model reflectance for a group of DSD's with results of Stephens and Platt (1987) (SP). Their calculated values of 1.6-$\mu$m reflectance were obtained from detailed multi-layer representations for the three stratocumulus cloud decks, including gaseous absorption which may have minor effects in the chosen spectral bands. The SP model results are shown as asterisks with our model curves for gamma size distributions. This suggests that the SP model results are very close to those for a homogenous layer with the analytical size distributions of droplet effective radius in the range 10–15 $\mu$m, and that this droplet size range represents the reflectance characteristics of the SP cases well. Mean values of effective radii for in-cloud samples at cloud top level were 9.9, 11.8, and 13.8 $\mu$m for the SP cases designated as SC01, SC03, and SC04, respectively. The first case occurred over land, while the second and third case were of stratocumulus over the ocean.

The values of reflectance measured averaged across the above-cloud sampling pass over these clouds was much less than the model values. Compare the values of 1.6-$\mu$m reflectance shown by the crosses (0.19, 0.29, and 0.35) with the calculated reflectances shown by the asterisks (0.23, 0.42, and 0.46). The measured values fall near our AD model curves for the size distributions of effective radius 25-30 $\mu$m. The lower measured reflectances would imply a larger effective radius for the cloud, which neither the SP model nor the AD model have predicted. In these case studies, the measured ratio of reflectances was less than unity, while the SP model produced results which predict the ratio to be equal to 1.08 and 1.21 for the two cases of small optical thickness ($\delta$ = 6 and 5, respectively). The model results for the thicker cloud ($\delta$ = 10) predicted a ratio equal to 0.85, while the measured ratio was again considerably less (0.65). Actually, the central wavelengths of the sampled filter bands for the Australian study are different (0.842 and

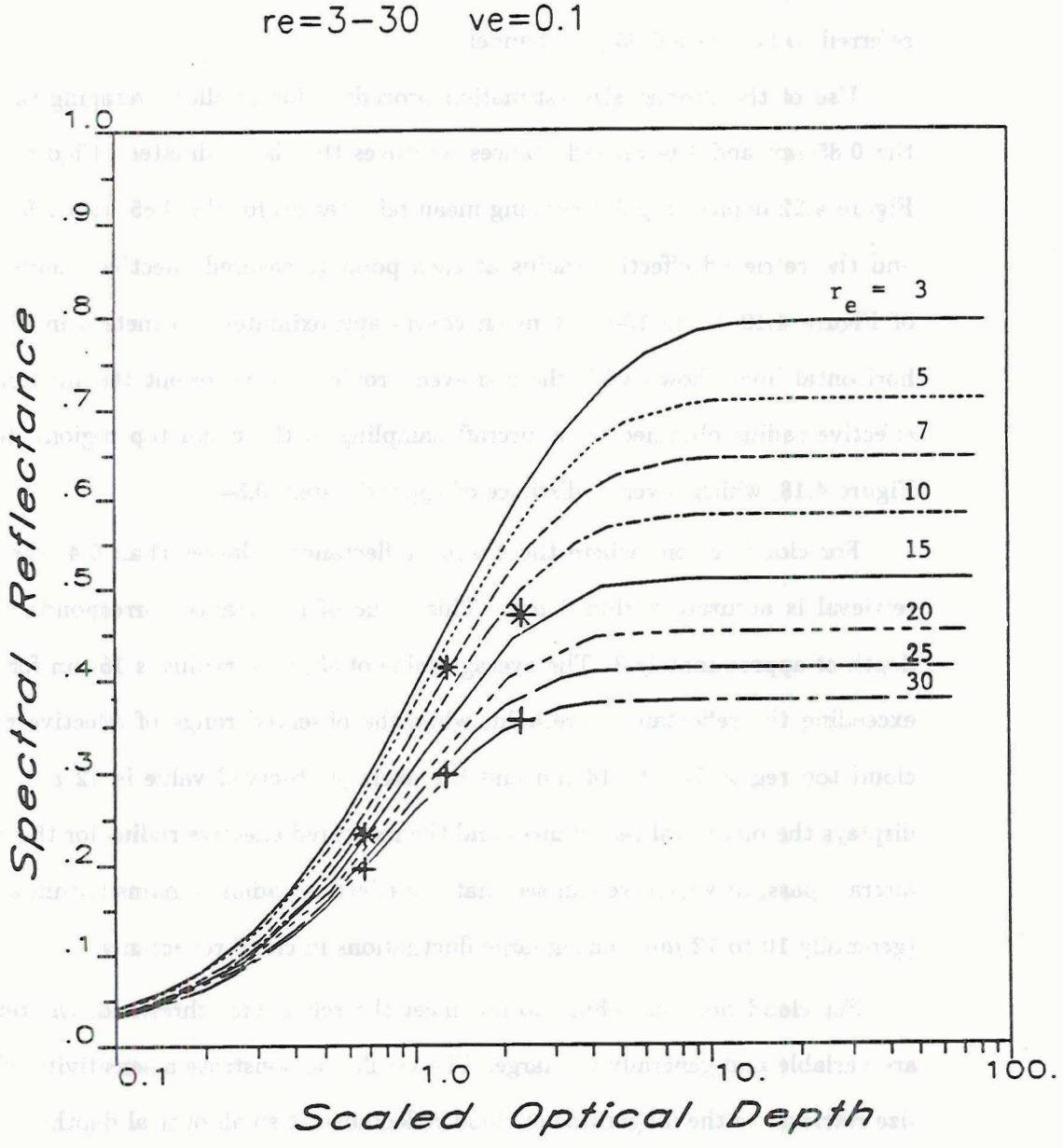


Figure 4.17: 1.6-$\mu$m nadir reflectances. Curves are adding model results from this study for gamma droplet size distributions. Asterisks are the Stephens and Platt model results based on observed cloud microphysics. Crosses are obtained from their reflectance measurements at cloud top.

1.635 $\mu$m) than those utilized for the California experiment (0.851 and 1.644 $\mu$m), but the asymmetry parameter, scattering coefficient, and absorption coefficient have insignificant variation within the intervals described by these variations (Irvine and Pollack, 1968; Hale and Querry, 1973; Davies *al.*, 1984). The SPERAD channel centered on 0.842 $\mu$m will be referred to here as a 0.85-$\mu$m channel.

Use of the droplet size estimation procedure for smaller averaging sample sizes of the 0.85-$\mu$m and 1.6-$\mu$m reflectances improves the size estimates. Figure 4.18 through Figure 4.22 depict 10-point running mean reflectances for the 0.85- and 1.6-$\mu$m channels, and the retrieved effective radius at each point (measured effective radius, in the case of Figure 4.19. The 10-point mean covers approximately 80 meters in distance. The horizontal lines shown with the retrieved droplet size represent the measured range in effective radius obtained from aircraft sampling in the cloud top region. Refer first to Figure 4.18, which covers a distance of approximately 0.54 km.

For cloud regions where the 1.6-$\mu$m reflectance is larger than 0.4, the droplet size retrieval is accurate within 3 $\mu$m. This value of reflectance corresponds to an optical depth of approximately 8. The average value of effective radius is 15 $\mu$m for the samples exceeding the reflectance threshold, while the observed range of effective radius in the cloud top region is 9 to 14 $\mu$m and the average observed value is 12 $\mu$m. Figure 4.19 displays the bispectral reflectances and the measured effective radius for the first in-cloud aircraft pass, in which we can see that the effective radius remains within a small range (generally 10 to 12 $\mu$m) during large fluctuations in cloud reflectance.

For cloud portions which do not meet the reflectance threshold, the retrieved sizes are variable and generally too large. The results demonstrate a sensitivity of the droplet size retrieval to the magnitude of cloud reflectance at small optical depths. Most of these points have a value of 1.6-$\mu$m reflectance which is lower, or a 0.85-$\mu$m reflectance which is higher, than model clouds of the observed droplet size characteristics.

One source of disparity between droplet size measurements and the values obtained from the retrieval scheme is the variance of the droplet size distribution. The retrieval scheme utilizes the results of modeling the size distributions of effective variance 0.1 and

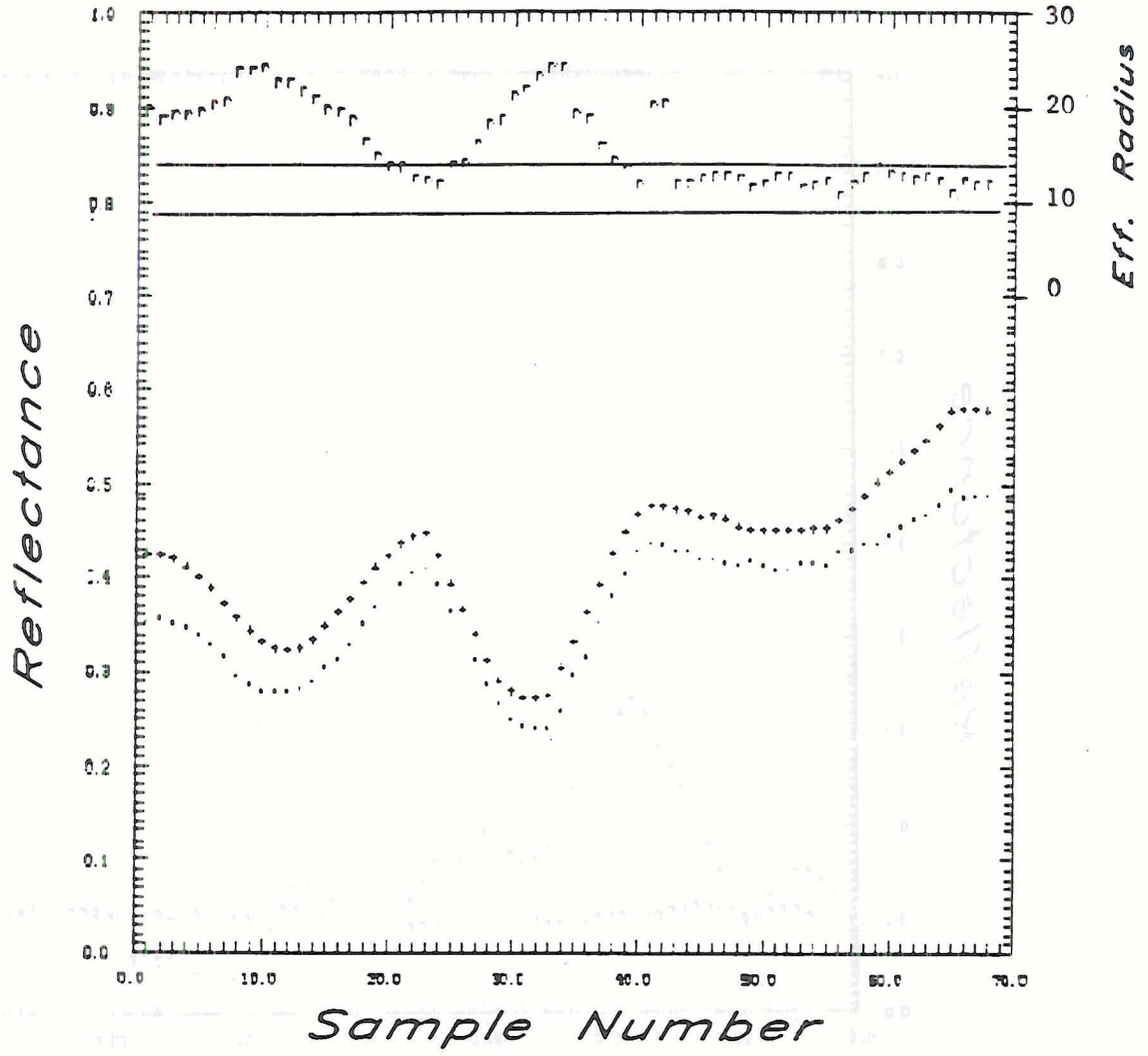


Figure 4.18: Measured reflectances at 0.85 (+) and 1.6 (.) $\mu$m and retrieved effective radius (r) from the aircraft pass directly above cloud top for case SC03.

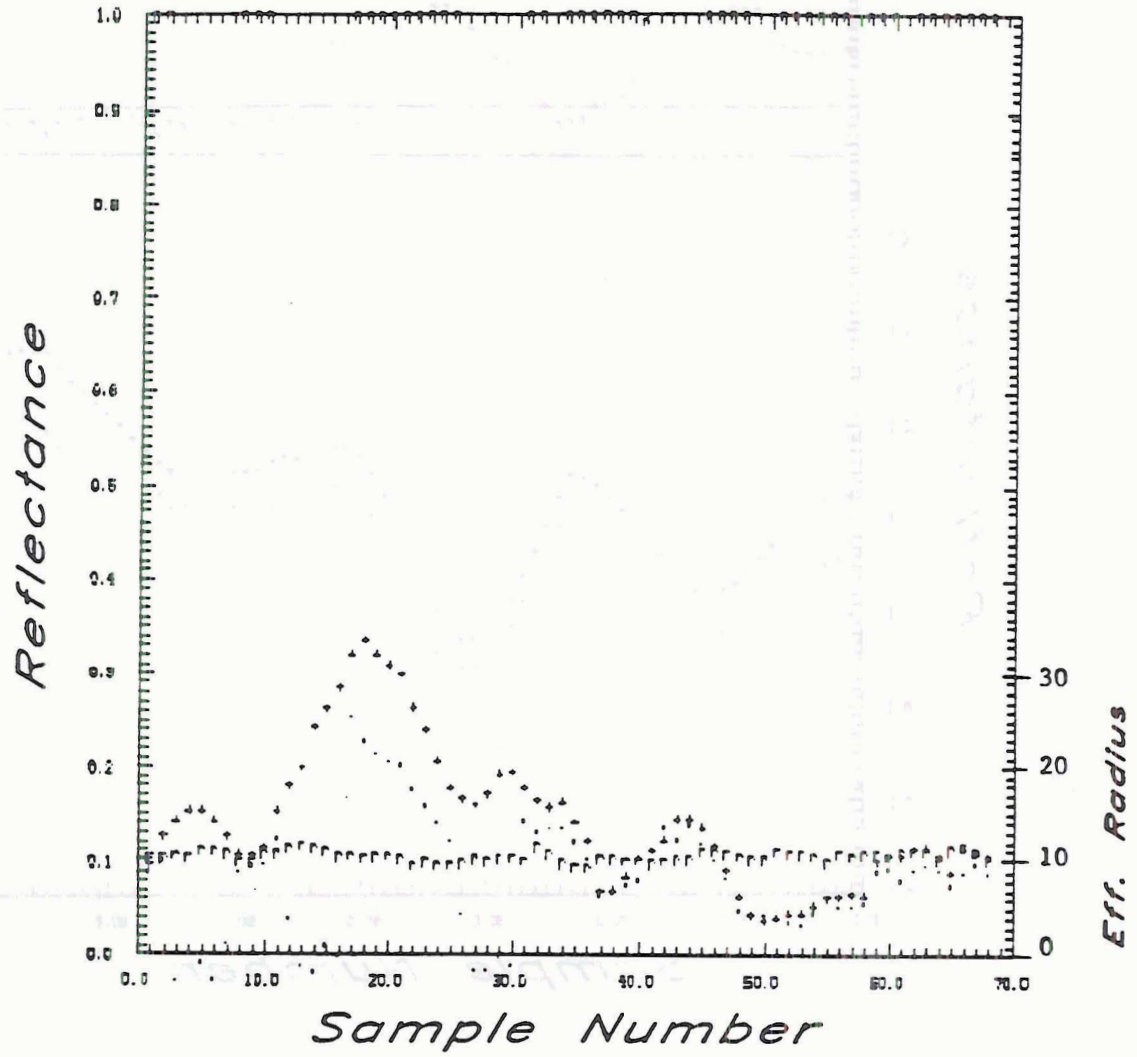


Figure 4.19: Measured reflectances at 0.85 (+) and 1.6 (.) $\mu$m and measured effective radius (r) from the aircraft pass within the cloud top region for case SC03.

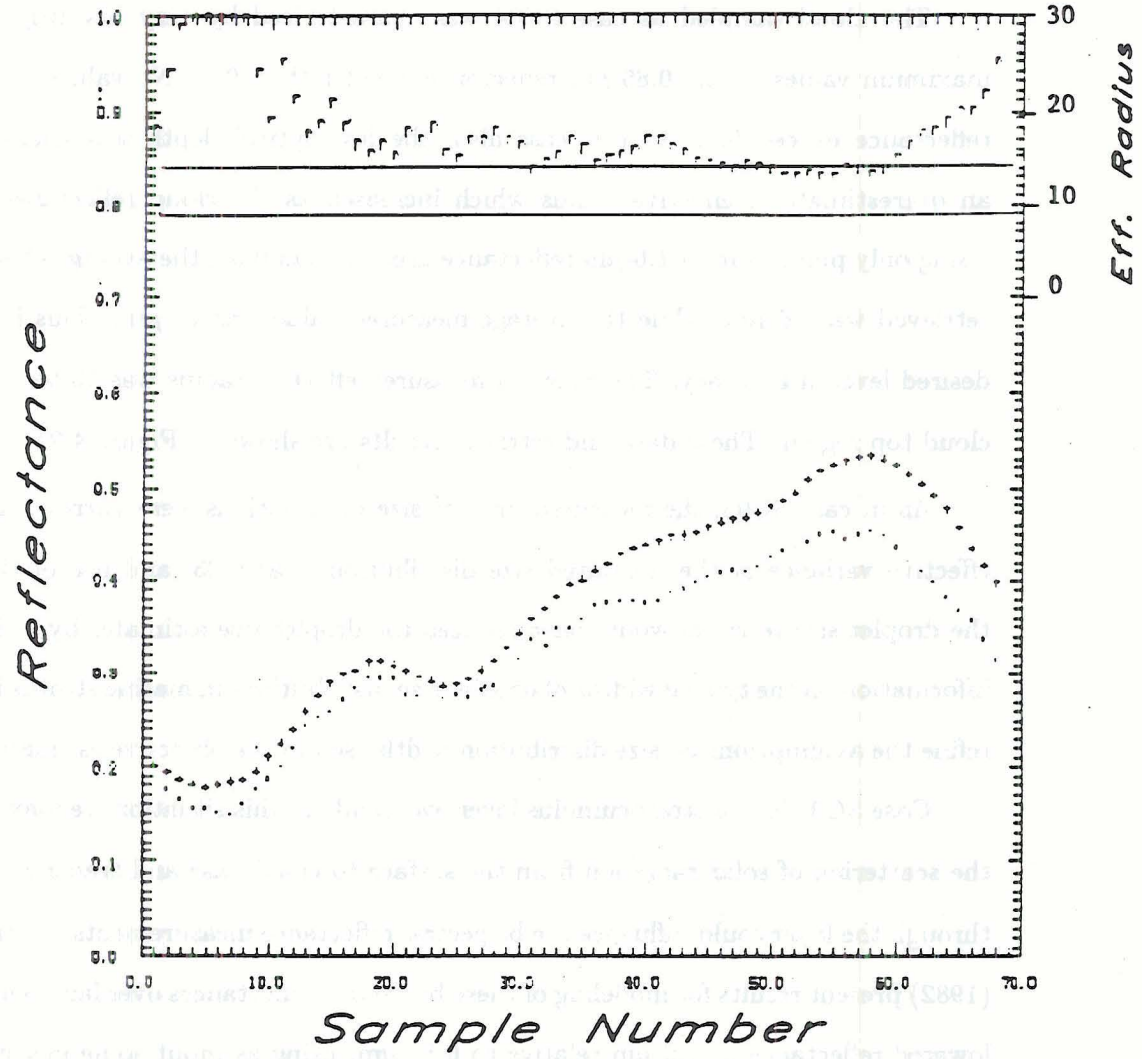


Figure 4.20: Measured reflectances at 0.85 (+) and 1.6 (.) $\mu$m and retrieved effective radius (r) from the aircraft pass directly above cloud top for case SC03.

0.3 to represent the range of most cloud distribution widths. The average of retrieved droplet sizes for the two conditions is taken, with the end result representing a droplet size distribution with an effective variance of approximately 0.2, while the average value of measured effective variance in the cloud was 0.07. Utilizing this value of effective variance improves the accuracy of the effective radius estimates by 1–2 $\mu$m.

The cloud sampled as case SC04 was characterized by very low brightness, with maximum values of the 0.85-$\mu$m reflectance smaller than 0.5. No values of the 1.6-$\mu$m reflectance exceed 0.4. In this case also, the low optical depth was characterized by an overestimate of effective radius which increased as the cloud reflectance decreased. Using only points with a 1.6-$\mu$m reflectance greater than 0.35, the average effective radius retrieved was 16 $\mu$m, while the average measured value was 14 $\mu$m. This is within our desired level of accuracy. The range of measured effective radius was 13 to 15 $\mu$m in the cloud top region. These data and retrieval results are shown in Figure 4.21.

As in case SC03, the measured droplet size distributions were narrow. The average effective variance of the measured size distributions was 0.03, and use of this value in the droplet size retrieval would have reduced the droplet size estimates by 2–3 $\mu$m. More information on the typical widths of droplet size distributions in marine stratus is needed to refine the assumptions on size distribution width used in the objective estimation method.

Case SC01 is of a stratocumulus layer over land. In this situation we may expect that the scattering of solar radiation from the surface to cloud base and transmission upward through the layer could influence the bispectral reflectance measurements. Curran and Wu (1982) present results for modeling of these bispectral reflectances over land which indicate lowered reflectance at 1.6 $\mu$m relative to 0.85 $\mu$m, using as input some measurements of spectral ground albedo obtained from high-flying aircraft. Apparent ground albedo is due both to surface characteristics and intervening atmospheric effects. The results of modeling a haze layer below cloud, described in Chapter 3, demonstrate that spectral dependence of the radiance boundary conditions at cloud base can strongly influence droplet size estimates for optically thin cloud. Surface spectral albedo variations can act in the same way. Although we do not have information on spectral ground reflectance or

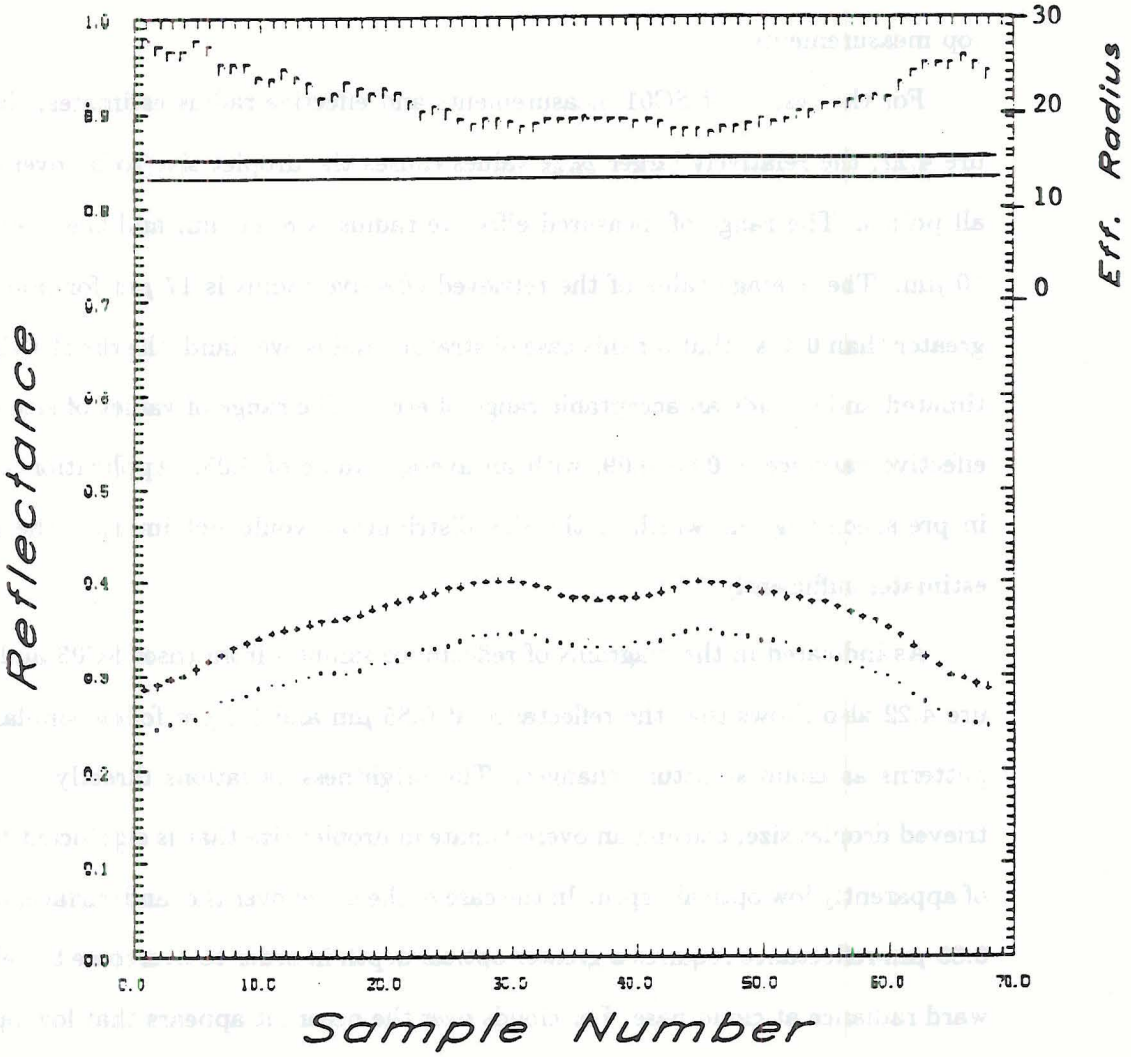


Figure 4.21: Measured reflectances at 0.85 (+) and 1.6 (.) $\mu$m and retrieved effective radius (r) from cloud top for case SC04.

the aerosol concentrations below cloud in the Australian measurements, we can see from the bispectral reflectance values at different levels at cloud base and within cloud that there is a relatively larger upward radiance at cloud base at 0.85 $\mu$m (reflectance 0.14) compared to 1.6 $\mu$m (reflectance 0.07) in the SC01 case, than in the cases of cloud over the ocean. For SC03, $\rho_{0.85} = 0.02$ and $\rho_{1.6} = 0.03$, and for SC04, $\rho_{0.85} = 0.04$ and $\rho_{1.6} = 0.04$. The enhanced 0.85-$\mu$m brightness is maintained throughout the cloud and in the cloud top measurements.

For the results of SC01 measurements and effective radius estimates, shown in Figure 4.22, the relatively larger $\rho_{0.85}$ values causes the droplet size to be overestimated at all points. The range of measured effective radius is 8–11 $\mu$m, and the average value is 10 $\mu$m. The average value of the retrieved effective radius is 17 $\mu$m for points with $\rho_{1.6}$ greater than 0.4, so that for this case of stratocumulus over land, the droplet size is overestimated and outside an acceptable range of error. The range of values of size distribution effective variance is 0.03–0.09, with an average value of 0.05. Application of this value in pre-specifying the width of the size distribution would not improve the droplet size estimates sufficiently.

As indicated in the diagrams of reflectance samples from cases SC03 and SC04, Figure 4.22 also shows that the reflectance at 0.85 $\mu$m and 1.6 $\mu$m follow similar horizontal patterns as cloud structure changes. The brightness variations directly impact the retrieved droplet size, causing an overestimate in droplet size that is significant for locations of apparently low optical depth. In the case of the cloud over the land surface, an enhanced 0.85-$\mu$m reflectance requires a greater optical depth in order to overcome the effects of upward radiance at cloud base. For clouds over the ocean, it appears that low optical depth does not provide sufficient absorption at 1.6 $\mu$m to permit accurate size discrimination. This parallels the results of Chapters 2 and 3, in which cloud structure variations and uncertainties in the cloud spectral reflectance compared to the idealized model results would require cloud optical depths to be in the range 4–8 as a minimum. This finding is relevant both to our ability to sample clouds with the relatively wide field of view required from present satellite technology. The portion of the sampled clouds which met this optical

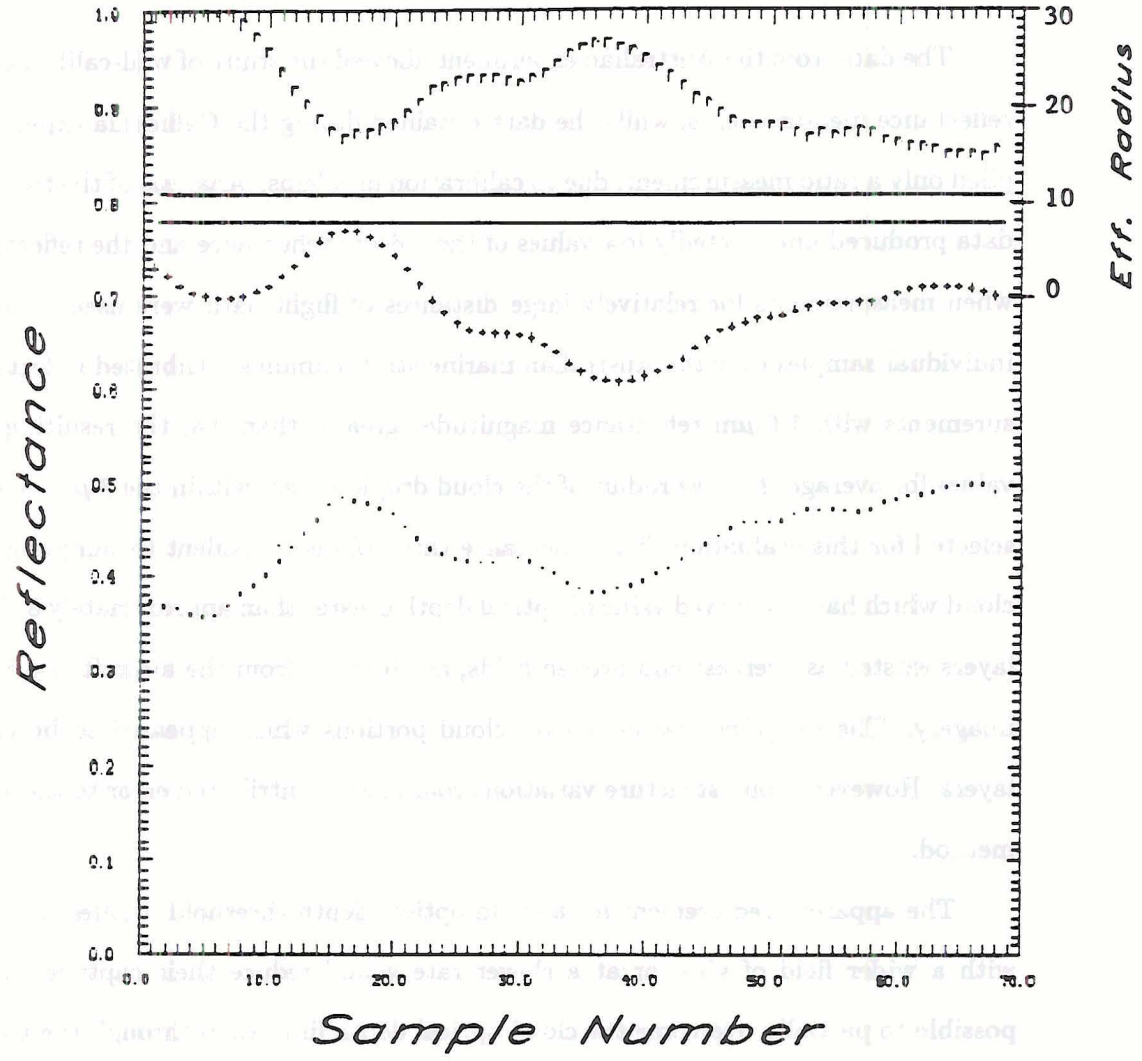


Figure 4.22: Measured reflectances at 0.85 (+) and 1.6 (.) $\mu$m and retrieved effective radius (r) from case SC01.

depth limitation was relatively small. In the case SC03, the number of points meeting the 1.6-$\mu$m reflectance threshold of 0.4 was 24 % of the total samples obtained above cloud top.

## 4.4 Summary

The data from the Australian experiment allowed the study of well-calibrated spectral reflectance measurements, while the data obtained during the California experiment supplied only a ratio measurement, due to calibration problems. Analysis of the two sources of data produced unexpectedly low values of the 1.6-$\mu$m reflectance and the reflectance ratio when measurements for relatively large distances of flight path were used. However, for individual samples over the Australian marine stratocumulus, calibrated reflectance measurements with 1.6-$\mu$m reflectance magnitudes greater than 0.4, the resulting retrieved values for average effective radius of the cloud droplets were within the 3 $\mu$m error margin selected for this evaluation. The reflectance threshold is equivalent to sampling only over cloud which has a retrieved value of optical depth greater than approximately 8. The cloud layers existed as overcast and broken fields, as observed from the aircraft and in satellite imagery. The sampling was done over cloud portions which appeared to be continuous layers. However, cloud structure variations could have contributed error to the estimation method.

The apparent requirement for a cloud optical depth threshold implies that sampling with a wider field of view or at a slower rate would reduce their capture. It may be possible to partially overcome the cloud optical depth limitation through the use of other wavelength bands to further distinguish size-specific reflectance characteristics. Some limitation due to optical depth will remain, however. Secondly, improvements in the basic assumptions on spectral extinction processes may be possible, such that the apparent cloud-scale variability in the relative magnitudes of reflectance at 0.85 and 1.6 $\mu$m is accounted for. These prospects are described in the following Chapter.

## Chapter 5

# CONCLUDING DISCUSSION

In this study, numerical experiments have been conducted on the spectral reflectance characteristics of marine stratiform cloud, based on *in situ* measurements of cloud and aerosol physical properties and other published data, and analysis of cloud reflectances and the values of effective radius derived from the reflectance data has been carried out. The primary conclusions obtained from the field work, theoretical studies and analysis are briefly listed below, and are followed by a more complete discussion in the next sections.

(1) The 1.6-$\mu$m spectral cloud bidirectional reflectance has been shown to allow segregation of cloud droplet effective radius for a given scaled optical depth.

(2) The 0.85-$\mu$m spectral reflectance has been used to determine cloud layer scaled optical depth, due to the observed independance of this optical depth parameter to droplet size distribution.

(3) An objective retrieval technique has been developed for estimation of droplet effective radius from the bispectral (0.85-$\mu$m and 1.6-$\mu$m) reflectance measurements above cloud top.

(4) An uncertainty of 3 $\mu$m in the retrieved effective radius is determined to be within acceptable accuracy for the potential applications of droplet size estimates obtained from remote sensing.

(5) The minimum cloud 0.85-$\mu$m optical depth for which the retrieval technique provides accurate droplet size retrievals is identified as approximately four.

(6) The measurement error for cloud spectral reflectance was shown to be required as 3 % or less to insure accurate droplet size estimates.

(7) The retrieval procedure should use model solutions with solar zenith angle increments of one degree or better, to avoid errors due to the variation of reflectance with solar angle.

(8) Droplet size retrieval errors due to cloud structure inhomogeneity was modeled, including broken cloud, the presence of aerosol, and vertical layering within cloud. The results indicated little sensitivity except in the case of haze below optically thin cloud. In this case, the cloud optical depth had to be at least seven to allow accurate droplet size estimates.

(9) Comparisons of field microphysical measurements to the droplet size estimates derived from coincident bispectral reflectance measurements for a limited set of cases show that the droplet size is accurately retrieved for cloud samples with indicated optical depths greater than seven.

## 5.1 Microphysical structure of marine cloud and aerosol layers

The marine stratiform cloud layers sampled during the California field experiment described in Chapter 4 can be characterized as thin (200-300 meters in depth) and of low liquid water contents (less than 0.16 g $m^{-3}$ except in one lower-cloud measurement of 0.55 g $m^{-3}$. The mean and effective radii for the cloud droplet size distributions increased with the liquid water content from cloud base to cloud top, with typical values near cloud top of 5 $\mu$m for mean radius and 6 $\mu$m for effective radius. Droplet concentrations were in the range 150-200 $cm^{-3}$ at cloud top, and with the inclusion of aerosol sizes, particle concentrations were in the range 200-400 $cm^{-3}$. Significant concentrations of aerosol were also measured in the sub-cloud layer (up to 700 $cm^{-3}$, and in lower cloud the combination of droplet and aerosol concentrations exceeded 400 $cm^{-3}$. For one sampling period, there also existed large concentrations of aerosol (439 $cm^{-3}$) above the cloud layer. Thus, the radiative effects of aerosol had to be considered at cloud top, within cloud, and in the sub-cloud layer. The aerosol population typically had values of the effective radius equal to 0.5 $\mu$m, but including the aerosol size range in the particle distributions added less than 0.001 g $m^{-3}$) to liquid water concent estimates. Mie calculations were carried out to

determine the phase function and extinction parameters of the aerosol size distributions, using different assumptions concerning the chemical composition of the aerosol. These data were then utilized in conjunction with measured and published droplet size characteristics to simulate the upward radiance properties of cloud-aerosol models. Conclusions were drawn and compared for the model results of pure-water cloud and then water-aerosol layer simulations, as described below.

## 5.2 The influence of cloud structure on spectral reflectance

It is found from theoretically-derived relationships between the cloud particle effective radius and cloud reflectance in the water vapor window bands, that the ratio of reflectances at 1.60 and 0.85 $\mu$m is slightly greater than unity for homogeneous shallow clouds with small or moderate values of $r_e$. The ratio becomes less than unity for optically thick layers. The optical depth at which this transition occurs is largest for droplet size distributions with small $r_e$. For very large $r_e$ (*e.g.* $> 40$ $\mu$m), $R_{0.85}^{1.6} < 1$ for any cloud optical thickness. The separation of $R_{0.85}^{1.6}$ values for different types of droplet distributions improves as the layer optical depth increases. Model comparisons of the bispectral reflectance characteristics of different cloud types indicate that for isolated, plane-parallel, pure water clouds with optical depth greater than approximately 4, a 1.6-$\mu$m reflectance can be applied to estimate effective radius. It is necessary to establish the scaled optical depth of the cloud layer, which can be accomplished using 0.85-$\mu$m reflectance data, in order to retrieve the droplet size estimate.

Results of the radiative transfer calculations for vertically inhomogenous clouds in the present study show that large internal variations in the microphysical structure of the cloud layer significantly alter reflectances. Thus, an inference of effective droplet radius from reflectance relationships based on vertically homogeneous model clouds contain some error. The plane-parallel simulations obtained with the adding model show that the topmost layer of cloud strongly influences the upward scattered radiance from optically thin clouds. The presence of a cloud-top layer having a large effective radius, in a cloud otherwise charcterized by small effective radius, decreases reflectance more at the 1.6 $\mu$m

wavelength than at 0.85 $\mu$m, and therefore also reduces the value of the ratio of these two reflectances. The observed structure of marine stratus from our measurements and those of others, was of thin cloud layers in which the effective radius was small in magnitude and increased with height. We have used the particle size distributions taken from the cloud-top levels to numerically model cloud reflectance for the entire cloud, in order to guage the effects of these particle distributions on the magnitudes of cloud reflectance at 1.6 and 0.85 $\mu$m.

To explore other possible mechanisms for reducing the 1.6-$\mu$m reflectance with respect to 0.85-$\mu$m values, this study completed calculations representing (a) finite cloud structure, and (b) incorporation of particles other than pure water droplets into the scattering/absorbing medium. Results of the analysis of finite cloud effects suggest little loss of nadir-directed radiance for these shallow clouds. Comparable changes in reflectance occur at both the 0.85- and 1.6-$\mu$m window wavelengths. The influence of aerosol both within and vertically adjacent to the cloud layers was modeled. Use of expected conditions of aerosol optical depth above cloud top did not produce a significant decrease in $R_{0.85}^{1.6}$. Secondly, it was found that while the presence of oceanic aerosol within the cloud causes enhanced absorption at the 1.6 $\mu$m wavelength due to the presence of sea salt, an extraordinarily large concentration of this aerosol within cloud would be required to explain the measurements which have been discussed here. Refractive indices associated with other types of aerosol (*e.g.* urban and rural) are relatively constant between the 0.85 and 1.6 $\mu$m wavelengths, and use of these in model calculations was not effective in reducing the reflectance ratio. The presence of a marine haze below cloud could cause a preferential reduction in the upward reflectance from cloud top at 1.6 $\mu$m, leading to an overestimate of the effective radius at small values of cloud optical depth.

The measurements of cloud spectral reflectance and reflectance ratio for cloud-top average or intermittant sampling indicate enhanced extinction at 1.6 $\mu$m with respect to 0.85 $\mu$m. More detailed analysis of individual reflectance values at single points along the above-cloud sampling passes reveals that droplet effective radius is accurately estimated (within the preset margin of error, 3 $\mu$m) for points where cloud optical depth

is at least seven, while at other points the droplet size is generally overestimated. The values of measured 1.6-$\mu$m reflectance are generally smaller (by 2–5%) than expected from model simulations of stratus cloud with the observed droplet size. This can be attributed partly to the very narrow droplet size distributions of the sampled clouds, and perhaps to small variations in the upward radiance at cloud base due to underlying haze. A bias of a few percent may also be introduced by small variation in solar angle during the measurement period, or other uncertainties related to the instrumentation, calibration, and measurement. The necessity of obtaining reflectance values within a few percent in order to distinguish droplet size variations in shallow clouds emphasizes the importance of measurement accuracy.

In reference to other observational studies noted in Chapter 1, recall that Twomey and Cocks (1982) also found discrepancies between bidirectional reflectances obtained from model calculations and from measurements. Previous studies of hemispheric reflectance have resulted in the term "anomalous absorption", due to the unexplained low measurements of cloud shortwave reflectance (Reynolds *et al.*, 1975; Herman, 1977) . Results from recent measurement programs suggest that the unexplained extinction occurs in the near-infrared (NIR) portion of the shortwave spectrum. Hignett (1987) compared NIR and visible albedos measured over marine stratus to model estimates. In these data, the NIR albedos and the ratios of NIR to visible albedos were notably below theoretical estimates. Herman and Curry (1984) present similar results. The evidence for enhanced extinction processes in the near-infrared is widespread. Some process of extinction not fully accounted for in present multiple scattering models or cloud droplet composition may be playing a role in the results found here.

In the very recent past, other theories on potential cloud extinction processes have been put forth. Twomey (1987) has made a theoretical study of the effects on NIR fractional absorption by droplets with internal scatterers (such as bubbles, occlusions, and other refractive index inhomogeneities). His conclusion that a sizable enhancement in absorption can occur, provides another possible mechanism for anomalously low reflectance. Stephens (1986) proposes that spatial heterogeneity of cloud optical properties can reduce

reflectance values below those predicted from using spatially averaged microphysical data. The results of the present study did indeed demonstrate the importance of small-scale variability in controlling the bispectral reflectance characteristics. More extensive comparitive analysis is needed to investigate the influence of spatial heterogeneity on spectral reflectance measurements. The adding-and-doubling radiative transfer model has utility for representing variations in layer extinction processes, but horizontal variations in the distribution of particles can have a larger influence. In that case, numerical methods which efficiently treat realistic variability of the in-cloud particle distributions are required for testing the cloud parameter remote sensing techniques.

### 5.3 Potential of satellite remote sensing estimation of droplet size

The identification in this study of a relationship between measured $r_e$ values and the bispectral reflectances at 0.85 and 1.6 $\mu$m suggests that satellite data in these wavelengths will provide information on cloud droplet sizes, within noted constraints. Utilization of measurements in additional channels may improve the reliability of droplet size estimates. A study carried out since the present work began has provided an estimation method of droplet mode radius using the combined 0.75, 1.6 and 2.2 $\mu$m reflectances (Nakajima and King, 1988). As in the present work, errors in the droplet size estimates were noted for optically thin cloud (optical depth less than six).

The application of numerical models and field measurements presented here demonstrate the many factors which effect the remote sensing of cloud radiance. These factors include solar and viewing geometry, the conversion of satellite radiance data to cloud reflectance values, the non-homogeneity of cloud layers, and the presence of aerosol. Theoretical results obtained in this study show that satellite measurements of cloud upwelling radiance have the potential of providing information on expected values of the effective radius of the cloud top droplet size distribution, and the field measurements generally support these conclusions.

### 5.3.1 Satellite instrument opportunities

Three NOAA satellites with the AVHRR radiometer series K/L/M will be launched beginning in 1990, and will carry a Channel 3A for the spectral band 1.58-1.64 $\mu$m. Using the signal-to-noise ratio of 20-to-1 planned for this channel and assuming a signal quantization similar to the current AVHRR Channel 2, reflectance variations of less than 0.1 % will be observable. The simultaneous use of Channel 2 (0.84-0.87 $\mu$m band), with the same signal sensitivity, is sufficient to separate reflectance variations due to very small $r_e$ shifts (less than one micrometer), for clouds of sufficient optical depth and structural homogeneity. The value of Channel 2 reflectance can be used to estimate scaled optical depth of the cloud layer. The Channel 3A reflectances, applied in an interpolation procedure based on model results for a given sun-cloud-sensor geometry, can then provide an $r_e$ estimate. As an example, for viewing with solar zenith angle equal to 50°, model stratiform clouds with equivalent optical depths of 6 have 1.6-$\mu$m reflectance values separated by 7% for droplet size distributions with $r_e = 7$ versus $r_e = 13$ $\mu$m. Layers with drizzle-sized droplets ($r_e$ approximately 40 $\mu$m) are predicted to differ in Channel 3A reflectance by more than 10% than clouds with $r_e = 13$ $\mu$m. Thus, the satellite sensors are capable of identifying the droplet-size dependant reflectance variability predicted from the model representations. However, the cloud uniformity within the instrument field-of-view will control how well the reflectance measurements represent the droplet size distributions of the clouds observed.

The comparitive field data analysis for this study suggested that cloud structure would not be uniform within a satellite instrument field-of-view. Variability in the measured reflectances as large as several percent occurred, and were associated with local cloud structure. Spatial averaging over distances corresponding to the field-of-view of the AVHRR satellite sensor (1 km) produced better agreement between the reflectance and $r_e$ measurements than did averaging over sampling pass times of a few minutes (approximately 5 km). However, accurate retrieval of the effective radius required limiting the sampling to the cloud portions with large optical depth, which occurred during limited

portions of the flight legs at cloud top, if at all. Sampling with a field of view larger than 100 meters would likely have not sufficiently represented these points. Cloud layers with optical depth larger than six over the majority of the cloud area are thus indicated to be necessary for sampling with the larger satellite fields of view. A comprehensive summary of cloud optical depth for marine stratus layers should be undertaken prior to the availability of 1.6-$\mu$m radiance measurements from AVHRR-K/L/M.

Certain conditions of the satellite remote sensing methods, other than instrument field of view, make the observation of cloud properties from space platforms more difficult than from aircraft. These include effects of the intervening atmosphere as well as physical constraints of the orbiting platform. The uncertainties involved in estimating cloud reflectance from satellite observations of spectral radiance can be reduced through application under limited conditions. First, the ocean radiance component can be minimized by determining the scaled optical depth parameter for clouds from the water vapor window wavelengths longer than 0.6 $\mu$m, where turbidity due to plankton, sediments and other marine constituents does little to alter the ocean layer reflectance. For clouds optically thin enough to allow a direct solar beam transmittance to the ocean surface, sensor viewing angles away from the solar zenith are needed. For example, Fischer and Grassl (1984) calculate that to limit the ocean-reflected solar radiance to 5 W m$^{-2}$ sr$^{-1}$ $\mu$m$^{-1}$ for a solar zenith angle of 51°, the viewing zenith angle should be 30° (60° in the hemisphere opposite the solar azimuth) or less, and the viewing azimuth angle should be at least 45° away from the solar azimuth.

This study has provided analysis of observations taken from a nadir view, which represents only portions of satellite images. Additional use of off-nadir satellite data may be possible through application of azimuth-dependant bidirectional reflectance models. In this case, the effects of finite cloud geometry, including shadowing and illumination of cloud sides, further constrain the utility of a plane-parallel radiative transfer model in establishing cloud reflectance relationships. It is recommended that the retrieval method be tested for nadir observations alone, and then applied to other viewing geometries.

### 5.3.2 Applications

An objective estimation method for effective radius would be useful as part of routine satellite monitoring of regional cloud conditions. The potential applications of this method have been discussed in Chapter 1, most notably the diagnosis of cloud radiation budgets. For example, values of the effective radius and cloud liquid water path can be used to estimate optical depth at visible wavelengths (Stephens, 1978b) , Effective radius and liquid water content were applied in a parameterization of shortwave extinction, single scattering albedo, and asymmetry parameter (Slingo and Schrecker, 1982) for a broadband radiative transfer model. The liquid water content needed for these may be provided through assumption of an adiabatic liquid water profile through the cloud, or by development of microwave remote sensing capabilities. The shortwave radiative fluxes can then be used to improve net (shortwave plus longwave) radiation budget calculations, where the longwave components are estimated primarily from the liquid water contents of the clouds.

Many applications of cloud remote sensing focus on macroscopic parameters such as fractional cloudiness, hemispheric flux, and layer optical depth. These are critical to determining the atmosphere's radiative balance, but can be used only indirectly to estimate the physical characteristics of individual clouds. Assessment of cloud microphysical variables would have wide use in evaluating radiometric terms of the energy budget on the cloud scale, as well as in identifying cloud structure itself. Moreoever, radiative flux and radiatively-driven phase changes are potentially critical components in the mixed layer energy budgets. Cloud top radiative cooling may generate significant fluctuations in turbulent kinetic energy. Solar irradiance at cloud top can induce droplet evaporation and a corresponding transfer of water mass from a bulk volume extinction element to a molecular entity. Such conditions will cause feedback which subsequently alters the radiative exchange.

Randall *et al.* (1984) suggest that cloud top radiative cooling promotes convective entrainment, and this process, in turn, is modulated through changes in liquid water content by increased cloud evaporation and fractional cloudiness. Much more needs to be

known on the interdependance of stratus/stratocumulus microphysics and their radiative signature before this type of process can be monitored via satellites.

In previous sections we have discussed various impacts of cloud structure on the droplet size estimates. An additional source of error in applying the observed reflectance to estimate effective radius is a differing scale of variation in droplet size spectra and cloud optical depth. The spectral reflectance at 0.85 $\mu$m is used to determine a cloud optical depth scaled by the asymmetry parameter. While the asymmetry parameter is relatively invariant within stratocumulus (Stephens and Platt, 1987), the optical depth can vary greatly and is largely dependant on liquid water path. Liquid water contents were observed during the field programs described in this study to be more highly variable along horizontal sampling tracks in cloud than were the values of effective radius. Thus, for physically accurate estimates of effective radius, the cloud must be relatively uniform in optical depth as well as the effective radius within the satellite field of view. Stephens and Platt (1987) found that the majority of the explained variance in the horizontal sampling of 0.59-$\mu$m reflectance, representing optical depth, occurred at 0.5 km and 3 km scales. This suggests that the applications discussed above would require a satellite sampling resolution of better than 0.5 km, or that only cloud layers with a greater horizontal uniformity could be accurately sampled.

## 5.4 Topics of suggested future research

The use of remote sensing to characterize the marine boundary layer must rely on a group of techniques for retrieving several parameters. Combining multispectral measurements from visible, near-infrared, infrared, and microwave instruments have the potential of routinely providing data that can be applied to estimate cloud optical depth, physical depth, liquid water content, hydrometeor size and phase, the presence of aerosol, the presence of precipitation, *etc.* Satellite operational schedules allow cloud layers to be monitored with respect to both temporal and spatial variability. The challenge for future remote sensing methods is the testing of data sets to determine which complement of passive and active instruments is required for a given application. For example, the

simultaneous retrieval of $r_e$ and liquid water path would contribute substantially to the estimation of the cloud shortwave and longwave radiative budgets. DeVault and Katsaros (1983) suggest a method of determining cloud liquid water path using bandwidth-limited (*e.g.* moderately narrow) shortwave reflectance ratios. More extensive measurements of radiance in the water vapor windows as well as in narrow channels near the absorption bands can also help answer the questions related to apparently "anomalous" cloud optical depths. It would be advantageous to promote the use of experimental narrowband imaging systems, such as the proposed NASA Shuttle Imaging Spectrometer (Chen, 1985) . This instrument would have ground resolution better than 50 meters (that is, on the scale of cloud convective domes) and many spectral bands in the visible and near-infrared. New satellite instrument designs could thus be tested in space with minimal engineering effort and expense. Microwave instruments are also slated for experimental use on the Space Shuttle in the future.

Questions on the relationship of cloud structure to spectral reflectance cannot be fully answered without more complete information on cloud particle composition. Aerosol external to droplets and within droplets may play a role in modulating cloud radiances. More laboratory and field data is needed on the near-infrared spectral extinction characteristics of multicomponent cloud particle populations. Fischer (1976) used absorption and dispersion analyses on thin films of impacted aerosol to determine bulk infrared optical properties and translate these to individual particle properties. Composite refractive indices can also be estimated by assuming the physical arrangement of aerosol within a droplet (Blanchet and List, 1983) . However, the concentrations of various aerosol types found in the marine layer clouds should be known. In-cloud sampling of the droplet composition, and the refinement of tunable dye lasers, may be helpful in documenting the spectral variability of non-pure water droplet refractive properties.

Other uncertainties in how cloud reflectance is related to microphysical parameters require improved sampling of droplet sizes, liquid water content, and their spatial and temporal variability. It is possible that the optical probes commonly used to sample droplet size distributions are producing misleading information (Baumgardner, 1986) . Studies

which rely on an intercomparison of cloud physical measurements and radiometric data should perhaps verify the droplet size measurements with more than one sampling instrument. Finally, it is suggested that additional research on the reflectance characteristics for a wide variety of sampled clouds be undertaken. Narrowband radiometric data is available now from earth resources satellites. An analysis program should also be planned prior to the launch of the first NOAA satellite carrying the AVHRR Channel 3A, to take advantage of information in the 1.6-$\mu$m water vapor window.

## REFERENCES


Abramowitz, M., and I.A. Stegun, ed., 1965: *Handbook of Mathematical Functions.* Dover, New York, 1046 pp.

Ackermann, S.A., and S.K. Cox, 1981: Aircraft observations of the shortwave fractional absorptance of non-homogeneous clouds. *J. Appl. Meteor.*, **20**, 1510–1515.

Ackermann, S.A., and G.L. Stephens, 1987: The absorption of solar radiation by cloud droplets: An application of anomalous diffraction theory. *J. Atmos. Sci.*, **44**, 1574–1588.

Arking, A., and J.D. Childs, 1985: Retrieval of cloud cover parameters from multispectral satellite images. *J. Clim. Appl. Meteor.*, **24**, 322–333.

Baker, M.B., and J. Latham, 1979: The evolution of the droplet spectra and the rate of production of embryonic raindrops in small cumulus clouds. *J. Atmos. Sci.*, **36**, 1612–1615.

Baker, M.B., R.E. Breidenthal, T.W. Choularton, and J. Latham, 1984: The effects of turbulent mixing in clouds. *J. Atmos. Sci.*, **41**, 299–304.

Barkstrom, B.R., 1978: Some effects of 8-12 $\mu$m radiant energy transfer on the mass and heat budgets of cloud droplets. *J. Atmos. Sci.*, **35**, 665–673.

Battalino, T.E., R. Helvey, C.J. Walcek, J. Rosenthal, and J. Gottschalk, 1982: Air mass trajectory analysis as an aid in distinguishing marine from continental aerosol distributions at San Nicholas Island. In *Atmospheric Aerosols*, ed. A. Deepak. Spectrum Press, Hampton, VA, 125–134.

Baumgardner, D., 1987: Corrections for the response times of particle measuring probes. *Proc., AMS 6th Symposium on Meteor. Observations and Instrumentation*, New Orleans, LA, 148-151.

Baumgardner, D., J.E. Dye, and W.A. Cooper, 1986: The effects of measurement uncertainties on the analysis of cloud particle data. *Proc., Joint Sessions AMS 23rd Conf. on Radar Meteor., Conf. on Cloud Physics*, Snowmass, CO, JP313–JP316.

Blanchet, J.-P., and R. List, 1983: Estimation of optical properties of Arctic haze using a numerical model. *Atmos.-Ocean*, **21**, 444–465.

Bohren, C.F., and B.R. Barkstrom, 1974: Theory of the optical properties of snow. *J. Geophys. Res.*, **79**, 4527–4535.

Bonnel, B., Y. Fouquart, J.C. Vanhoutte, C. Fravalo, and R. Rosset, 1983: Radiative properties of some African and midlatitude stratocumulus clouds. *Contr. Atmos. Phys.*, **56**, 409–428.

Bunting, J.T., and R.P. d'Entremont, 1982: Improved cloud detection utilizing Defense Meteorological Satellite Program near-infrared measurements. *AFGL Technical Report 82-0027.* Hanscom AFB, MA, 91 pp.

Carlson, T.N., and S.G. Benjamin, 1980: Radiative heating rates for Saharan dust. *J. Atmos. Sci.*, **37**, 193–213.

Caughey, S.J., and M. Kitchen, 1984: Simultaneous measurements of the turbulent and microphysical structure of nocturnal stratocumulus cloud. *Quart. J. Roy. Meteor. Soc.*, **110**, 13–34.

Chandrasekhar, S., 1950: *Radiative Transfer.* Oxford University Press, 393 pp.

Charlock, T.P., 1982: Climate optical feedback and climate stability in a radiative-convective model. *Tellus*, **34**, 245–254.

Chen, H.S., 1985: *Space Remote Sensing Systems.* Academic Press, Inc., Orlando, FL, 257 pp.

Chýlek, P., V. Ramaswamy, and R.J. Cheng, 1984: Effect of graphitic carbon on the albedo of clouds. *J. Atmos. Sci.*, **41**, 3076–3084.

Collins, D.G., and M.B. Wells, 1965: *Monte Carlo codes for study of light transport in the atmosphere. Vol. I, Description of codes.* U.S. Department of Commerce, Institute for Applied Technology, 100 pp.

Collins, D.G., W.G. Blättner, M.B. Wells, and H.G. Horak, 1972: Backward Monte Carlo calculations of the polarization characteristics of the radiation emerging from spherical-shell atmospheres. *Appl. Opt.*, **11**, 2684–2696.

Coulson, K.L, J.V. Dave, and Z. Sekera, 1960: *Tables Related to Radiation Emerging from a Planetary Atmosphere with Rayleigh Scattering.* U. California Press, Berkeley, 548 pp.

Curran, R.J., and M.-L.C. Wu, 1982: Skylab near-infrared observations of clouds indicating supercooled liquid water droplets. *J. Atmos. Sci.*, **39**, 635–647.

Curry, J.A., 1986: Interactions among turbulence, radiation, and microphysics in Arctic stratus clouds. *J. Atmos. Sci.*, **43**, 90–106.

Davies, R., 1978: The effect of finite geometry on the three-dimensional transfer of solar irradiance in clouds. *J. Atmos. Sci.*, **35**, 1712–1725.

Davies, R., 1984: Reflected solar radiances from broken cloud scenes and the interpretation of scanner measurements. *J. Geophy. Res.*, **89**, 1259–1266.

Davies, R., 1985: Response of cloud supersaturation to radiative forcing. *J. Atmos. Sci.*, **42**, 2820–2825.

Davies, R., W.L. Ridgway, and K.-E. Kim, 1984: Spectral absorption of solar radiation in cloudy atmospheres: A 20 $cm^{-1}$ model. *J. Atmos. Sci.*, **41**, 2126–2137.

Davis, J.M., S.K. Cox, and T.B. McKee, 1979: Total shortwave radiative characteristics of absorbing finite clouds. *J. Atmos. Sci.*, **36**, 508–518.

Davis, J.M., T.B. McKee, and S.K. Cox, 1985: Application of the Monte Carlo method to prblems in visibility using a local estimate: an investigation. *Appl. Opt.*, **24**, 3193–3205.

Derr, V. E., 1984: Atmospheric Handbook. *NOAA NESDIS World Data Center 'A' Report UAG-89.* Boulder, CO, 57 pp.

Devault, J.E., and K.B. Katsaros, 1983: Remote determination of cloud liquid water path from bandwidth-limited shortwave measurements. *J. Atmos. Sci.*, **40**, 665-685.

Deirmendjian, D., 1964: Scattering and polarization properties of water clouds and hazes in the visible and infrared. *Appl. Opt.*, **3**, 187–196.

Drummond, A.J., ed., 1970: Precision Radiometry. *Advances in Geophysics Vol. 14.* Academic Press, New York. 415 pp.

Elterman, L., 1968: UV, Visible, and IR Attenuation for Altitudes to 50 km. Office of Aerospace Research, U.S. Air Force.

Fischer, K., 1976: The optical constants of atmospheric aerosol particles in the 7.5-12 $\mu$m spectral region. *Tellus*, **28**, 266–274.

Fischer, K., and H. Grassl, 1984: Radiative transfer in an atmosphere-ocean system: An azimuthally dependant matrix-operator approach. *Appl. Opt.*, **23**, 1032–1039.

Foot, J.S., 1988: Some observations of the optical properties of clouds. I: Stratocumulus. *Quart. J. Roy. Meteor. Soc.*, **114**, 129–144.

Grant, I.P., and G.E. Hunt, 1968: Solution of radiative transfer problems in planetary atmospheres. *Icarus*, **9**, 526–534.

Hale, G.M., and M.R. Querry, 1973: Optical constants of water in the 200-nm to 200-$\mu$m wavelength region. *Appl. Opt.*, **12**, 555–563.

Hänel, G., 1976: The single-scattering albedo of atmospheric aerosol particles as a function of relative humidity. *J. Atmos. Sci.*, **33**, 1120–1124.

Hansen, J.E., 1969: Exact and approximate solutions for multiple scattering by cloudy and hazy planetary atmospheres. *J. Atmos. Sci.*, **26**, 478–487.

Hansen, J.E., 1971a: Multiple scattering of polarized light in planetary atmospheres. Part I. The doubling method. *J. Atmos. Sci.*, **28**, 120–125.

Hansen, J.E., 1971b: Multiple scattering of polarized light in planetary atmospheres. Part II. Sunlight reflected by terrestrial water clouds. *J. Atmos. Sci.*, **28**, 1400–1426.

Hansen, J.E., and J.B. Pollack, 1970: Near-infrared light scattering by terrestrial clouds. *J. Atmos. Sci.*, **27**, 265–281.

Hansen, J.E., and L.D. Travis, 1974: Light scattering in planetary atmospheres. *Space Sci. Rev.*, **16**, 527–610. Hansen, J.E., 1971:

Henyey, L.G., and J.L. Greenstein, 1941: Diffuse radiation in the galaxy. *Astro. Journal*, **93**, 70–83.

Herman, G.F., 1977: Solar radiation in summertime arctic stratus clouds. *J. Atmos. Sci.*, **34**, 1423–1432.

Herman, G.F., and J.A. Curry, 1984: Observational and theoretical studies of solar radiation in Arctic stratus clouds. *J. Clim. Appl. Meteor.*, **23**, 5–24.

Hignett, P., 1987: A study of the short-wave radiative properties of marine stratus: Aircraft measurements and model comparisons. *Q. J. R. Meteor. Soc.*, **113**, 1011–1024.

Hill, T.A., and T.W. Choularton, 1985: An airborne study of the micorphysical structure of cumulus clouds. *Quart. J. Roy. Meteor. Soc.*, **111**, 517–544.

Irvine, W.M., and J.B. Pollack, 1968: Infrared Optical Properties of Water and Ice Spheres. *Icarus*, **8**, 324–360.

Jensen, D.R., 1978: Aerosol measurements in the marine boundary layer at San Diego. *Tech. Report 168*, Naval Ocean Systems Center, San Diego.

Joseph,J.H., W.J. Wiscombe, and J.A. Weinman, 1976: The delta-Eddington approximation for radiative flux transfer. *J. Atmos. Sci.*, **33**, 2452–2459.

Kim, Kyung-Eak, 1983: Spectral absorption of solar radiation in homogeneous clouds. M.S. Thesis, Purdue University, 76 pp.

King, M.D., 1986: Determination of the optical thickness of clouds from reflected solar radiation measurements. *Extended Abstracts, AMS Sixth Conf. on Atmos. Radiation*, Williamsburg, VA, 66–69.

Köpp, F., and H. Müller, 1977: Experimental and numerical determination of reflected radiation from clouds. *Proc. Symp. Radiation in the Atmosphere*, H.-J. Bolle, ed. Science Press, Princeton, 202–204.

Kneizys, F.X., E.P. Shettle, W.O. Gallery, J.H. Chetwynd, Jr., L.W. Abreu, J.E.A. Selby, S.A. Clough, and R.W. Fenn, 1983: Atmospheric Transmittance/Radiance: Computer Code LOWTRAN 6. *AFGL Technical Report 83-0187*, 200 pp.

Kuo, H.-C., 1987: Dynamical modeling of marine boundary layer convection. *CSU Atmospheric Science Paper No. 412*, Colorado State University, 126 pp.

Kyle, H.L., R.J. Curran, W.L. Barnes, and D. Escoe, 1978: A cloud physics radiometer. *Proc., AMS Third Conf. on Atmos. Radiation*, Davis, CA, 107–110.

Lee, I.Y., G. Hänel, and H.R. Pruppacher, 1980: A numerical determination of the evolution of cloud drop spectra due to condensation on natural aerosol particles. *J. Atmos. Sci.*, **37**, 1839–1853.

Lilly, D.K., 1968: Models of cloud-topped mixed layers under a strong inversion. *Quart. J. Roy. Meteor. Soc.*, **94**, 292–309.

McKee, T.B., and S.K. Cox, 1974: Scattering of visible radiation by finite clouds. *J. Atmos. Sci.*, **31**, 1885–1892.

Nakajima, T., and M.D. King, 1988: Cloud optical properties as derived from the multispectral cloud radiometer. *FIRE Science Team Workshop*, July 11–15, Vail, CO, 321–326.

Newiger, M., and K. Bähnke, 1981: Influence of cloud composition and cloud geometry on the absorption of solar radiation. *Contri. Atmos. Phys.*, **54**, 370–382.

Nicholls, S., and J. Leighton, 1986: An observational study of the structure of stratiform cloud sheets: Part I. Structure. *Quart. J. Roy. Meteor. Soc.*, **112**, 431–460.

Nicholls, S., and J.D. Turton, 1986: An observational study of the structure of stratiform cloud sheets: Part II. Entrainment. *Quart. J. Roy. Meteor. Soc.*, **112**, 461–480.

Noonkester, V.R., 1984: Droplet spectra observed in marine stratus cloud layers. *J. Atmos. Sci.* **41**. 829–845.

Paltridge, G.W., and C.M.R. Platt, 1976: *Radiative Processes in Meteorology and Climatology*. Elsevier, New York, 318 pp.

Plass, G.N. and G.W. Kattawar, 1968: Monte Carlo calculations of light scattering from clouds. *Appl. Opt.*, **7**, 415–419.

Plass, G.N., G.W. Kattawar, and F.E. Catchings, 1973: Matrix operator theory of radiative transfer. 1: Rayleigh scattering. *Appl. Optics*, **12**, 314–329.

Podzimek, J., 1982: Marine aerosol research. *Időjárás*, **86**, 179–199.

Press, W.H., B.P. Flannery, S.A. Teukolsky, and W.T. Vetterling, 1986: *Numerical Recipes.* Cambridge University Press, Cambridge, 818 pp.

Randall, D.A., J.A. Coakley, Jr., C.W. Fairall, R.A. Kropfli, and D.H. Lenschow, 1984: Outlook for research on subtropical marine stratiform clouds. *Bull. Amer. Meteor. Soc.*, **65**, 1290–1301.

Raschke, E., ed., 1978: *Terminology and units of radiation quantities and measurements.* IAMAP, Boulder CO, 17 pp.

Reynolds, D.W., T.H. Vonder Haar, and S.K. Cox, 1975: The effect of solar radiation absorption in the tropical troposphere. *J. Appl. Meteor.*, **14**, 433–444.

Rogers, D.P., and J.W. Telford, 1986: Metastable stratus tops. *Quart. J. Roy. Meteor. Soc.*, **112**, 481–500.

Schubert, W.H., J.S. Wakefield, E.J. Steiner, and S.K. Cox, 1979: Marine stratocumulus convection. Part I: Governing equations and horizontally homogeneous solutions. *J. Atmos. Sci.*, **36**, 1286–1307.

Shettle, E.P., and R.W. Fenn, 1979: Models for the aerosols of the lower atmosphere and the effects of humidity variations on their optical properties. *Environmental Research Paper 676, AFGL Technical Report 79-0214*, Air Force Geophysics Laboratory, Hanscom AFB, MA, 94 pp.

Skumanich, A., and K. Bhattachargie, 1961: *J. Opt. Soc. Am.*, **51**, 484.

Slingo, A., and H.M. Schrecker, 1982: On the shortwave properties of stratiform water clouds. *Quart. J. Roy. Meteor. Soc.*, **108**, 407–426.

Slingo, A., S. Nicholls, and J. Schmetz, 1982: Aircraft observations of marine stratocumulus during JASIN. *Quart. J. Roy. Meteor. Soc.*, **108**, 833–856.

Stair, R., R.G. Johnston, and E.W. Halbach, 1960: Standard of spectral radiance for the region of 0.25 to 2.6 microns. *J. Research Nat. Bur. Standards*, **64A**, 291–296.

Stephens, G.L., 1978a: Radiation profiles in extended water clouds. I: Theory. *J. Atmos. Sci.*, **35**, 2111–2122.

Stephens, G.L., 1978b: Radiation profiles in extended water clouds. II: Parameterization schemes. *J. Atmos. Sci.*, **35**, 2123–2132.

Stephens, G.L., 1978c: Radiation profiles in extended water clouds. III: Observations. *J. Atmos. Sci.*, **35**, 2133–2141.

Stephens, G.L, 1986: Radiative transfer in two-dimensionally anisotropically scattering media. *J. Quart. Spectros. Rad. Transfer*, **36**, 51–67.

Stephens, G.L., and C.M.R. Platt, 1987: Aircraft observations of the radiative and microphysical properties of stratocumulus and cumulus cloud fields. *J. Atmos. Sci.*, **26**, 1243–1269.

Stephens, G.L., and J.C. Scott, 1985: A high speed spectrally-scanning radiometer (SPERAD) for airborne measurements of cloud optical properties. *J. Atmos. Ocean. Tech.*, **2**, 148–156.

Stewart, R.H., 1985: *Methods of Satellite Oceanography* (Chapters 6,7). Univ. of Calif. Press, Berkeley, 360 pp.

Stuhlmann, R., P. Minnis, and G.L. Smith, 1985: Cloud bidirectional reflectance functions: A comparison of experimental and theoretical results. *Appl. Optics*, **24**, 396–401.

Telford, J.W., and P.B. Wagner, 1981: Observations of condensation growth determined by entity type mixing. *Pure Appl. Geophysics*, **119**, 934–965.

Telford, J.W., T.S. Keck, and S.K. Chai, 1984: Entrainment at cloud tops and the droplet spectra. *J. Atmos. Sci.*, **41**, 3170–3179.

Tsay, S.-C., J.M. Davis, G.L. Stephens, S.K. Cox, and T.B. McKee, 1987: *Backward Monte Carlo Computations of Radiation Propagating in Horizontally Inhomogeneous Media. Part I: Description of Codes.* Cooperative Institute for Research in the Atmosphere, Fort Collins, CO, 76 pp.

Twomey, S., 1987: Influence of internal scattering on the optical properties of particles and drops in the near infrared. *Appl. Optics*, **26**, 1342–1347.

Twomey, S., and C.F. Bohren, 1980: Simple approximations for calculations of absorption in clouds. *J. Atmos. Sci.*, **37**, 2086–2094.

Twomey, S. and T. Cocks, 1982: Spectral refectance in the near-infrared: Comparison of measurements and calculations. *J. Meteor. Soc. Japan*, **60**, 583–592.

van de Hulst, H.C., 1980: *Multiple Light Scattering.* Academic Press, New York, 738 pp.

van de Hulst, H.C., 1981: *Light Scattering by Small Particles.* Dover, Inc., New York, 470 pp.

Vonder Haar, T.V., C.-F. Shih, D.L. Randel, J.J. Toth, D.N. Allen, R.A. Pielke, and R. Green, 1987: The prototype digital weather laboratory at Colorado State University. *Bull. Amer. Meteor. Soc.*, **68**, 230-236.

Wallace, J.M., and P.V. Hobbs, 1977: Introduction to Atmospheric Science. Academic Press, New York.

Warner, J., 1973: The microstructure of cumulus clouds, Part IV: The effect on the droplet spectrum of mixing between cloud and environment. *J. Atmos. Sci.*, **30**, 256–261.

Weiss, R.E., R.J. Charlson, A.P. Waggoner, N. Sadler, and J. Ogren, 1980: An assessment of light absorption by aerosol particles in urban, rural and remote tropospheric and stratospheric air. *Extended Abstracts, 1980 International Radiation Symposium*, Fort Collins, CO, 178–180.

Welch, R.M., and B.A. Wielicki, 1984: Stratocumulus cloud field reflected fluxes: The effect of cloud shape. *J. Atmos. Sci.*, **41**, 3085–3103.

Welch, R.M., and B.A. Wielicki, 1985: A radiative parameterization of stratocumulus cloud fields. *J. Atmos. Sci.*, **42**, 2888–2897.

Welch, R.M., S.K. Cox, and J.M. Davis, 1980: Solar Radiation and Clouds. *Meteorological Monographs*, **17 #39**, American Meteorological Society, Boston, MA, 96 pp.

Wendling, P., 1977: Albedo and reflected radiance of horizontally inhomogeneous clouds. *J. Atmos. Sci.*, **34**, 642–650.

Wetzel, M., and T.H. Vonder Haar, 1986a: The impact of stratocumulus microphysical variations on near-infrared radiance. *Extended Abstracts, AMS Sixth Conf. on Atmos. Radiation*, Williamsburg, VA, 153–156.

Wetzel, M., and T. Vonder Haar, 1986b: Modeling and observation of near-IR cloud signatures in the marine boundary layer. *Fourth Tri-Service Cloud Modeling Workshop*, Hanscom AFB, MA, 50–64.

Wiscombe, W.J., 1976a: Extension of the doubling method to inhomogenous sources. *J. Quant. Spec. Rad. Trans.*, **16**, 477–489.

Wiscombe, W.J., 1976b: On initialization, error and flux conservation in the doubling method. *J. Quant. Spec. Rad. Trans.*, **16**, 637–658.

Wiscombe, W.J., 1977: The delta-M method: Rapid yet accurate radiative flux calculations for strongly asymmetric phase functions. *J. Atmos. Sci.*, **34**, 1408–1422.

Wiscombe, W.J., R.M. Welch, and W.D. Hall, 1984: The effects of very large drops on cloud absorption. Part I: Parcel models. *J. Atmos. Sci.*, **41**, 1336–1355.

## Appendix A

## DATA COLLECTION FOR CALIFORNIA STRATUS EXPERIMENT

A twin-engine Piper Navajo was used in airborne sampling of marine stratus and stratocumulus clouds during June 1986 with an experimental spectral radiometer. The research aircraft was equipped with atmospheric state parameter and microphysical instrumentation (Jensen, 1978), and was available through the cooperation with and support by the Naval Ocean Systems Center (NOSC).

Sampling at incremental altitudes made it possible to describe the vertical variation of temperature and dew point which define the boundary layer and inversion. Also helpful in the analysis of atmospheric structure were the local (at Montgomery Field) National Weather Service (NWS) rawinsonde vertical profiles. These, and the NWS surface hourly measurements from the coastal region and islands, were received via the FAA604 communications channel and archived at CSU. In addition, digital image data were obtained from the geostationary and polar-orbiting meteorological satellites.

The research aircraft flew horizontal tracks at two or more heights above cloud, such as directly above cloud top and above the estimated inversion level or visible haze lid. Microphysical parameters were sampled 100 foot altitude increments near cloud top (30 meter increments; non-metric units used during operations for reference to aircraft cockpit instruments) and at 200 foot (61 meter) intervals at lower levels within the cloud. The aircraft suffered power system problems during the 1986 field program, so that portions of the flight periods in Table A.1 did not yield complete data sets. For example, the flight on Julian day 179 provided little data because of power loss problems. Study of the stratus layers was limited to the region relatively close to the coast due to the aircraft fuel capacity, and certain areas within aircraft range were off-limits due to military operations.

Table A.1: Aircraft measurement periods during June 1986.

| *Date* | *Julian day* | *Time period (UTC)* |
|---|---|---|
| 24 June | 175 | 2012–2201 |
| 25 June | 176 | 2202–2340 |
| 26 June | 177 | 1523–1744 |
| 27 June | 178 | 0132–0250 |
| 28 June | 179 | 1406–1445 |
| 28 June | 179 | 1555–1612 |
| 29 June | 180 | 1420–1755 |
| 30 June | 181 | 1418–1757 |

Particle size distributions were obtained at eight second intervals over the size range 0.23 to 150 $\mu$m radius by PMS, Inc. optical probes; the Axially Scattering Spectrometer Probe (ASSP) Model 100, and the Optical Array Probe (OAP) Model 200. Within this range, it was possible to directly determine the $dN/dr$, or differential particle concentration, for a total of 47 sub-ranges of varying size increment. The optical probes count the number of individual particles which are sensed during passage through the sampling volume, $v_i$.

$$v_i = a_i s \Delta t, \tag{A.1}$$

where $a_i$ is the sampling area for a given size range $i$, $s$ is the true airspeed through the sampling unit, and $\Delta t$ is the sampling time interval. For the ASSP size ranges, $a_i$ is a constant, while for the OAP the value of $a_i$ increases with size. The concentration of particles in a given size range, $n_i$, is given by dividing the number of droplets counted in each channel ($c_i$) by the sampling volume:

$$n_i = \frac{c_i}{v_i}. \tag{A.2}$$

Thus, the moments of a sampled particle distribution are derived from summation over each size range's concentration. The central radius ($r_i$) and differential radius interval ($d_i$) associated with each size range are given in Table A.2.

Table A.2: List of PMS optical probe size ranges.

| *Probe type* | *Channel #* | $r_i$ ($\mu m$) | $d_i$ ($\mu m$) | *Probe type* | *Channel #* | $r_i$ ($\mu m$) | $d_i$ ($\mu m$) |
|---|---|---|---|---|---|---|---|
| ASSP | 1 | 0.300 | 0.150 | OAP | 33 | 15.833 | 2.3 |
| | 2 | 0.450 | 0.150 | | 34 | 22.050 | 10.1 |
| | 3 | 0.600 | 0.150 | | 35 | 32.000 | 9.8 |
| | 4 | 0.750 | 0.150 | | 36 | 41.800 | 10.0 |
| | 5 | 0.900 | 0.150 | | 37 | 51.700 | 9.8 |
| | 6 | 1.050 | 0.150 | | 38 | 61.500 | 9.8 |
| | 7 | 1.225 | 0.175 | | 39 | 71.350 | 9.9 |
| | 8 | 1.400 | 0.200 | | 40 | 81.250 | 9.9 |
| | 9 | 1.590 | 0.175 | | 41 | 91.050 | 9.7 |
| | 10 | 1.765 | 0.175 | | 42 | 100.95 | 10.1 |
| | 11 | 1.950 | 0.200 | | 43 | 110.75 | 9.5 |
| | 12 | 2.150 | 0.200 | | 44 | 120.25 | 9.5 |
| | 13 | 2.365 | 0.230 | | 45 | 130.00 | 10.0 |
| | 14 | 2.590 | 0.220 | | 46 | 140.00 | 10.0 |
| | 15 | 2.840 | 0.280 | | 47 | 150.00 | 10.0 |
| | 16 | 3.130 | 0.300 | | | | |
| | 17 | 3.440 | 0.320 | | | | |
| | 18 | 4.125 | 0.550 | | | | |
| | 19 | 4.675 | 0.550 | | | | |
| | 20 | 5.225 | 0.550 | | | | |
| | 21 | 5.750 | 0.500 | | | | |
| | 22 | 6.250 | 0.500 | | | | |
| | 23 | 6.750 | 0.500 | | | | |
| | 24 | 7.250 | 0.500 | | | | |
| | 25 | 7.690 | 0.920 | | | | |
| | 26 | 8.625 | 0.950 | | | | |
| | 27 | 9.565 | 0.930 | | | | |
| | 28 | 10.49 | 0.920 | | | | |
| | 29 | 11.44 | 0.980 | | | | |
| | 30 | 12.365 | 0.870 | | | | |
| | 31 | 13.275 | 0.950 | | | | |
| | 32 | 14.225 | 0.950 | | | | |

Parameters of the size distributions were determined for populations. The first utilized the entire size spectrum available from the optical probes, while the second ignored aerosol (particles less than 2 $\mu$m in radius). Summation over the size ranges from 1 to 47, listed in Table A.2, corresponds to what we define as the particle size distribution. The equations for number concentration, liquid water content, effective radius and mean radius shown below are those for the entire particle size range. Calculations of the same parameters for the droplet size distributions (neglecting aerosol) were made by using the same basic equations with a summation over size ranges 12 through 47.

Particle concentration is given by

$$N = \sum_{i=1}^{47} n_i d_i. \tag{A.3}$$

Liquid water concentration, assuming pure water droplets with density $\rho_w$, is

$$W = \rho_w \frac{4}{3}\pi \sum_{i=1}^{47} n_i r_i^3 d_i. \tag{A.4}$$

The effective radius is found from

$$r_e = \frac{\sum_{i=1}^{47} n_i r_i^3 d_i}{\sum_{i=1}^{47} n_i r_i^2 d_i}, \tag{A.5}$$

and the mean radius is calculated from

$$r_m = \frac{\sum_{i=1}^{47} n_i r_i d_i}{\sum_{i=1}^{47} n_i d_i}. \tag{A.6}$$

Studies by Baumgardner *et al.* (1986) indicate that electronic response time and optical depth of field for the PMS probes can introduce improper sizing of particles. This can lead to discrepancies in the regions of size overlap for multiple probes. Corrections of this error generally must increase as the airspeed increases (Baumgardner, 1987). The aircraft used for this study had a relatively low operating speed (54 m $s^{-1}$), so that error in droplet concentrations were expected to be minimal. An error in the measured concentrations of droplets would bias the effective radius values obtained from the aircraft sampling and influence the comparison between $r_e$ and spectral reflectance observations.

Thermodynamic variables such as temperature, relative humidity, and pressure were recorded simultaneously at five second intervals on the aircraft. A LORAN-C navigation

processor recorded latitude and longitude at the same sampling frequency. Temperature was obtained by a Rosemount temperature probe, dew point and relative humidity were determined from an EG & G Model 137-C3 cooled-mirror hygrometer, and pressure altitude was measured by a Rosemount Model 542K pressure altimeter.

It was possible to also archive the National Weather Service data for the twice-daily rawinsondes launched locally at Montgomery Field, and for the hourly surface observations of temperature, dew point, cloud cover, wind, *etc.* at many stations along the coast and on the coastal islands. This information was processed into tabular and graphic format using software which is available at the CSU Cooperative Institute for Research in the Atmosphere (CIRA) (Vonder Haar *et al.*, 1987).

The CSU Spectral Radiometer (SR), manufactured by CI, Ltd. as Model SR-1000 was used to obtain relative spectral radiances. The SR is a rugged field instrument designed to measure the radiant signal from targets, point sources, and backgrounds. It operates in a continuous scanning mode with a rotating filter wheel or in a single filter mode. A discrete filter wheel (DFW) was designed and built at CSU to allow narrowband radiances to be obtained in the near-infrared region not covered by the continuously variable filter (CVF) wheels provided by the manufacturer. The design of this DFW and its mode of operation were determined in part by the operating conditions possible for the SR. Although the SR has been modified at CSU to allow more complete electronic control of sampling, most of these improvements were not available for use during this field measurement program. The SR was operated in both a scanning mode and a fixed wheel position so that a single or a sequence of filters could be sampled. These filters are described in Table A.3, in sequential order according to their sampling position on the circular rotating filter wheel.

The filters selected from OCLI, Inc. stock catalogs for characteristics of filter center wavelength, half-width, and transmissivity which would provide the needed radiance data and sensitivity for the field program. Other filters were installed in the DFW that have not been used for this study. The 0.65 $\mu$m and 0.85 $\mu$m radiances were detected by a silicon (Si) chip element in an (uncooled) detector unit. The 1.6-$\mu$m radiances were sensed by a lead sulfide (PbS) element in the same unit. The photoconductive PbS exhibits an

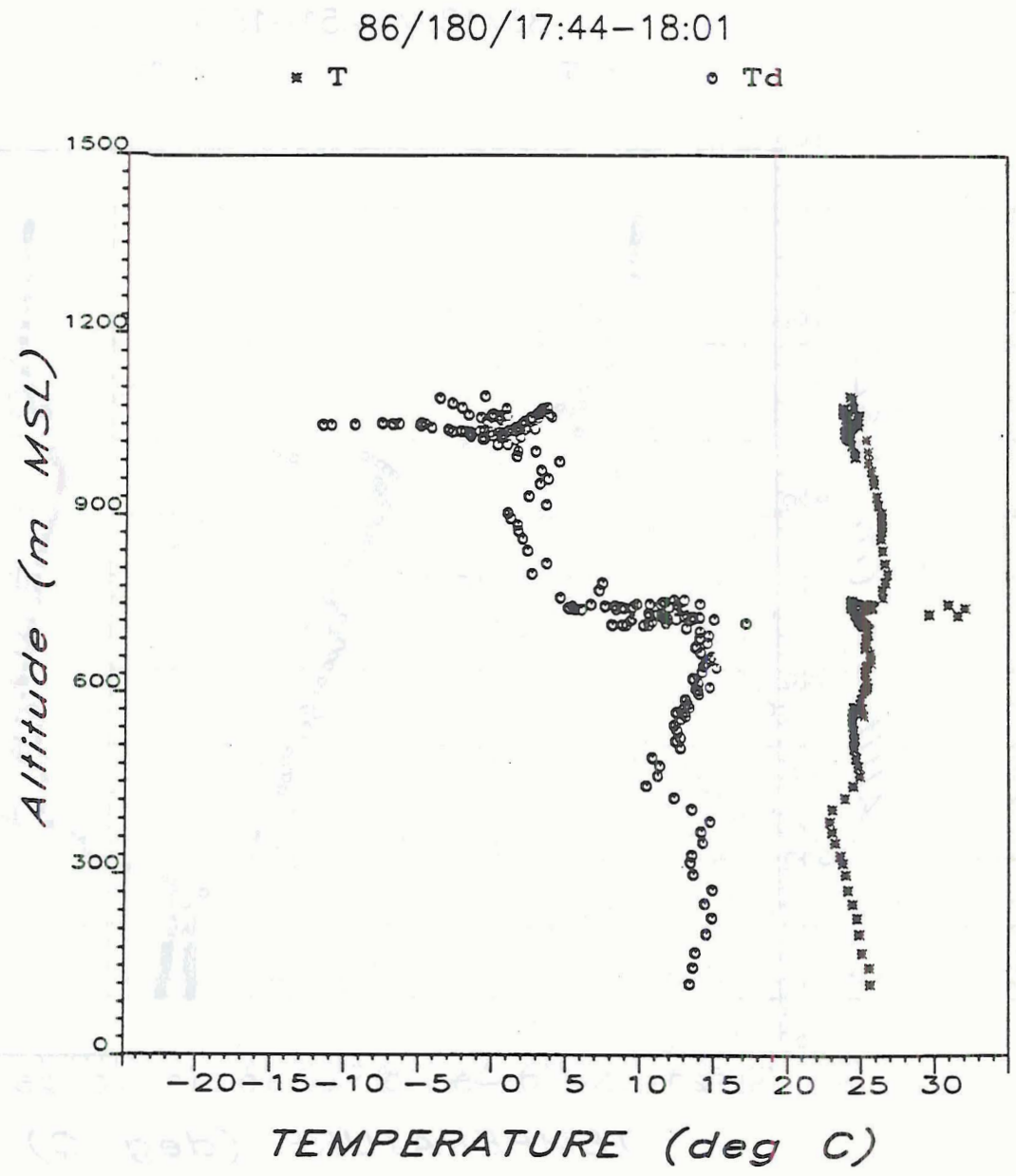


Figure A.4: Profile sampled from aircraft, 1800 UTC on day 180.

of one kilometer can be obtained within a time frame of 20 seconds, and can be matched in the shortwave satellite image data for coincident observation times. Exact viewing coincidence is not easily attained with limited flight schedules, particularly for the polar-orbiting satellites which pass over a given region only twice daily. The satellite shortwave imagery was, however, quite useful in observing reflectances within the cloud field.

The satellite imagery provides an encompassing look at the study region during the transition from morning cloud cover to breakup near the coast. The size and spacing of cloud elements increases throughout the image area during the day. The temperatures of the stratus tops and the ocean surface are found to be within 3°C in the AVHRR thermal channel data. Infrared imagery from the night hours indicate the filling in of cloud cover to the coast, and a slight decrease in cloud top temperature associated with the overcast conditions.

Deduced values of reflectance in the AVHRR 0.65-$\mu$m channel varied between 20% and 30%, for thinner and thicker cloud layers. These are less than calculated from the AD model for the sampled cloud droplet size distribution, but the 0.65 $\mu$m atmospheric transmission calculated from cloud top to satellite via LOWTRAN-6 was only 70%. The LOWTRAN model includes ozone and aerosol parameters which are significant at the 0.65 $\mu$m wavelength. Time-dependent variation was noted due to the changing solar zenith angle, aside from obvious variation in cloud distribution.